© 2018 by Sarvagya Sharma. All rights reserved.

NV DIAMOND PROJECT FOR NEDM

BY

SARVAGYA SHARMA

DISSERTATION

Submitted in partial fulfillment of the requirements
for the degree of Doctor of Philosophy in Physics
in the Graduate College of the
University of Illinois at Urbana-Champaign, 2018

Urbana, Illinois

Doctoral Committee:

Professor Paul Kwiat, Chair
Professor Douglas Beck, Director of Research
Professor Brian Demarco
Professor David Ceperley

Abstract

This work presents the research conducted on Nitrogen Vacancy (NV) defects in diamonds for the nEDM experiment which has an operating temperature of 0.5 K. NV defects have been investigated as metrological sensors for measuring both, electric and magnetic fields at room temperature and also at 4 K.

This thesis discusses different techniques used to probe the NV centers electronic structure. The first, Optically Detected Magnetic Resonance (ODMR) allows us to probe the Zeeman and Stark induced shifts in the ground state through resonant microwave spectroscopy. This technnique has helped us study and characterize the response of the NV center to electromagnetic fields. The use of the NV center ensemble as a vector field sensor is also studied using ODMR.

The second technique allows us to build a sensor which also measures the ground state resonances but without the need for microwaves. Instead the quantum phenomenon of electromagnetically induced transparency (EIT) was used. This all-optical method makes diamonds containing NV centers a suitable sensor of the nEDM experiment.

The driven and free spin dynamics of the NV center are also investigated in this work. Studying the evolution of the NV center spin gives us important clues about its spin bath environment and the characterisitic time constants over which the NV spin states decay. These time constants set the fundamental limit of the sensitivity for measuring magnetic and electric fields.

Acknowledgements

I would first like to thank my advisor and mentor, Doug Beck, who not only helped me figure out answers, but also raised important questions that have guided my research. I would also like to thank our wonderful friend and collaborator, Chris Hovde from Southwest Sciences, without his experience and expertise, the work reported here would have been impossible. Researchers from other labs, including Victor Acosta, Phil Hemmer and Dima Budker have also provided valuable input essential for this project.

I am ever grateful to my family for their constant encouragement and support throughout my scientific career. It has also taken support from my friends in Illinois and Texas for me to complete seven years of doctoral research - you have my heart-felt gratitude.

Table of Contents

List of Figures . . . . . **vi**

Chapter 1 Introduction **1**
1.1 nEDM 1
1.1.1 Symmetries 1
1.1.2 Symmetry violation 2
1.1.3 Baryon Asymmetry 4
1.1.4 Symmetry violation in the neutron 4
1.1.5 nEDM Experiment at SNS 5
1.2 The NV Center 8
1.2.1 Electronic Structure 10
1.2.2 Fabrication 16

Chapter 2 Optically Detected Magnetic Resonance **21**
2.1 Theory 21
2.2 Experimental Details 23
2.2.1 Resolution of confocal microscope 25
2.2.2 Polarization-dependent excitation 27
2.3 Strain measurements 28
2.3.1 Lineshape 28
2.3.2 Strain magnitude 30
2.3.3 Strain Direction 32
2.3.4 Electrometry 34
2.3.5 Electric field imaging 40

Chapter 3 Spin Dynamics **42**
3.1 Introduction 42
3.1.1 Two-level excitation 43
3.1.2 The Bloch Sphere 43
3.1.3 Density Matrix 44
3.1.4 Decoherence 45
3.2 Experimental Details 48
3.2.1 Detection Scheme 48
3.2.2 The Antenna 49
3.3 Rabi Oscillations 51
3.3.1 Theory 51
3.3.2 Results 54
3.3.3 Microwave intensity map 57
3.4 Free Induction Decay 57
3.4.1 Theory 57
3.4.2 Results 59
3.5 Hahn Echo 61

3.5.1 Theory 61
3.5.2 Results 63

Chapter 4 Electromagnetically Induced Transparency 67
4.1 Theory 67
4.1.1 Mathematical Model for EIT 68
4.1.2 EIT in Diamond 70
4.2 Experimental Setup 71
4.3 Results 75
4.3.1 Magnetometry 76
4.3.2 Electrometry 78

Chapter 5 Conclusion 82

References 83

Appendix : MATLAB Code 95

List of Figures

1.1 Three symmetries of interest in particle physics - charge (C), parity (P) and time (T) 1
1.2 The Wu experiment demonstrated the violation of P symmetry. The ^{60}Co atoms aligned in a magnetic field were shown to have a preferential direction for beta decay. 2
1.3 A hypothetical neutron which carries both, electric and magnetic dipole moments. P and T operations do not conserve the symmetry of this particle. Time reversal causes the neutron to spin backwards, reversing the direction of spin. The parity operation flips the direction of its electric dipole moment 3
1.4 The upper bound on the neutron EDM through the years as established by different experiments, adapted from [6]. The standard model predicts a value of the neutron EDM that is too low for the baryon asymmetry. The sensitivity goal for the new nEDM experiments is shown in blue. 4
1.5 A drawing of the proposed nEDM experiment at the Spallation Neutron Source (SNS) at Oakridge National Laboratory (ORNL) 7
1.6 An NV center in a host diamond lattice marked by grey spheres. The axis connecting the vacancy to the nitrogen atom determines the quantization axis of the NV center, $\hat{z}$. 9
1.7 Comparison of different magnetic field sensing techniques. Diamond magnetometers offer high sensitivity at nanoscale resolutions. Adapted from [16]. 9
1.8 Energy levels of the NV center. Optical transitions are seen on the left, the phonon-free zero phonon line is at 637 nm. The defect can also be excited with off-resonant optical radiation. The figure on the right shows the ground state structure which is an orbital singlet state. Hyperfine interactions lead to a total of nine energy levels. Transitions between these nine states can be driven with microwaves that preserve the nuclear spin projection ($\Delta m_I = 0$) 10
1.9 a) The fluorescence spectrum of NV center at room temperature (300 K) and with liquid nitrogen (77 K) where sharp zero phonon lines for the NV^0 and NV^- center can be observed. b) Absorption spectrum for the NV center at 300 K. An additional unknown absorption feature is observed at 595 nm which has been attributed to radiation damage in nitrogen-containing diamonds [17]. c) A HPHT(high pressure high temperature) diamond with a high NV concentration emits a pinkish-red fluorescence under a confocal microscope. 11

1.10 Simulated magnetic field induced Zeeman shifts of the ground state energy levels, $m_s = +1$ (solid) and $m_s = -1$ (dashed) for a) no strain b) with a strain equivalent to 15 kV/cm. Strain induced avoided crossing between the $|m_s = \pm 1, m_I = 0\rangle$ sublevels (blue) occurs at 0 μT, between the $|m_s = \pm 1, m_I = +1\rangle$ sublevels (red) at 77 μT and $|m_s = \pm 1, m_I = -1\rangle$ sublevels (green) at -77 μT. . 14
1.11 FTIR spectrum of E6-HPHT-1 diamond. Both marked spectral lines are associated with the nitrogen defect. 18
1.12 The visible absorption graph of diamond WD-CVD-3a before annealing (blue), after annealing at 600 C (green) and finally after annealing at 750 C (red). Four defect centers are identified here - the ND1, NV^-, NV^0 and the GR1 center, these are associated with the negatively charged vacancy, the negatively and positively NV center and the neutral vacancy respectively. A decrease (increase) in the vacancy (NV center) absorption lines is observed after each annealing step. 19

2.1 The mechanism for optically detected magnetic resonance (ODMR). a) The ground state sublevels are equally populated (unless the temperature is < 1 K or exceptionally high magnetic fields are being used (B> 1 T); neither condition applies for the work discussed here. A green laser pulse drives transitions to the excited state via spin preserving optical optical transitions. b) The excited state, $m_s = \pm 1$ sublevels decay preferentially via the ISC into the ground state $m_s = 0$ sublevel. The excited state $m_s = 0$ sublevel only decays radiatively. c) The ground state is now polarized in the $m_s = 0$ sublevel. d) Resonant microwaves are applied to the ground state, driving electrons from the $m_s = 0$ to the $m_s = \pm 1$ sublevels. e) Green laser again drives optical transitions to the excited state. Since these transitions are spin conserving, the excited state sublevels $m_s = \pm 1$ are more heavily populated. e) The excited state decays to the ground state but now there are fewer electrons occupying the $m_s = 0$ state. The visible fluorescence is attenuated because more electrons decay through the non-radiative pathway. 22
2.2 Magnetic transitions observed in the ground state of the NV center, as per the selection rules (2.1). As the microwave frequency is swept across the $m_s = \pm 1 \leftrightarrow m_s = 0$ transitions, six dips in the fluorescence are observed on resonant excitation. The width of these transitions is about 0.5 MHz and is typically larger for samples with higher NV concentrations. 24
2.3 Experimental setup for ODMR experiments. The confocal microscope allows a small volume to investigated to minimize the magnetic and electric inhomogeneities in the investigated region. This figure has been adapted from [65]. 24
2.4 Reflection observed from the front and rear face of the diamond. This allows us to estimate the axial resolution of our confocal microscope. The two peaks are separated by the width of the diamond (400 μm). Our axial resolution is estimated to be about 80 microns using this method. The red curve is recorded without a pinhole before the detector. 26

2.5 a)By rotating the polarization of the green laser, we can select pairs of NV centers from the four found in the ensemble. b) The measured ODMR contrast observed for pairs of NV axes as a function of the green lasers polarization angle. We can turn off the resonances from NV centers 1 and 2 if the polarization of the green laser is horizontal in the lab frame. c) ODMR spectrum for horizontally polarized light (orange) and vertically polarized light (blue). We see two sets of twelve resonances, corresponding to pairs of NV axes. 27
2.6 Strain-induced Stark shift observed near a magnetic field of about $-77\,\mu T$. The outer four resonance lines have been fit to Lorentzian lineshapes while the inner peaks have been fit to asymmetric Doniach-Sunjic[77] profiles with an asymmetry parameter, $\alpha \approx 0.2$. 29
2.7 The asymmetry parameter, α, as a function of the magnetic field. The lineshape becomes more asymmetric as the resonances approach the avoided crossing and the strain mixes the $m_s = \pm 1$ sublevels. 30
2.8 The green curve shows the magnitude of the laser light that is reflected from the top and bottom faces of the diamond. The red curves represent the intensity of the 637-nm ZPL. Applying an electric field increases the observed fluorescence at the NV center ZPL. Curves are rescaled for clarity. The blue data points show the strain measured as a function of depth in the diamond. This figure has been adapted from [65]. 31
2.9 Three degenerate [100] directions with respect to the four equivalent [111] NV center axis. The diamond is grown in the [100] direction. 32
2.10 a) Schematic illustrating the two NV orientations used to measure the strain direction. The white ellipses represent the plane in which the transverse magnetic field ($B_\perp \approx 1$ mT) is rotated. Strain direction as determined by the polar plots of the Stark shift is drawn in orange. The green arrows represent the initial direction of the magnetic field ($\theta = 0^\circ$ in the graphs below). b) Change in strain-induced Stark shift as a function of the polar angle of the transverse magnetic field for the two NV orientations. Dashed black lines show the lines connecting the vacancy to the three adjacent carbon atoms. Here the strain-induced Stark shifts are measured in kV/cm. The orange vector represents the strain as it projects on the transverse plane and the shaded region represents the uncertainty associated with the strain measurements. Simulated data is shown as a the blue curve. This figure has been adapted from [65]. 33
2.11 Chromium electrodes printed on a CVD diamond. a) In this geometry, the applied electric field is degenerate on pairs of NV axis. b) A second electrode geometry allowed arbitrary electric field direction to be established in the center by applying different voltages on the four pads. Fig.a) has been adapted from [62]. . . 34

2.12 COMSOL simulation of electric fields within diamond. The electrodes (white) are separated by the distance of 80 microns. An electric potential of 2500 V is applied on the right electrode. The bottom face of the diamond and the left electrode are grounded. A high region of electric fields is observed near the electrodes and it drops off quickly with depth in the diamond. The white arrows represent the electric field vector. 35
2.13 Electric field-induced Stark shift observed near a magnetic field of about $-77\,\mu T$. a) This data is recorded with a pinhole; the Stark-shifted resonance lines do not broaden appreciably b) The pinhole is removed for this data. The Stark-shifted lines broaden when the electric field is applied because of the large electric field inhomogeneity in the probed region of the diamond. 36
2.14 Stark shifts for six hyperfine transitions for different electric fields. The blue lines represent the values derived from the ground state Hamiltonian. The inner resonances tune the most as a function of an applied electric field. This figure has been adapted from [62]. 38
2.15 Stark shift as a function of axial magnetic field. Solid lines are the three predicted Stark shifts derived from the ground state Hamiltonian. An increase in electric field sensitivity is observed at magnetic fields of B=0 μT and B = $\pm$77 μT. This figure has been adapted from [62]. 39
2.16 Difference in fluorescence at 0 V (blue), 2500 V (red) and their difference (yellow). There is an almost 100% increase in fluorescence from the NV^- ZPL when an electric field is applied. This figure has been adapted from [65]. 39
2.17 Electric field measured between electrodes, about 200 μm inside the diamond. The gap at its minimum is about 80 μm. The electric field magnitude has been color coded. This figure has been adapted from [62]. 41
2.18 Electric field measured as a function of depth the diamond. The simulated data is obtained from finite element analysis done in COMSOL[78]. This figure has been adapted from [65]. 41

3.1 Energy level scheme for the two ground states used in the NV center. Coherent microwave radiation is applied to prepare the state in a particular superposition of the two states. 43
3.2 An arbitrary state on the Bloch sphere with the polar, ϕ and azimuthal angle, θ. Purely coherent states lie in the x-y plane. Statistical distributions with no coherence are restricted to the z-axis and have no x or y components. 44
3.3 Approximate coupling strengths between different impurities. The NV centers(red) are drawn along the same [111] direction. ^{13}C nuclei(black) are oriented randomly and form the spin-bath for the NV center. Given the low intra-bath coupling between the NV centers, the ensemble can be modelled as an aggregate of non-interacting NV-^{13}C bath spin systems. 46
3.4 Detection scheme used for observing spin dynamics of NV centers. The laser is modulated at twice the detection frequency. The lock-in amplifier effectively measures the emitted fluorescence signal with microwaves and green laser minus the fluorescence induced from the undriven spin system. 49

3.5 a) Antenna design used to observe spin dynamics. A 50 Ohm impedance matched line is used to feed the microwaves. The diamond is placed in the center region which is about 1 mm in diameter. b) Antenna with shorter feed line so it could be placed in the cryostat buffer window. c) and d) Half and full-wavelength loop antennae. e) Patch antenna with half-wavelength sides (10.4 cm) 50
3.6 Pulse scheme used for Rabi oscillations. The green laser first prepares the state into the $m_s = 0$ state. Resonant microwaves are then applied for a variable time τ. The final green pulse projects the $m_s = 0$ component on the vertical axis. 51
3.7 a) Simulated evolution of the spin-vector in the Bloch sphere with time constants, $T_1 = 1\ ms$ and $T_2 = 1\ \mu s$. b) Rabi curve obtained from an ensemble of NV centers. The spin oscillates coherently between the $m_s = 0$ and $m_s = 1$ states. The Rabi frequency is 0.62 MHz. The bright and dark states are distinguishable because of the preferential non-radiative intersystem crossing from the $|m_s = 1\rangle$ excited state. 53
3.8 Rabi frequency plotted against the input microwave power. We can see that the Rabi frequency scales as the square root of the microwave power or linearly with the magnetic field component of the microwaves. 55
3.9 a) The diamond is mounted on the right edge of a circular antenna. b) Rabi frequency of the ensembles within the diamond as it is scanned under the confocal microscope. There is a sharp dip in the Rabi frequency at the edge of the printed trace. . . . 56
3.10 Pulse sequence used for free induction decay (FID) measurements. The spin is first prepared in the $m_s = 0$ state. It is then irradiated with a resonant microwave pulse of duration $\pi/2$. The created superposition is allowed to evolve under its internal Hamiltonian. The coherence is lost primarily through the thermal noise of the surrounding bath spins. The spin is then coherently projected on the $m_s = 1$ state with a second $\pi/2$ pulse. The phase accumulated in the FID is converted into a population difference between the $m_s = 0$ and $m_s \pm 1$ levels with the green laser. 58
3.11 Free induction decay curves observed in the ground state. The top curve represents the free induction decay between the magnetic sublevels $|m_s = 0, m_I = 0\rangle$ and $|m_s = -1, m_I = 0\rangle$. The adjacent resonances are also being driven and since they are detuned by a frequency of about 2.1 MHz, a beating at the same frequency is observed. The bottom curve shows FID when the microwave frequency is parked at the other resonance ($m_I = -1$). Here two frequencies can be observed, 4.09 MHz and 1.95 MHz. These frequencies match the hyperfine splittings shown in Fig. 2.2. . . 60
3.12 Pulse sequence used for Hahn-echo spin decoupling. First the spin is pumped into the $m_s = 0$ state with non resonant green excitation. A resonant $\pi/2$ pulse tips the spin into the x-y plane of the Rabi sphere thus creating spin coherence which then evolves with a characteristic time, T_2^*. The second microwave pulse has a duration of π, this flips the spin by 180 degrees. The effective reflection of the spins reverses their dephasing. Therefore, an echo is formed a time τ, after the π pulse. 62

3.13 Hahn-echo decay curve. The recurrence rate for the echoes matches the Larmor frequency of the ^{13}C spin bath. After $t > T_2$, the echoes cannot be revived because of nuclear pair spin dynamics in the spin bath. 63
3.14 Multiple Hahn-echo curves plotted vs magnetic field. The darker blue colorings indicates a spin revival. As the magnetic field increases, the spacing between the echo revivals is reduced. This interval is equal to the Larmor period of the ^{13}C nuclei. The red line represents the T^2 time, it was obtained by fitting individual Hahn echo curves to Eq. (3.21). It can be seen that the T_2 time increases with an increasing magnetic field, as suggested by numerical simulations[39] 64
3.15 The behavior of the different time constants in the Hahn Echo sequence. T_R is the spin echo revival period and is inversely proportional to the Larmor precession rate of the ^{13}C nuclei. T_2 is the decoherence time of the spin echoes and T_w is the half-width of all coherence peaks within a single Hahn echo curve. 66

4.1 Three possible level schemes for EIT - a) Λ-system b) ladder system c) V-system. The allowed dipole transitions are drawn with red arrows. We realize the Λ system in the NV center to demonstrate EIT. 68
4.2 Ground and excited state energy levels as a function of strain. The E_x excited states make possible the non-cycling transitions required for a Λ-system while the E_y states displays only spin-conserving transitions on account of the unmixed $(S_{x,y}) \leftrightarrow S_z$ spin character. 70
4.3 a) The diamond is cleaved on one corner to create a waveguide which allows multiple passes of the green and red lasers through total internal reflection. A red filter is used to track the optical path traced inside the diamond. b) Zero phonon line observed at 77 K. An optical depth of 4.5 (99% absorption) is achieved in this configuration. 72
4.4 Experimental setup for EIT experiments with diamond. The green and red laser beams are combined with a dichroic mirror and alternatively chopped at 500 Hz. The diamond is held in a liquid helium cryostat which has a quartz window for optical access. 73
4.5 EIT features observed in diamond. The top figure shows a broad anti-hole which is a result of optical pumping. The width of this feature is about 80 MHz. The bottom graph shows the narrow EIT resonances at the bottom of the anti-hole. These are increases in transmission and have a narrow spectral width of $\nu_{EIT} = 350\ kHz$. 74
4.6 Difference in EIT contrast when the green laser is turned off and when it is turned on. The green laser is thought to undo the bleaching effect from the red laser[15] 75
4.7 EIT spectra for three different magnetic fields. The bottom spectrum was recorded for earth's magnetic field, $B \approx 50\ \mu T$. The other two were taken with magnetic fields aligned in the (100) diamond direction. 77

4.8 Illustration of the diamond mounted in the cryostat. An ITO coated glass slides is used to apply an electric field across the diamond. The electric field is degenerate across all four NV axes. 78
4.9 COMSOL simulation of the diamond with the electrodes configuration described in the text. The bottom of the diamond is grounded and there is an ITO coated coverslip about 200 μm from the top of the diamond. The coverslip is held at V = 3000 V in this simulation. The electric field within the diamond is largely homogeneous. 79
4.10 a) Electric field induced Stark shifts in the EIT spectrum. The Stark shift of the inner resonances is plotted vs the applied voltage at the ITO electrode. b) EIT data recorded at V = - 3000 V and V = 2750 V. 80
4.11 COMSOL simulation of two diamonds oriented parallel and perpendicular to an electric field. The dielectric screening effect is enhanced when the diamond is oriented perpendicular to the electric field. 81

Chapter 1

Introduction

1.1 nEDM

One of the greatest puzzles in cosmology is the matter-anti-matter asymmetry in the universe. Why is there such a preponderance of matter in the universe while anti-matter is largely confined to high energy particle accelerators and cosmic rays? One possible explanation to this problem is linked to the potential existence of an electric dipole moment on the neutron. The nEDM collaboration seeks to measure this charge separation of a neutron through an experiment which measures changes in the spin precession frequency of neutrons in the presence of electric and magnetic fields. Precise measurements of the properties of the neutron can help us test the violations of fundamental symmetries and push the boundaries of the Standard Model.

1.1.1 Symmetries

The idea of symmetry has played a crucial role in the world of modern physics. We can start to think about symmetry as a transformation performed on a physical system, object or law under which it remains invariant. Perhaps the most intuitive object to imagine here is an idealized sphere, which we can rotate about any axis without modifying it. Thus we can conclude the sphere must possess rotational symmetry. However the idea of symmetry can be extended beyond physical space, to transformations that can be applied to physical laws.

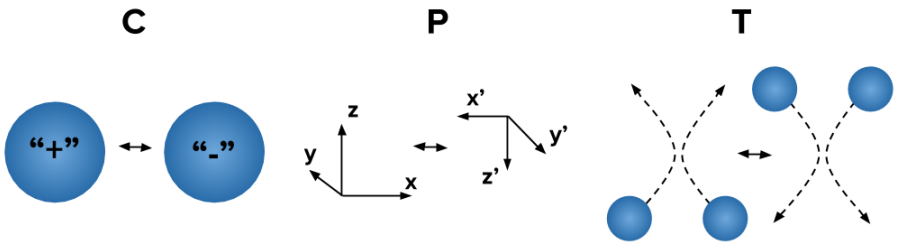


Figure 1.1: Three symmetries of interest in particle physics - charge (C), parity (P) and time (T)

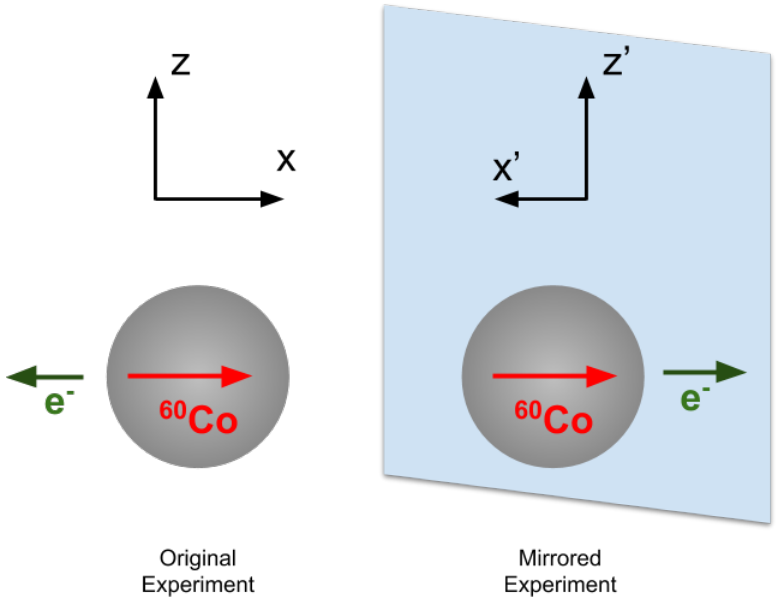


Figure 1.2: The Wu experiment demonstrated the violation of P symmetry. The ^{60}Co atoms aligned in a magnetic field were shown to have a preferential direction for beta decay.

In particle physics, there are three significant symmetries of interest - charge conjugation (C), parity (P) and time reversal (T). Charge conjugation substitutes all particles with their corresponding anti-particles, thus switching their charge (electron vs positron), lepton number and baryon number. Parity simply flips the system through the origin, thus switching all three co-ordinate axes. A system that preserves time reversal symmetry would appear invariant if we could record it and play it backwards. These symmetries are illustrated in Fig. 1.1.

1.1.2 Symmetry violation

Intuitively, it appears that the universe and physical laws should preserve the these symmetries. In confidence of the parity symmetry, Wolfgang Pauli wrote in 1957, "I do not believe that God is a weak left hander"[1].

However, the parity symmetry was soon shown to be decidedly broken. In an experiment designed to test parity conservation[2], nuclei of cobalt-60 were polarized in a strong magnetic field at a low temperature (3 mK). The radioactive cobalt decayed into nickel-60 by giving off an electron, an electron anti-neutrino and two photons

$$^{60}_{27}Co \rightarrow ^{60}_{28}Ni + e^- + \bar{\nu}_e + 2\gamma \tag{1.1}$$

The emitted electrons were counted with the use of scintillators. This beta decay occurs under the weak force, and if the parity of the weak interaction is to

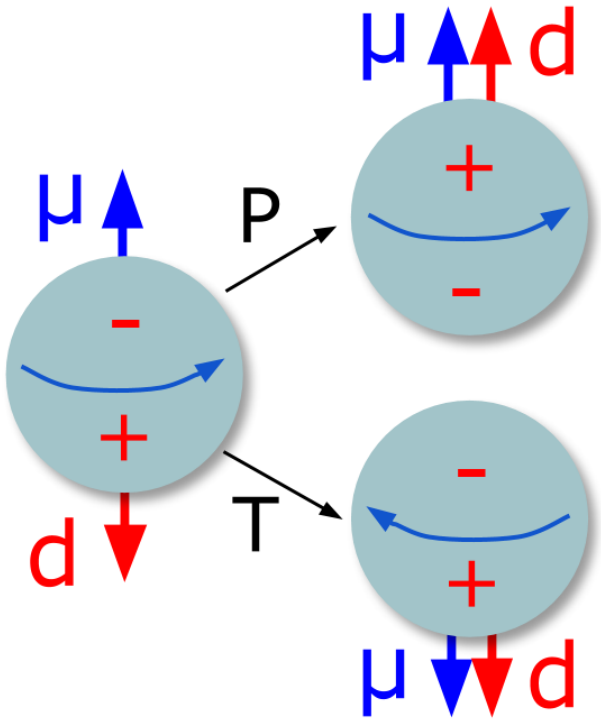


Figure 1.3: A hypothetical neutron which carries both, electric and magnetic dipole moments. P and T operations do not conserve the symmetry of this particle. Time reversal causes the neutron to spin backwards, reversing the direction of spin. The parity operation flips the direction of its electric dipole moment

be conserved, electrons emitted parallel and anti-parallel to the aligned cobalt spin must be equal in number. But the experiment revealed a preferential direction for the electrons to be emitted: it was opposite to the alignment of the nuclear spin. To see how this breaks parity, we can imagine an identical but mirrored experiment in which the cobalt-60 nucleus is still spinning in the same direction, hence its spin also points towards the right as shown in Fig. 1.2. But now the electrons are preferentially emitted in a direction parallel to the nuclear spin. This means we cannot neatly map the original experiment on to its mirrored version and its symmetry is not conserved.

This unexpected result of parity violation was a watershed moment. The universe was found to be playing favorites when it came to symmetries that were previously thought immutable. This led to several other experiments that were designed to test the conservation of other symmetries. In 1964, the violation of stronger, combined CP symmetry was discovered in the decay of neutral kaons [3]. A plethora of other experiments like BaBar experiment at SLAC, LHC at CERN and the Belle collaboration have confirmed the limited role of CP violation in the Standard Model.

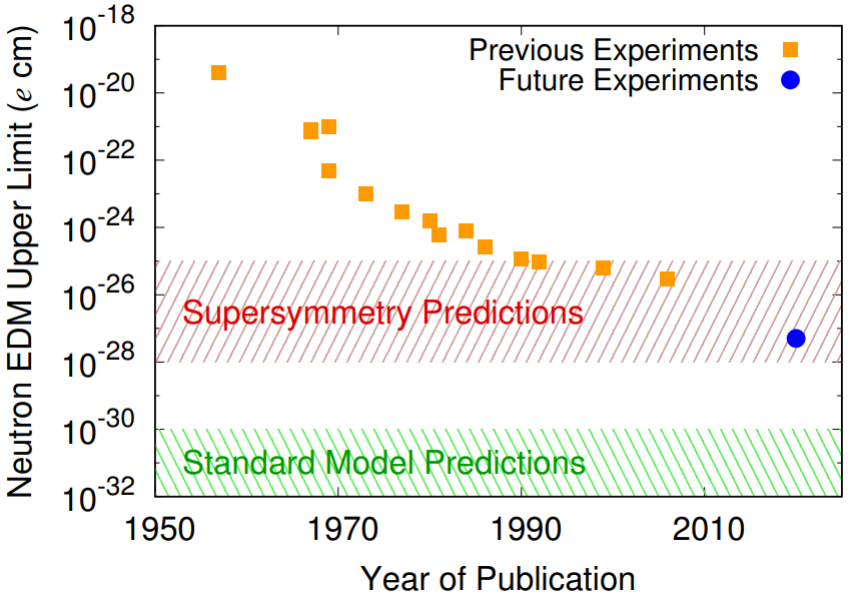


Figure 1.4: The upper bound on the neutron EDM through the years as established by different experiments, adapted from [6]. The standard model predicts a value of the neutron EDM that is too low for the baryon asymmetry. The sensitivity goal for the new nEDM experiments is shown in blue.

1.1.3 Baryon Asymmetry

Baryon asymmetry addresses the fundamental question of why the universe exists. Based on our current understanding of the Big Bang, fourteen billion years ago, the universe had equal number of matter and anti-matter pairs. As the universe cooled, the pair-wise annihilation of matter and anti-matter particles took place. But there was a difference in the way that the laws of physics treated matter and anti-matter. A little bit of matter (one part in ten billion) survived and formed the universe we see today [4]. It has also been shown that a necessary condition for this asymmetry is the violation of C and CP symmetry[5].

The degree of CP violation that been measured so far cannot solve the baryon asymmetry puzzle. Thus we must search for the missing CP violation in other systems.

1.1.4 Symmetry violation in the neutron

The neutron is electrically neutral on the whole but it is comprised of charge carrying constituents: one 'up' and two 'down' quarks. So the neutron could have distributions of positive and negative charges that do not perfectly eclipse each other. This would lead to the neutron possessing an electric dipole moment.

To understand how the existence of a neutron electric dipole moment could be problematic for symmetry, let us start with the supposition that the neutron does carry a non-zero electric dipole moment, $\vec{d}$ as shown in Fig. 1.6. The neu-

tron's magnetic moment has already been measured, and it has a corresponding vector, $\vec{\mu}$. Now we perform symmetry operations on this hypothetical neutron.

A time reversal operation, as shown in the bottom of Fig. 1.6 will cause the spin to be reversed and hence the spin vector will now be parallel to the electric dipole moment. This new neutron has spin $\vec{\mu}$ parallel to the electric dipole moment, $\vec{d}$ and hence cannot be rotated back to its original state. This indicates that time reversal symmetry is not conserved.

In another test for symmetry, we can apply the parity operation which will flip the electric charge distribution, changing the direction of $\vec{d}$. Being the cross product of two polar vectors($\vec{r}$ and $\vec{v}$), the pseudovector, $\vec{\mu}$ is invariant under this transformation, we again end up with parallel spin and electric dipole moment vectors.

According to the CPT theorem[7], a violation of time reversal also violates CP symmetry(and vice-versa). So the existence of a neutron EDM would lead us to some degree of CP violation and it might help solve the baryon asymmetry puzzle.

The first experiment to measure the neutron EDM was carried out by Smith, Purcell and Ramsey [8] in 1950 at the Oak Ridge reactor. Their efforts constrained the neutron electric dipole moment to $|d_n| < 5 \times 10^{-20}$ e cm.

Since 1950, there have been several efforts to detect neutron EDM. The successive experiments have tightened the constraints by reducing the maximum possible value (see Fig. 1.4). The current best upper limit for the nEDM, measured at the Institut Laue-Langevin (ILL), Grenoble[9] stands at

$$|d_n| < 3 \times 10^{-26} \text{e cm [90\% C.I.]} \tag{1.2}$$

1.1.5 nEDM Experiment at SNS

The operating principle behind the nEDM experiment is based upon the change in Larmor precession frequency under reversal of electric and magnetic fields. Assuming a non-zero electric dipole moment $\vec{d_n}$, we can write the neutron Hamiltonian as

$$H = -(\vec{\mu}_n.\vec{B} + \vec{d}_n.\vec{E}). \tag{1.3}$$

We can re-write this as

$$H = -(\mu_n \vec{I}.\vec{B} + d_n \vec{I}.\vec{E})/I. \tag{1.4}$$

The electric dipole moment must align itself with $\vec{I}$ since the ground state can be completely characterized by the nuclear spin projection[10]. We can now calculate the energy shifts associated with the electric and magnetic fields

$$\begin{aligned} \Delta E_{elec} &= \hbar\omega_B = 2\mu_B B \\ \Delta E_{mag} &= \hbar\omega_E = 2d_n E. \end{aligned} \tag{1.5}$$

These energies can either add or subtract depending on if the electric and magnetic fields are parallel or anti-parallel. Here, we assume $\vec{d}$ and $\vec{\mu}$ are parallel:

$$\begin{aligned} E_{\uparrow\uparrow} &= \hbar\omega_{\uparrow\uparrow} = 2(\mu_n B + d_n E) \\ E_{\uparrow\downarrow} &= \hbar\omega_{\uparrow\downarrow} = 2(\mu_n B - d_n E). \end{aligned} \tag{1.6}$$

Subtracting these two equations, we get

$$\hbar\Delta\omega = \hbar(\omega_{\uparrow\uparrow} - \omega_{\uparrow\downarrow}) = 4d_n E. \tag{1.7}$$

So if we can track this change in precession frequency as a function of parallel and anti-parallel electric fields, we have a measure of the neutron EDM

$$d_n = \frac{\hbar\Delta\omega}{4E}. \tag{1.8}$$

Ultra cold neutrons

The first nEDM experiment was performed with a beam of neutrons which have a very limited measurement time. The current generation of nEDM experiments instead use slow-moving ultra cold neutrons (UCNs) which provide a sensitivity that is orders of magnitude higher. The measurement time with UCNs is expected to be around 500 seconds[11]. The systematic effects of inhomogeneous fields(e.g. motional) would also be reduced with UCNs[10].

^{3}He co-magnetometer

The nEDM experiment at SNS will be carried out in a bath of superfluid liquid helium where cold neutrons are slowed down and converted into UCNs via a downscattering process. The small nuclear cross section of the helium nucleus allows the UCNs to be stored until they β-decay. Another purpose of using a liquid helium bath is its large dielectric strength which allows a large electric field to be established over the measurement region. The helium in this bath would be isotopically purified ^{4}He.

The helium bath will also contain an admixture of dissolved polarised ^{3}He which plays two important roles - as a co-magnetometer and a neutron spin analyzer.

Since the ^{3}He shares the same volume with the neutrons and has a non-zero (nuclear) magnetic moment, it can serve as a sensitive magnetometer that can correct for drifts in magnetic fields. Importantly, it would be largely insensitive to electric field changes since the electric dipole moment of ^{3}He is negligible. This is because the electron cloud shields the helium nucleus from external electric fields. This is called the Schiff effect[12] and it reduces the atomic EDM of most bare nuclei by several orders of magnitude[13].

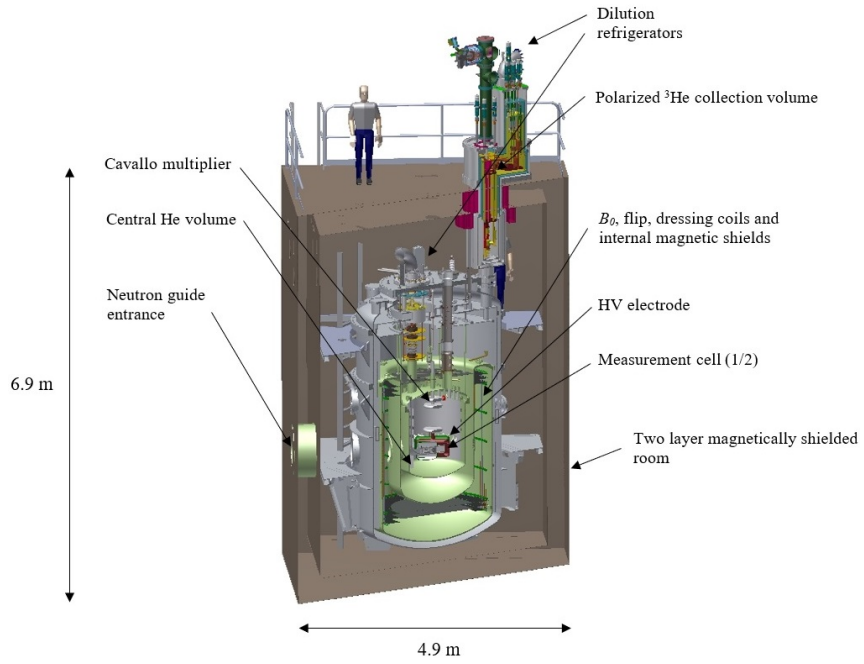


Figure 1.5: A drawing of the proposed nEDM experiment at the Spallation Neutron Source (SNS) at Oakridge National Laboratory (ORNL)

The second role of ^{3}He is as a neutron spin analyzer. The helium nucleus can capture a neutron via the following process

$$n +^3 He \rightarrow^3 H + p + 764 \text{ keV} \tag{1.9}$$

This process is highly spin-dependent. Here the cross-section ratio for parallel and anti-parallel spins is about 1:200[10]. The scintillation produced from the charged protons and tritium in the liquid helium can be detected with photo-multiplier tubes.

The gyromagnetic ratio(ratio of magnetic moment to angular momentum) of helium-3 is about 10% larger than that of the neutron. The scintillation light then reflects the relative precession rate of the ^{3}He and the neutrons.

A CAD drawing of the nEDM apparatus is shown in Fig. 1.5. μ-metal shielding has a high permeability and protects the experiment from static and slowly varying magnetic fields. The neutron beam on the right is delivered from the spallation neutron source (SNS)[14].

The cryostat is divided into two parts. The upper cryostat consists of the dilution refrigerators and the polarised helium-3 source. The lower cryostat contains the magnetic shielding, measurement cells, the HV electrodes and the entrance port for the neutrons.

The projected sensitivity of the nEDM experiment is a few times x 10^{-28} e cm, a hundred times lower than the current limit. At an electric field of

50 kV/cm, averaged over the entire experiment, the differential shift would be $\approx$ 2 nHz which corresponds to a sub-femtoTesla magnetic field. The nEDM has requirements for both high-sensitivity electric and magnetic field sensors. (Despite the canceling out of B in the expression for the neutron electric dipole moment, a temporal shift in B over the measurement period could lead to a false measurement.)

The sensors designed must be able to function at the nEDM operating temperature of 0.5 K and must also themselves be magnetically inert. The latter requirement precludes sensing techniques that require alternating magnetic fields and wires needed to deliver them. Thus nEDM needs an all-optical method for electric and magnetic field sensing.

Alkali vapor cells can be used as optical probes for magnetic fields but they cannot be used in the cryogenic regions of the nEDM. SQUID devices consist of wire leads and must be treated very carefully. Fluxgate sensors are themselves magnetic.

The NV center in diamond offers a robust solid-state method with a small electric and magnetic field signature. The feasibility of an all-optical diamond magnetic field sensor at 4 K has already been demonstrated [15]. The diamond project for nEDM has taken that work further and investigated the electric field sensing capabilities of the NV center using both, all-optical and more generally RF induced electron spin resonance techniques.

1.2 The NV Center

Diamonds are comprised of carbon atoms arranged in a tetrahedral lattice. Diamonds with few impurities are clear while a colored diamond is generally an indication of substitutional or interstitial impurities in the carbon lattice. Hundreds of naturally occurring and artificially created defect centers in diamonds have been identified [17].

The NV center in diamond is one such defect where a nitrogen atom sits adjacent to a vacancy center. Depending upon the electric charge, three species of NV centers exist - NV^0, NV^- and NV^+ [18, 19]. However, only the negatively charged, NV^- center is magneto-optically active. The NV center can switch between its charge states under optical illumination[20] and, as will be shown later, with application of static electric fields as well.

The NV center acts as a paramagnetic (spin-1) pseudo-atom which sits securely in a largely inert and transparent diamond lattice. It has its own electronic structure which turns out to be very practical with optical transitions in the visible range and magnetic sublevels that are easily addressable. In isoptically pure, ^{12}C samples, the ground state has long lived coherence times, exceeding 1 second in certain decoupling regimes [21]. The free evolution time is typically in the microseconds range, depending upon the concentration of other magnetic impurities.

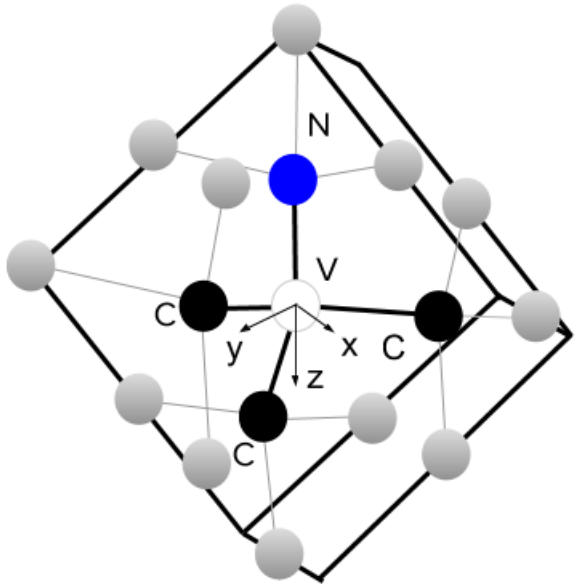


Figure 1.6: An NV center in a host diamond lattice marked by grey spheres. The axis connecting the vacancy to the nitrogen atom determines the quantization axis of the NV center, $\hat{z}$.

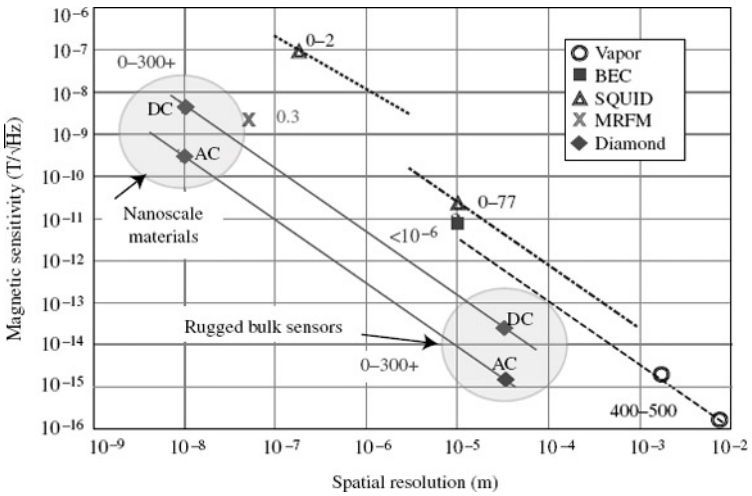


Figure 1.7: Comparison of different magnetic field sensing techniques. Diamond magnetometers offer high sensitivity at nanoscale resolutions. Adapted from [16].

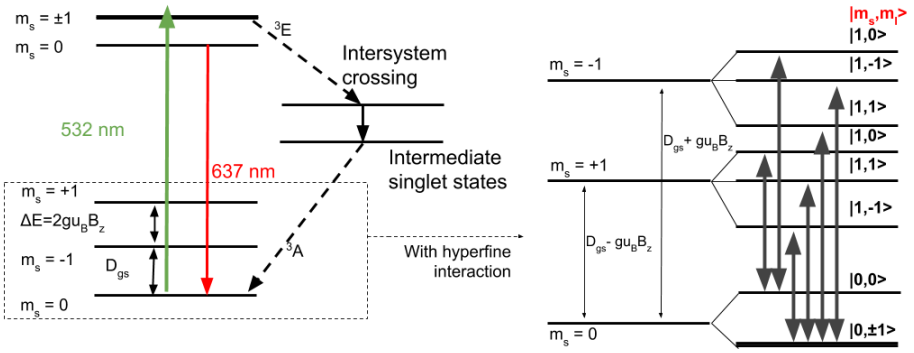


Figure 1.8: Energy levels of the NV center. Optical transitions are seen on the left, the phonon-free zero phonon line is at 637 nm. The defect can also be excited with off-resonant optical radiation. The figure on the right shows the ground state structure which is an orbital singlet state. Hyperfine interactions lead to a total of nine energy levels. Transitions between these nine states can be driven with microwaves that preserve the nuclear spin projection ($\Delta m_I = 0$)

The easiest way to probe these ground state transitions is through a technique called optically induced magnetic resonance (ODMR) which reveals narrow resonance lines, about 500 kHz wide that can be easily observed in diamonds containing NV centers. For sharp optical transitions the diamond must be cooled to cryogenic temperatures as will be shown later.

For higher sensitivity applications, ensembles of NV centers are usually employed while single NV centers are used as probes with high spatial sensitivity[22]. The high photo-stability of NV centers makes single defects easy to locate in sparse diamonds [23].

These properties make the NV center an attractive tool for many applications. NV defects have proved to be useful sensors for detecting magnetic fields[24, 25, 26], electric fields[27] and temperature[28, 29]. In comparison to other magnetometer technologies, NV centers offer very high, close to atomic, spatial resolutions as shown in Fig. 1.7. The non-cytotoxicity of diamond lends itself to use in biomedical imaging as biomarkers[30]. NV defects have also served as a playground for testing esoteric quantum phenomena like entanglement [31], slow light[32] and coherent population trapping (CPT)[33] .

1.2.1 Electronic Structure

The NV center is host to six electrons - two are from the dangling nitrogen bond, three from the adjacent carbon atoms and one is captured from the lattice, usually from another nitrogen site[34]. (Hence the NV production yield is always less than half that of the nitrogen concentration we begin with). An NV center without the extra captured electron is in the NV^0 state. These six electrons form ground and excited state spin-triplets that are split by an optical transition of 1.945 eV (637 nm). Apart from spatial isolation, the wide bandgap of diamond

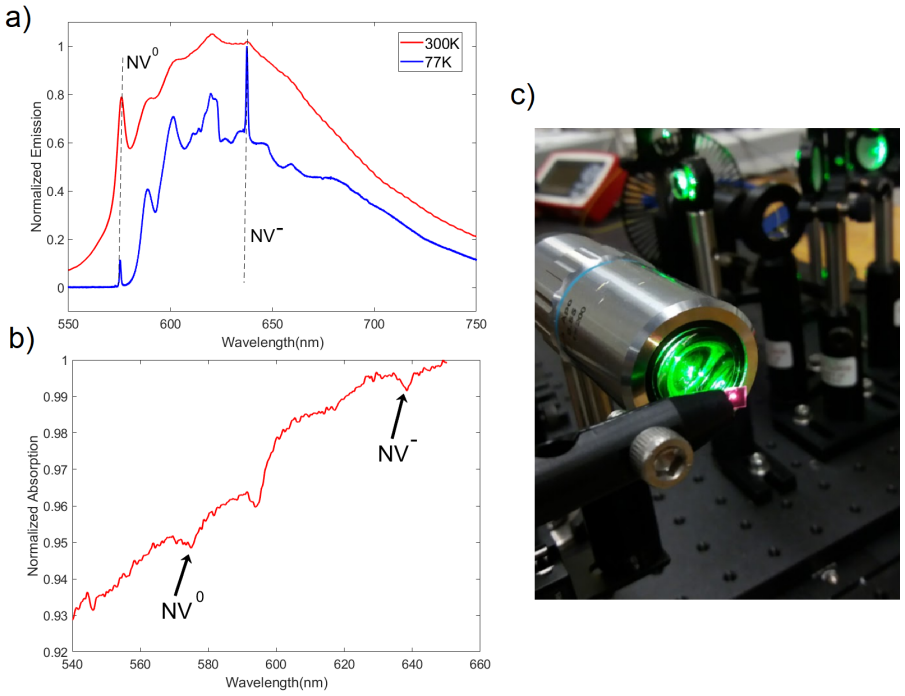


Figure 1.9: a) The fluorescence spectrum of NV center at room temperature (300 K) and with liquid nitrogen (77 K) where sharp zero phonon lines for the NV^0 and NV^- center can be observed. b) Absorption spectrum for the NV center at 300 K. An additional unknown absorption feature is observed at 595 nm which has been attributed to radiation damage in nitrogen-containing diamonds [17]. c) A HPHT(high pressure high temperature) diamond with a high NV concentration emits a pinkish-red fluorescence under a confocal microscope.

(5.5eV) also offers a large electronic buffer to the NV center electronic structure which lies well below diamond's conduction band [35]. The energy structure is illustrated in Fig. 1.8.

The 1.945 eV optical transition can be resonantly driven with a red laser (637 nm) but more conveniently it can also be driven off-resonantly by the ubiquitous green laser. Since the spin-orbit coupling is very weak[36], optical transitions are generally spin conserving, $\Delta m_s = 0$. Owing to broad phonon-induced sidebands, illumination of the NV center results in broad features extending out to 800 nm. Phonon sidebands in the emission and absorption spectrum are suppressed at cryogenic temperatures[37]. Absorption and emission spectra of a low NV concentration diamond are shown in Fig. 1.9. Both, NV^- and NV^0 features can be identified along with a host of other impurities which have not yet been assigned. Differences in observed concentrations of the two NV charged states generally depend on the wavelength of the illumination. Shorter wavelengths lead to a higher transition rate from NV^0 to NV^-[18].

A side-channel also exists as a mechanism for relaxation from the excited state. The intermediate singlet states associated with this transition selectively shelve the excited state $m_s = \pm 1$ sublevels into the $m_s = 0$ ground state. An infrared transition at 1046 nm, between two singlet states has been identified with this intersystem crossing (ISC)[38].

The mechanism of the ISC is a useful way to polarize the ground state of the NV center. Since the decay from the $m_s = \pm 1$ excited states is partially non-radiative, the emitted fluorescence also lets us measure the degree of polarization of the ground state[26]. This trick is used to detect the evolution of the ground state spin as it lets us extract the $m_s = 0$ character of a prepared coherent state as it moves under driving pulses and decohering processes. This is discussed further in chapter 4.

The total ground state Hamiltonian can be written as

$$\hat{H}_{gs} = \hat{H}_{hfs} + \hat{H}_{es}\,. \tag{1.10}$$

$\hat{H}_{hfs}$ is the hyperfine coupling interaction with the adjacent nitrogen nucleus (^{14}N, spin-1). The hyperfine interaction can also include contributions from spin-1/2 ^{13}C and other nitrogen nuclei (P1 centers) but these magnetic interactions are averaged out in the ensemble and can be estimated as a random dipolar field, δB_z [39]. The nitrogen hyperfine interactions are usually resolvable in CVD (Chemical Vapor Deposition) diamonds through ODMR (Optically Detected Magnetic Resonance). The inhomogeneous broadening is typically too broad in HPHT (High Pressure High Temperature) diamonds to discern hyperfine sublevels. Despite having a much lower concentration of nitrogen impurities than magnetic carbon impurities (^{13}C), nitrogen impurities can be the source of a much greater magnetic noise because of the larger gyromagnetic ratio(1.08 kHz/G for ^{13}C vs 2.8 MHz/G for nitrogen). In some experiments[40], spin-1/2

^{15}N ions are implanted in diamond which result in a simpler hyperfine structure of four spectral lines.

The hyperfine component of the Hamiltonian, $\hat{H}_{hfs}$ can be written as[41]

$$\hat{H}_{hfs} = \frac{1}{\hbar^2}[D_{gs}S_z^2 + A_\parallel S_z I_z + A_\perp(S_x I_x + S_y I_y) + P I_z^2]\,. \tag{1.11}$$

At room temperature, $D_{gs} = 2870$ MHz and increases to $D_{gs} = 2878$ MHz at 77 K, this splitting is because of the spin-spin interaction between the parallel and anti-parallel pair of electrons. I and S are the Pauli spin matrices for the nuclear and electronic spin, respectively. A is the magnetic hyperfine coupling parameter and P is quadrupole coupling parameter. The parallel and perpendicular components are taken with respect to the NV quantization axis (line connecting the nitrogen atom to the vacancy).

The hyperfine coupling splits ground state transitions into triplets, separated by about 2 MHz. This structure is revealed by driving the ground state transitions and is helpful for simultaneous electrometry and magnetometry as shown in the next chapter. The same high-resolution information can be obtained with nonlinear optical spectroscopy, such as coherent population trapping[33] or electromagnetically induced transparency (EIT)[15], discussed in Chapter 4.

The electronic part of the Hamiltonian can be written as

$$\hat{H}_{es} = \frac{1}{\hbar^2}d_\parallel \Pi_z S_z^2 + \frac{\mu_B}{\hbar}\vec{S}.\bar{g}.\vec{B} - \frac{1}{\hbar^2}d_\perp \Pi_y(S_x^2 - S_y^2) - \frac{1}{\hbar^2}d_\perp \Pi_x(S_x S_y + S_y S_x). \tag{1.12}$$

Here d is the electric dipole moment of the ground state. As can be seen in the Hamiltonian, the parallel component of d, $d_\parallel$ produces an effective shift in D_{gs} while the perpendicular component, $d_\perp$ produces an equal and opposite shift in the $m_s = \pm 1$ sublevels causing them to repel near an avoided crossing. Since the Stark shift is only appreciable near avoided crossings, sensitive electrometry using the ground state can only be performed at certain axial magnetic fields.

Even in the absence of an externally applied electric field, we observe that the resonance lines appear to be Stark shifted. This is because the inherent strain in the diamond which manifests as an apparent electric field[27]. To accommodate the strain induced Stark shift in the Hamiltonian, $\vec{\Pi} = \vec{E} + \vec{\sigma}$ represents the sum of the strain field, $\vec{\sigma}$ and the electric field, $\vec{E}$.

The Zeeman interaction is encapsulated in the $\vec{S}.\bar{g}.\vec{B}$ term where $\bar{g}$ is effective g-factor tensor which has longitudinal component $\bar{g}_\parallel$ and transverse component, $\bar{g}_\perp$. A very small anisotropy for the two components of the g-factor has been observed[42]. $\vec{B}$ is the magnetic field vector.

To compare our experimental results with theory, the complete Hamiltonian was simulated in MATLAB[43](see Appendix). The values and sources for the parameters used in the simulation that resulted in the best agreement with

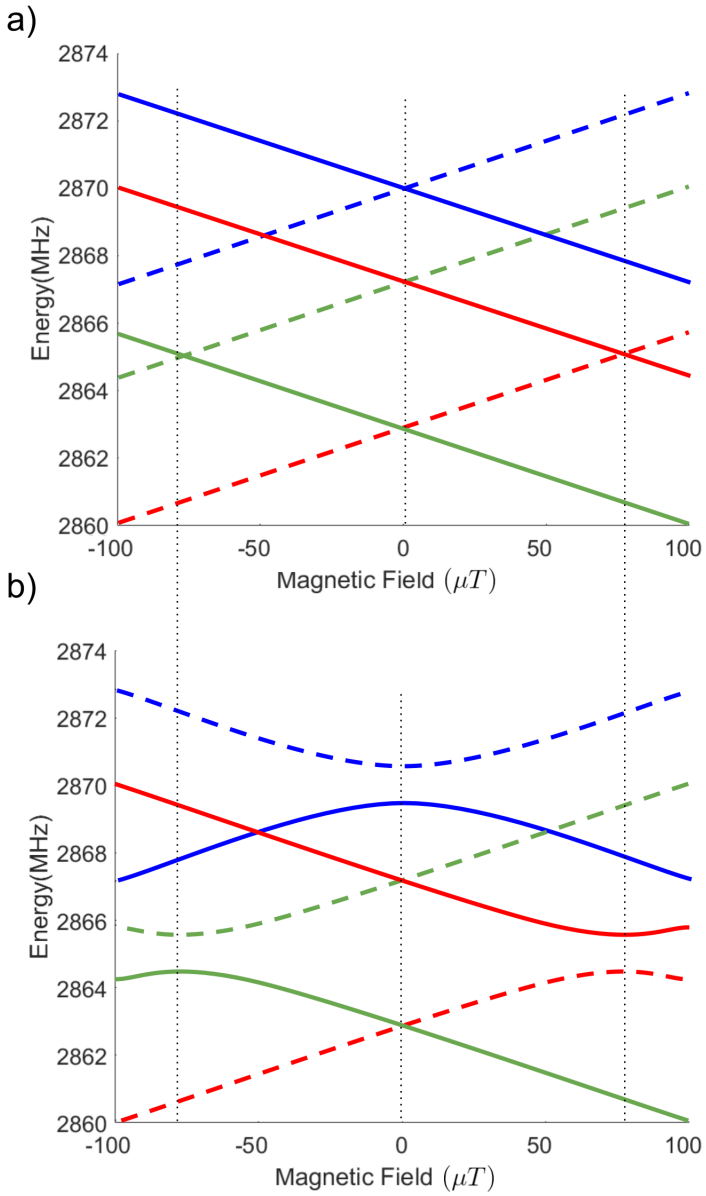


Figure 1.10: Simulated magnetic field induced Zeeman shifts of the ground state energy levels, $m_s = +1$ (solid) and $m_s = -1$ (dashed) for a) no strain b) with a strain equivalent to 15 kV/cm. Strain induced avoided crossing between the $|m_s = \pm 1, m_I = 0\rangle$ sublevels (blue) occurs at 0 μT, between the $|m_s = \pm 1, m_I = +1\rangle$ sublevels (red) at 77 μT and $|m_s = \pm 1, m_I = -1\rangle$ sublevels (green) at -77 μT.

experimental data are listed in table 1.1.

Table 1.1: Parameters used to model the ground state Hamiltonian of the NV center

Parameter	**Value**	**Source**
D_{gs} (300K)	2871.2 MHz	Experiment
D_{gs}(4K)	2878 MHz	Experiment
$g_\perp$	2.0028	[44]
$g_\parallel$	2.0023	[44]
$A_\perp/h$	2.7 MHz	[45]
$A_\parallel/h$	2.166 MHz	[46]
P/h	4.945 MHz	[47]
$d_\perp$	17 Hz cm/V	[48]
$d_\parallel$	0.35 Hz cm/V	[48]

The solution to the electronic part of the Hamilton reveals three eigenstates, corresponding to the magnetic levels, $m_s = 0$ and $m_s = \pm 1$. Spin-spin interaction lifts the $m_s = \pm 1$ states above the $m_s = 0$ level by the zero-field splitting (ZFS), $D_{gs} \approx 2.8$ GHz. Upon including the hyperfine interaction with the adjacent spin-1 nitrogen nucleus, the electronic levels split into a total of nine sublevels.

Under an axial magnetic field(along the NV quantization axis, $\hat{z}$), the $m_s = \pm 1$ energy levels are Zeeman shifted. The simulated tuning of these sublevels along with the hyperfine components is plotted Fig. 1.10. For a zero axial magnetic field, the two $m_s = \pm 1$ sublevels are degenerate but the hyperfine splitting results in three distinct energy levels corresponding to the nuclear spins, $m_I = 0$ and $m_I = \pm 1$. In the absence of strain or an electric field, the levels tune linearly with an applied magnetic field over the entire range.

But most diamonds come with varying levels of strain, ranging from low strain in ultrapure CVD diamonds to very high strain in HPHT and nanodiamonds [49]. At low magnetic fields (< 50 μT), the strain mixes the magnetic sublevels with $m_I = 0$ nuclear spin projection, creating an avoided crossing. The Zeeman tuning of an NV center's ground state with a strain of 15 kV/cm, typical for a CVD diamond is also shown in Fig. 1.10.

The mixed states at zero magnetic field can be written in terms of the eigenstates of the spin-triplet, $S_z(|0\rangle$ and $|\pm 1\rangle)$ (ignoring the hyperfine interaction) [27]

$$|S_\pm\rangle = \frac{1}{\sqrt{2}}(e^{-i\phi\sigma/2}\,|1\rangle \pm e^{i\phi\sigma/2}\,|-1\rangle), \tag{1.13}$$

σ is the magnitude of the strain and ϕ is the phase between the two states. The expectation value of the spin operator for both these states is zero

$$\langle S_\pm|\,\vec{S}\,|S_\pm\rangle = 0. \tag{1.14}$$

Hence these states do not tune linearly with an applied magnetic field but instead are more sensitive to the strain or electric field. This has important implications for the free evolution of such states: they become immune to the magnetic field induced decoherence effects, while at the same time becoming more susceptible to strain inhomogeneities or fluctuating electric fields created by the charge conversion of nearby defects[50].

Photo-ionization of neighboring defects is also thought to explain the sudden changes in the wavelength of the ^{3}A-^{3}E optical transition, a phenomenon known as spectral diffusion[51]. Recent work has shown that applied electric fields can be used to stabilize the absorption/emission wavelength of single NV centers[52]. Stability helps in coupling multiple NV centers as qubits.

Another pair of features worth noting in Fig. 1.10 are the avoided crossings occuring at a non-zero axial magnetic field of $B = \pm 77$ μT, where the levels with nuclear spin projection $m_I = \pm 1$ would be degenerate in the absence of strain. Since the strain is non-zero, these levels also undergo avoided crossings and become sensitive to electric fields. The electric field measurements in this work are performed at these non-zero magnetic fields since this allows us to easily resolve all six hyperfine transitions and get a better measure of the axial magnetic field, which also influences the magnitude of the Stark shift.

The excited state of the NV center is an orbital doublet. It has a similar g-factor to the ground state and is more sensitive to electric fields on account of a permanent electric dipole moment[27]. The magnetic transitions in the excited state can also be driven with microwaves[53]. We do not use these states for electrometry because of the much shorter lived lifetimes ($T_1 \approx 10$ ns) and the consequent broad resonance lines.

The excited states do help us establish Λ systems which allow for spin non-conserving transitions. This is a prerequisite for electromagnetically induced transparency (EIT) which we use to probe the ground state with a resonant red laser. This work is discussed in chapter 4.

1.2.2 Fabrication

Diamonds for the NV centers were purchased from different vendors with different stated purities of nitrogen and other impurities like boron. Diamonds grown with two different techniques - chemical vapor deposition (CVD) and high pressure high temperature (HPHT) have been investigated. CVD diamonds are slowly grown on a substrate from a specific gas mixture while the growth of HPHT diamonds is done in small volumes of extreme pressure and temperature - akin to the process of natural diamond growth.

All diamonds are roughly the same size - 4.5x4.5x0.4 mm, except for one smaller, high purity electronic grade diamond (E6-EG-SM-1) which 2x2x0.4 mm in size. This diamond has a very low NV concentration and was purchased for single NV experiments.

Table 1.2: Diamonds used in the diamond project for nEDM. The production steps are described in the text.

Name	Electron Fluence	Neutral Vacancies $[V^0]$ ppb	Anneal Temp (C°)	Post-anneal Vacancies $[V^0]$ ppb	$[V^-]$ ppb	[NV-] ppb
E6-CVD-1	10^{16}	-	1000	<1	<1	7.7
E6-CVD-3	10^{16}	29	925	<1	2	6
E6-CVD-5	10^{17}	719	925	<1	<1	10
E6-CVD-4	10^{16}	38	875	<1	<1	19
ME-OG-1	10^{17}	736	875	<1	<1	180
WD-CVD-1	$5x10^{17}$	3550	875	<1	<1	84
WD-CVD-2	10^{18}	6430	875	<1	<1	65.5
WD-CVD-3a	10^{18}	6430	750	290	100	80
WD-CVD-3b	10^{18}	6430	-	-	-	< 1
E6-HPHT-1	$5x10^{18}$	-	875	<1	<1	$21x10^3$
E6-HPHT-2	10^{19}	-	875	<1	<1	$20x10^3$
ME-HN-1	$5x10^{18}$	7000	875	<1	<1	<1
ME-OG-2	$5x10^{17}$	3480	925	32	<1	21
ME-HN-2	10^{19}	9600	875	17.5	<1	<1

The diamonds were purchased from three different vendors - Element 6 (E6), Microwave Enterprises (ME) and Washington Diamonds (WD). The names of the vendors are encoded in the diamond names, as shown in Table 1.2. All diamonds used in this experiment were single crystals. The diamonds from Element-6 were listed with varying levels of nitrogen impurities. The HPHT diamonds were estimated to carry less than 200 ppm of nitrogen dopants while the CVD grown optical and high purity electronic grade had tolerances of $[N] < 150$ ppb and $[N] < 5$ ppb respectively. The diamonds with a high nitrogen content carried a brown tint while the other diamonds were mostly clear. All CVD diamonds were type IIa which means that nitrogen is the majority impurity donor. Type IIb diamonds have boron as the typical impurity donor [54].

FTIR To estimate the radiation dose required for optimal NV generation, it was first useful to measure the nitrogen content of the diamonds. For this purpose we used the Nicolet Nexus 670 FTIR (Fourier-transform infrared spectroscopy) instrument[55] to see the infrared absorption spectrum of the diamond samples. Unfortunately the nitrogen content of most of our samples was too low to show up on the FTIR spectrum. We were only able to calculate the nitrogen content of the two nitrogen-rich HPHT diamonds.

The nitrogen concentration in the two HPHT diamonds was calculated using the nitrogen defect associated broad absorption feature at 1130 cm^{-1} in the FTIR spectrum. The calibration constant used was 22 ppm of nitrogen nuclei for every cm^{-1} of absorption[26]. The linear background seen in the spectrum was subtracted to calculate the peak strengths. This led to our nitrogen concentration estimates of 126 ppm and 130 ppm, for E6-HPHT-1 and E6-HPHT-2,

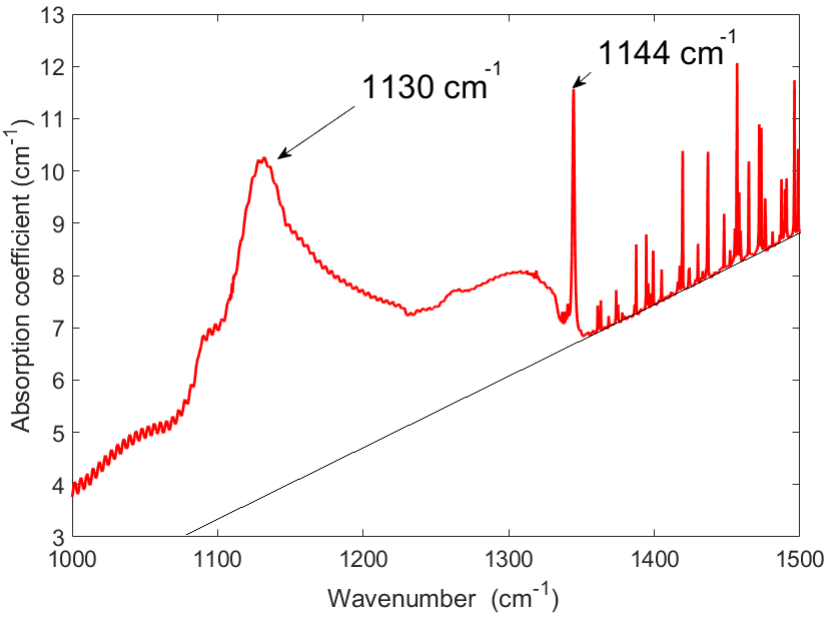


Figure 1.11: FTIR spectrum of E6-HPHT-1 diamond. Both marked spectral lines are associated with the nitrogen defect.

respectively. These estimates were well within the bounds specified by the vendor, $[N] < 200$ ppm. The sharp feature at 1144 cm^{-1} is also assigned to the nitrogen impurity [56]. The FTIR spectra of the CVD diamonds is analyzed and an upper limit of 0.3 cm^{-1} is placed on a possible absorbance feature at 1130 cm^{-1}. This sets a limit on their nitrogen concentrations: $[N] < 5$ ppm. For these diamonds we used the manufacturer's specifications which ranged from $<$ 5 ppb to $<$ 1 ppm.

As we will see in later chapters, nitrogen impurities and spin-1/2 ^{13}C nuclei are the two main sources of spin dephasing in the NV spin-bath. The thermal noise associated with these impurities can be extracted via dynamic decoupling sequences like the Hahn spin-echo. But to achieve a long free evolution time (T_2^*) which sets the limit on our DC sensitivity, it is important to minimize these impurities.

Irradiation In order to form NV centers, the nitrogen atoms need adjacent vacancies in the diamond lattice to couple with. We use electron irradiation at different doses to create these vacancies. The diamonds were sent to an irradiation facility[57] for this process. As shown in Table 1.2, the diamonds received a varying fluence of 2-MeV electrons roughly commensurate with their nitrogen content. After irradiation, the diamonds were spectroscopically examined for the vacancies generated.

The vacancy comes in two different types - the electrically neutral, and the negatively charged[58]. We can distinguish these vacancies in the visible

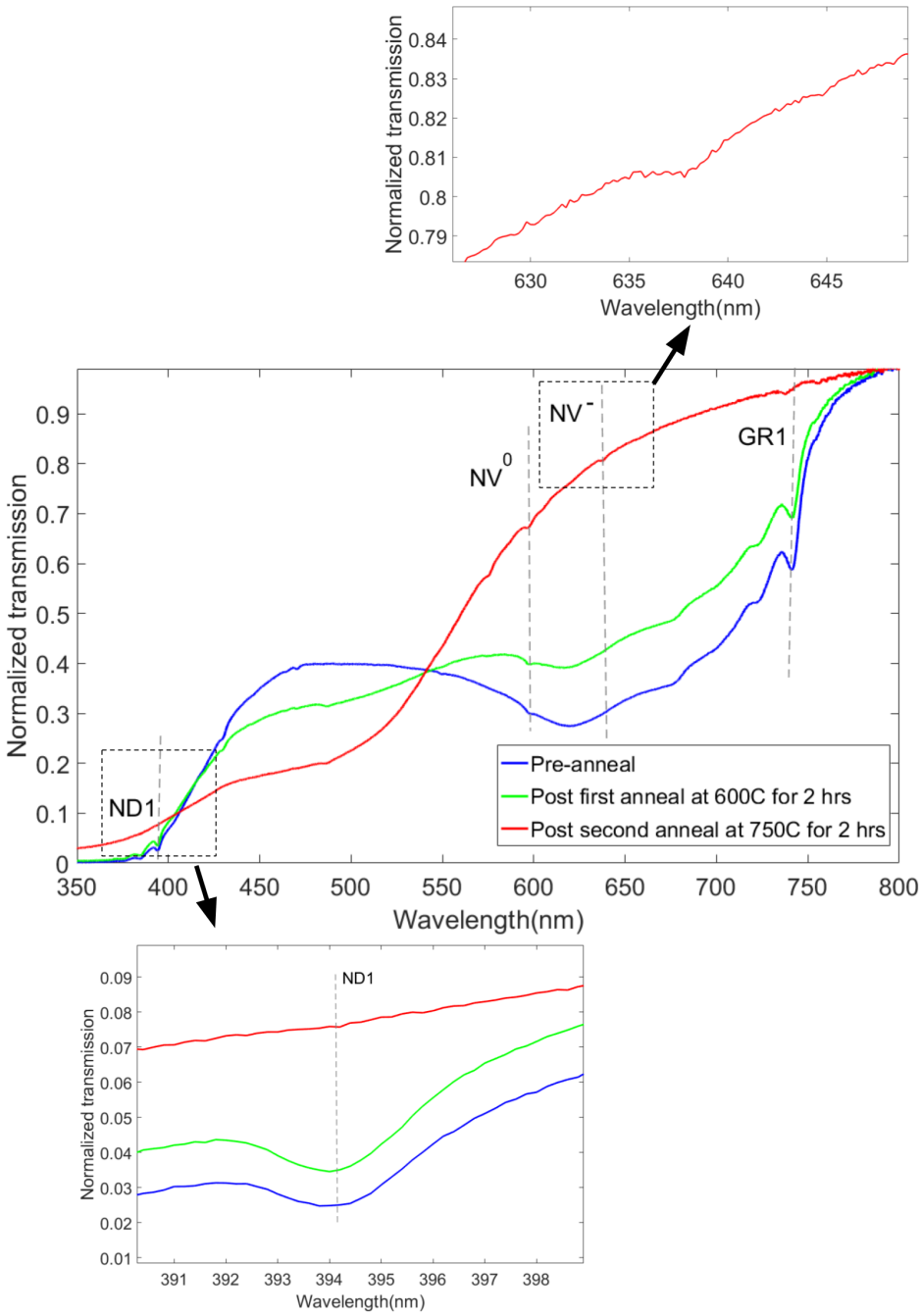


Figure 1.12: The visible absorption graph of diamond WD-CVD-3a before annealing (blue), after annealing at 600 C (green) and finally after annealing at 750 C (red). Four defect centers are identified here - the ND1, NV^-, NV^0 and the GR1 center, these are associated with the negatively charged vacancy, the negatively and positively NV center and the neutral vacancy respectively. A decrease (increase) in the vacancy (NV center) absorption lines is observed after each annealing step.

absorption spectrum. These are labelled as GR1 (neutral) and ND1 (negatively charged). Integrating these absorption lines and using the parameters listed in [58], we can estimate their concentrations.

The calculated vacancy yields are listed in Table 1.2. The absorption feature of the negatively charged vacancy at 396 nm was not visible for all diamonds, because of high background absorption from other features. No vacancy features were observed in the optically dense HPHT samples.

Under ion irradiation, the NVs are usually generated in a very narrow region of the diamond [59]. This can be useful for near field sensing applications. But high energy electrons are expected to traverse 1 mm of diamond without serious attenuation[60]. Thus we can expect an even distribution of vacancies and subsequent NV centers in our samples.

Annealing It is believed that vacancies become mobile when diamond is heated[61]. This encourages coupling to the nitrogen atoms and the subsequent formation of NV centers.

Annealing of diamonds was either performed in vacuum or in the presence of an inert gas like argon. Annealing in air led to the graphtization of the diamond surface which was removed with some difficulty using a refluxing mixture (1:1:1) of nitric acid, perchloric acid and sulfuric acid.

Fig. 1.12 shows the absorption lines associated with the vacancies before and after annealing. The diamond was first annealed at 600 C°. After remaining vacancies were found, the diamond was annealed again at 750 C°. The absorption spectrum, recorded before each annealing shows a reduction in the absorption lines associated with the vacancies. After the final annealing step, zero phonon lines attributed to the NV^- and NV^0 center can be observed.

Yield estimation We were able to produce NV centers in samples with different defect densities, ranging from a few ppb in the CVD diamonds to over 20 ppm in the HPHT diamonds. For quick comparisons, we can observe the differences in spectrally filtered fluorescence between the different diamonds. To get an absolute measure of the NV concentration, we calculate the area under the absorption feature at the 637 nm ZPL and use the parameters in [58]. The concentration of NV^0 can be estimated with a similar method. However, it should be noted that the relative concentration NV^0 and NV^- changes under illumination with different laser wavelengths, power and also electric fields.

As we will see later, the differences in NV and nitrogen densities lead to differences in detection sensitivities. Since the behavior of a spin is influenced by its magnetic environment, we also observe differences in the driven and free evolution dynamics as a function of the defect concentrations.

Chapter 2

Optically Detected Magnetic Resonance

2.1 Theory

The NV center's ground state responds to both electric and magnetic fields. Ensembles of NV centers, as well as single NV centers, have been demonstrated as magnetic sensors. The first paper to discuss electrometry using NV centers derived the ground state electric dipole moment using an oscillating electric field and the spin echo technique. The electric field applied over part of the pulse sequence allowed a sensitive measurement of the electric field induced phase shift[48]. Subsequently, low DC electric fields were shown to induce a Stark shift in single NV centers[27]. We discussed our electric field measurements using ensembles of NV centers at an SPIE conference[62]. Since then, other work has also shown electrometry using NV center ensembles[63].

In this chapter I discuss how we have used ensembles of NV centers in CVD diamonds to measure electric fields and also characterize the magnitude and direction of the internal strain field. The even distribution of NV centers in our samples has also helped us image the distribution of electric fields across the entire volume of the diamond.

The NV center can absorb off-resonant, 532 nm radiation and decay by fluorescing in the red or via a side channel called intersystem-crossing (ISC). This non-radiative pathway is stronger for the $m_s=\pm1$ excited state sublevels. Because of this non-radiative pathway, the overall fluorescence from the excited state varies with the excited state sublevel occupancy. The optical transitions from the ground state are mostly spin preserving, thus the emission in turn depends on the spin orientation of the ground state.

The selective relaxation into the ground state therefore allows the ground state spin projection to be measured by monitoring the brightness of the emitted fluorescence; this measurement scheme also simultaneously polarizes the ground state into the $m_s = 0$ sublevel. The population created with this method is non-Boltzmann and has a sub-Kelvin spin temperature.

Either CW or pulsed microwave techniques can be used to drive magnetic dipole transitions from the $m_s = 0$ to $m_s = \pm1$ levels in the ground state with high spectral resolution[64]. This technique of resolving the ground state electronic structure is called optically detected magnetic resonance (ODMR). The

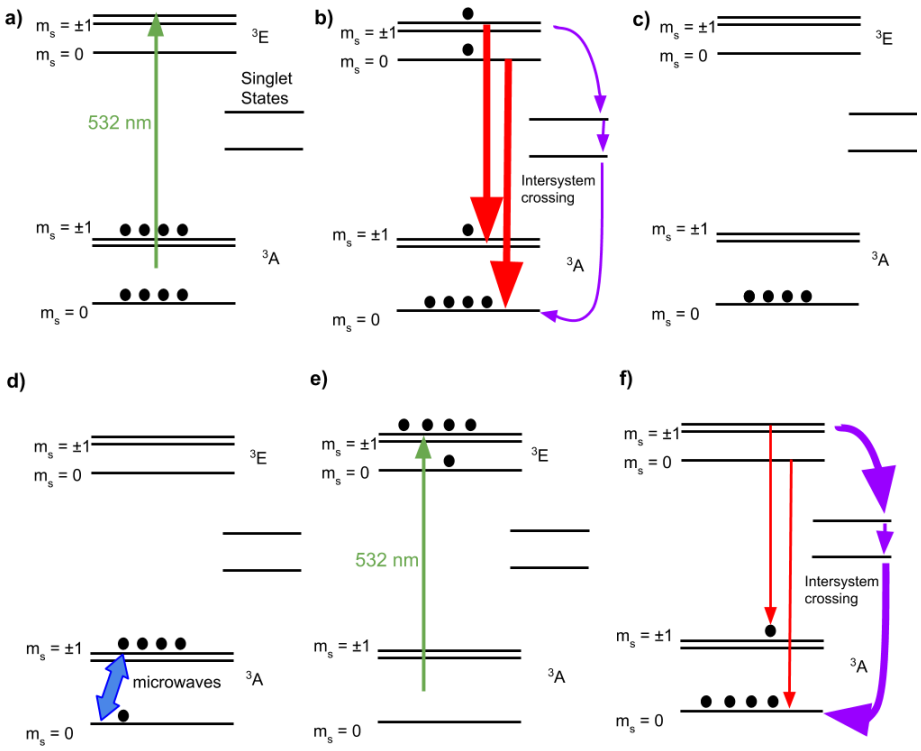


Figure 2.1: The mechanism for optically detected magnetic resonance (ODMR). a) The ground state sublevels are equally populated (unless the temperature is < 1 K or exceptionally high magnetic fields are being used (B> 1 T); neither condition applies for the work discussed here. A green laser pulse drives transitions to the excited state via spin preserving optical optical transitions. b) The excited state, $m_s = \pm 1$ sublevels decay preferentially via the ISC into the ground state $m_s = 0$ sublevel. The excited state $m_s = 0$ sublevel only decays radiatively. c) The ground state is now polarized in the $m_s = 0$ sublevel. d) Resonant microwaves are applied to the ground state, driving electrons from the $m_s = 0$ to the $m_s = \pm 1$ sublevels. e) Green laser again drives optical transitions to the excited state. Since these transitions are spin conserving, the excited state sublevels $m_s = \pm 1$ are more heavily populated. e) The excited state decays to the ground state but now there are fewer electrons occupying the $m_s = 0$ state. The visible fluorescence is attenuated because more electrons decay through the non-radiative pathway.

process is illustrated in Fig. 2.1. In this chapter we show that the ground state resonances resolved through ODMR can be used to detect electric field induced Stark shifts. It also serves as a useful secondary temperature gauge along with a silicon diode, when performing experiments at cryogenic temperatures.

The selection rules for the magnetic dipole transitions are

$$\Delta m_s = \pm 1 \text{ and } \Delta m_I = 0. \tag{2.1}$$

This leads to six possible transitions within the ground state of the NV center. We can drive these transitions using a microwave source while simultaneously illuminating the diamond with a green laser which serves as a pump beam as well as a readout. As the frequency of the source matches the energy splitting in an allowed transition, we observe a dip in the emitted fluorescence spectrum. This reduction in fluorescence upon resonant microwave excitation is because the population of electrons driven from the ground state $m_s = 0$ state to the $m_s = \pm 1$ state is now more likely to decay via the non-radiative intersystem crossing. The magnitude of this observed change in contrast in the emitted fluorescence is a few percent.

A typical ODMR spectrum is shown in Fig. 2.2. The linewidth of an ODMR resonance line in CVD diamonds is around 500 kHz. This increases for diamonds with a higher NV concentration and also scales with other impurities. In HPHT diamonds the linewidths are typically around 5 MHz, making it hard the distinguish the hyperfine sublevels.

The resonance lines are centered at 2870 MHz which is the room temperature zero-field splitting (ZFS), denoted as D_{gs} in the ground state Hamiltonian(see Equation 1.11). The ZFS depends on temperature, changing by about 10 MHz over temperatures between 4 K and 300 K [28]. However, the ZFS is not of great importance to us since we always use the difference between the $m_s = \pm 1$ resonance frequencies to extract magnetic and electric field data, for which the ZFS cancels out.

2.2 Experimental Details

A confocal microscope was built to probe the ground state resonances within a small NV ensemble. The setup is shown schematically in in Fig. 2.3. Light from a 30-mW frequency-doubled Nd:YAG laser[66] was adjusted in power with a continuously variable neutral density filter. The angle of the linear polarization was adjusted with a half-wave plate, allowing selective excitation of NV centers within the ensemble.

The light beam was brought onto the optical axis of the confocal microscope by means of a dichroic mirror[67]. The light was focused on the diamond using a glass-thickness compensated, 50x microscope objective (Mitutoyo 50x, 0.55 NA, long-working-distance(LWD))[68] located outside the cryostat. The relatively

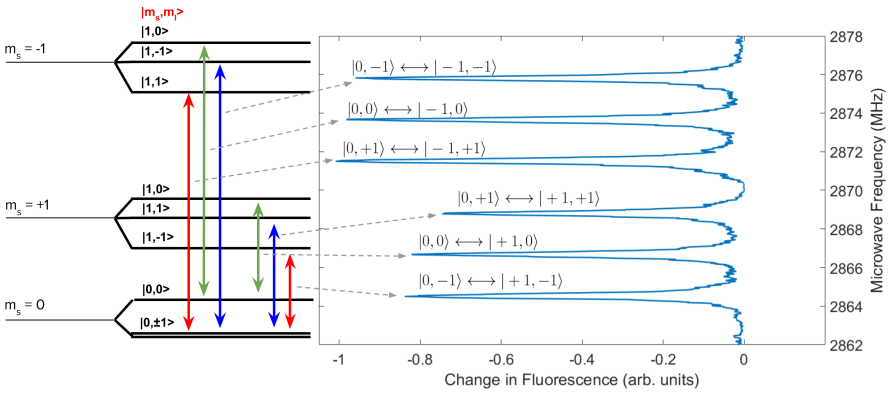


Figure 2.2: Magnetic transitions observed in the ground state of the NV center, as per the selection rules (2.1). As the microwave frequency is swept across the $m_s = \pm 1 \leftrightarrow m_s = 0$ transitions, six dips in the fluorescence are observed on resonant excitation. The width of these transitions is about 0.5 MHz and is typically larger for samples with higher NV concentrations.

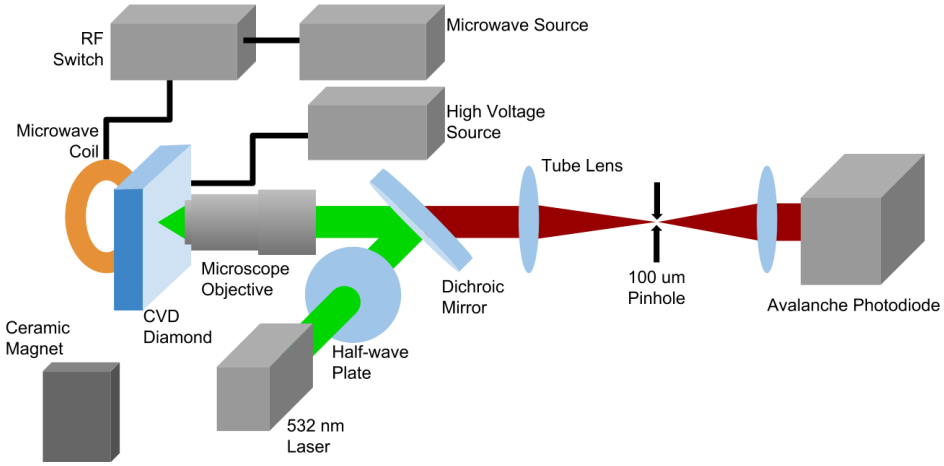


Figure 2.3: Experimental setup for ODMR experiments. The confocal microscope allows a small volume to investigated to minimize the magnetic and electric inhomogeneities in the investigated region. This figure has been adapted from [65].

long working distance of this objective (13 mm) accommodated the cryostat window (3.175 mm thick synthetic fused silica, AR coated) and the stand-off from the window to the diamond.

The emitted fluorescence from the NV ensembles was collimated by the microscope objective and filtered through an optical long-pass filter (Andover 590 FG05)[69] which provided additional spectral selectivity after the dichroic mirror. The infinity-corrected objective allowed a long beam path in which additional colored filters like the notch filter (centered around the excitation laser line, 532 nm) could be introduced. This helped to maximize ODMR contrast at different operating temperatures.

The pinhole served as a spatial filter and gave us the resolution required for electrometry. Without a pinhole, the region we sample would be too large and the recorded spectrum would reflect the electric field inhomogeneities across the whole thickness of the diamond, about 400 μm. The 100-μm sized pinhole restricted the confocal volume to a few airy units and reduced the inhomogeneous broadening. The filtered fluorescence was collected by an avalanche photodiode (Thorlabs APD 410A)[70]. For ease of alignment and adjustments, all optical components were mounted in an optical cage system.

The microwave source was a programmable, digitally-synthesized oscillator[71] with a maximum output power of 18 dBm. Additionally, the microwaves were amplified to about 25 dBm[72]. To enable lock-in detection, the microwaves were digitally modulated with a switch[73], typically at a few kHz.

A resonant loop antenna, 3.4 cm in diameter, was used to couple the microwaves to the diamond, placed about 1 cm away. This ensured that the NV centers were in the near field region. The loop's symmetry axis was aligned with the optical axis. Given the [100] geometry of all our diamonds, the rotating magnetic field was degenerate on all four NV axes.

2.2.1 Resolution of confocal microscope

Most of the experiments mentioned in this chapter were carried out in a cryostat which limited us to microscope objectives with a long working distance and a low numerical aperture. The microscope objective that gave us the best resolution was the Mitutoyo Glass Thickness-Compensated Infinity Corrected Objective (working distance = 13.89 mm and NA = 0.5) which is ideal for imaging into vacuum systems through an optical window.

The axial resolution of a confocal microscope is much poorer when compared to its lateral resolution, this disparity is enhanced for microscope objectives with a low numerical aperture like ours. This is because of the ellipsoidal shape of the point spread function.

The axial and lateral resolution of our confocal microscope can be estimated with the following formulae[74]

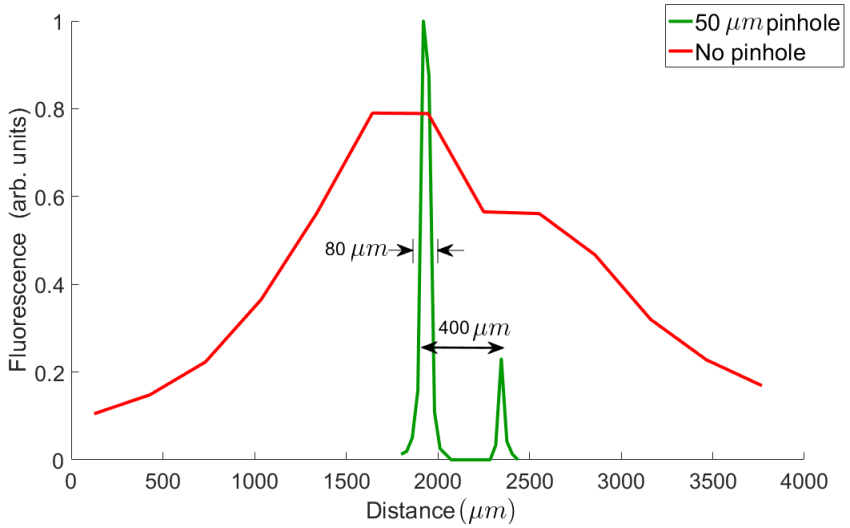


Figure 2.4: Reflection observed from the front and rear face of the diamond. This allows us to estimate the axial resolution of our confocal microscope. The two peaks are separated by the width of the diamond (400 μm). Our axial resolution is estimated to be about 80 microns using this method. The red curve is recorded without a pinhole before the detector.

$$r_{axial} = \sqrt{\left[\frac{0.88\lambda_{ex}}{n - \sqrt{n^2 - NA^2}}\right]^2 + \left[\frac{\sqrt{2}\ n\ PH}{NA}\right]^2} = 128\ \mu m, \tag{2.2}$$

$$r_{lateral} = \frac{0.51\lambda_{ex}}{NA} = 0.5\ \mu m, \tag{2.3}$$

λ is the wavelength of the excitation laser (532 nm), PH is the pinhole diameter (100 um), NA is the numerical aperture of the objective lens (0.5) and n is the index of refraction of vacuum (1). Constricting the diaphragm of the pinhole blocks more of the light coming from above and below the focal plane. This results in better optical sectioning but also leads to a reduction in the signal-to-noise by limiting the number of photons reaching the detector. To experimentally test our axial resolution, we can move the diamond in and out of focal plane. As the focal plane coincides with the front and back face of the diamond, we observe a spike in light that reaches the detector as it is reflected off the diamond surfaces. The spectral filters are removed for this test. Fig. 2.4 shows the magnitude of light as the diamond is moved in the z direction. We use the widths of these features, about 80 microns as estimates for our axial resolution.

The estimated count of NV centers within our probed ensemble can be calculated since we know the concentration of NV centers through spectroscopic techniques. In a diamond carrying a concentration of NV centers that is a few parts per billion, we are investigating an ensemble composed of about ten thousand NV centers.

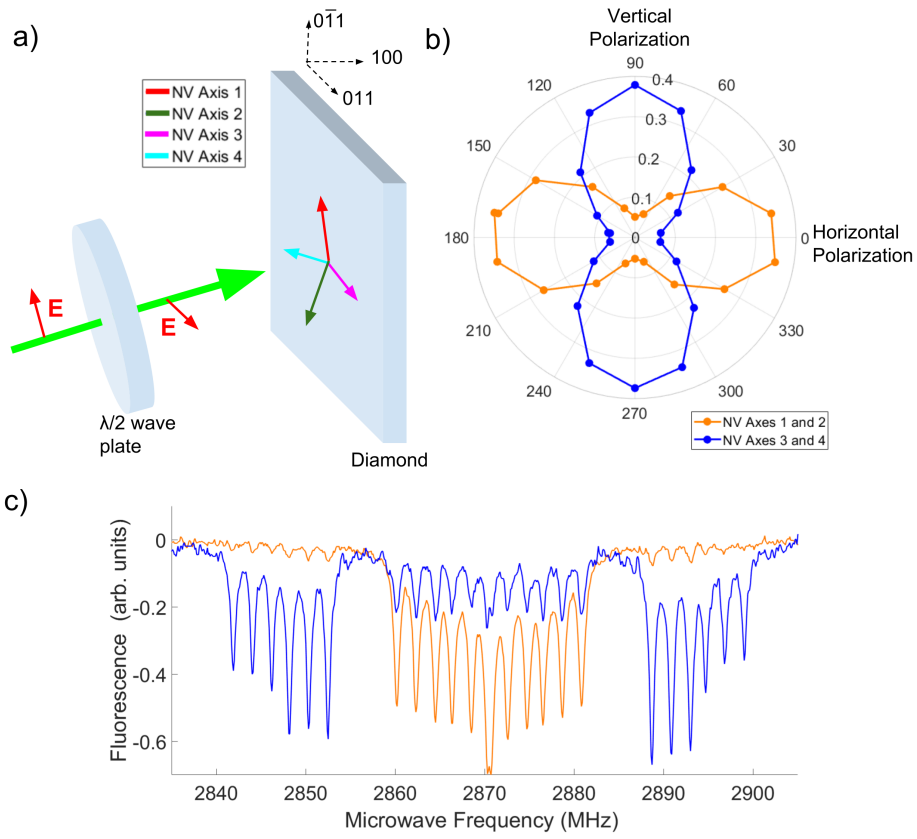


Figure 2.5: a)By rotating the polarization of the green laser, we can select pairs of NV centers from the four found in the ensemble. b) The measured ODMR contrast observed for pairs of NV axes as a function of the green lasers polarization angle. We can turn off the resonances from NV centers 1 and 2 if the polarization of the green laser is horizontal in the lab frame. c) ODMR spectrum for horizontally polarized light (orange) and vertically polarized light (blue). We see two sets of twelve resonances, corresponding to pairs of NV axes.

2.2.2 Polarization-dependent excitation

Since there are four possible crystallographic orientations of NV axes, we see four different sets of resonances within the spectrum for a non-degenerate magnetic field. The magnetic dipole transition rules allow for six ground state transitions. Hence we observe a total of (4x6=) 24 resonances in the ODMR spectrum. It can be challenging to interpret these resonances without a way to assign these resonance lines to NV centers oriented along the different axes. We can introduce some selectivity in our spectrum by modulating the polarization of the exciting green laser[75].

The dipole moment associated with the NV optical transitions, $\vec{d}$, is oriented perpendicular to the NV axis, while the electric field component $\vec{E}$ of the green laser can be rotated with a half-wave plate. The optical transition rate R, has

the following relation[76]

$$R \propto (\vec{d}.\vec{E})^2 \propto cos^2(\theta), \tag{2.4}$$

θ is the angle between the polarization of the laser and $\vec{d}$, the dipole moment associated with optical transitions. Since all our diamonds are grown in the [100] plane, this method allows us to selectively drive transitions of NV centers in pairs by rotating the polarization of the laser.

The ODMR spectrum can serve as a measure for how efficiently we are driving the optical transitions. As the microwave frequency is tuned across the hyperfine transitions, we can monitor the contrast (measured as the height of the resonance features) in these resonances as a function of the green laser's polarization. We find that we can effectively turn off pairs of resonance lines by turning the polarization of the laser parallel to the NV axis(as it is projected in the plane perpendicular to the laser beam). The resonances are not completely turned off because of small misalignment in the diamond with respect to the angle of the half-wave plate. This is illustrated in Fig. 2.5.

In principle the NV centers can be further distinguished between parallel(NV) and anti-parallel(VN) orientations. However, the only term that lifts this degeneracy in the Hamiltonian is the longitudinal Stark shift component, $d_{gs}\Pi_z$ (see equation 1.12). Π_z is the electric or strain field along the axis joining the nitrogen and the vacancy. For the largest electric field magnitudes discussed here, we can expect the NV-VN resonances to split by $d_{gs}^{\parallel} \times 30$ kV/cm = 10 kHz. This is below our typical measurement sensitivity and hence we ignore the difference between NV and VN centers.

2.3 Strain measurements

Since the total electric field measured in these experiments is the sum of the externally applied electric and effective electric field produced by the intrinsic strain, it is important to characterize the strain magnitude and direction.

2.3.1 Lineshape

A Stark shifted ODMR spectrum is shown in Fig. 2.6. Here an axial magnetic field of 77 μT along one of the NV axes, brings the $|m_s = 1, m_I = 1\rangle$ and $|m_s = -1, m_I = 1\rangle$ ground state sublevels near an avoided crossing. A moderate transverse magnetic field of $B_\perp$=200 μT keeps the ODMR resonances from NV's oriented along the other three axes out of our scanning range.

These are the six hyperfine resonances of the ground state. The outer four can be fit to Lorentzians with a width of about 400 kHz. These outer four resonances do not tune appreciably with strain and hence can be used as unbiased measures of magnetic fields.

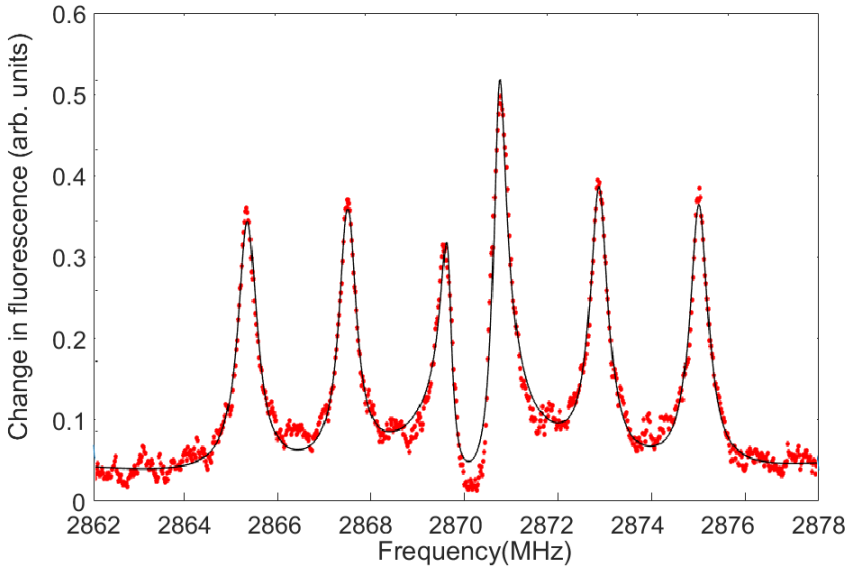


Figure 2.6: Strain-induced Stark shift observed near a magnetic field of about $-77\,\mu T$. The outer four resonance lines have been fit to Lorentzian lineshapes while the inner peaks have been fit to asymmetric Doniach-Sunjic[77] profiles with an asymmetry parameter, $\alpha \approx 0.2$.

The inner resonances repel near the ZFS because of the non-zero strain. The strain in this diamond is equivalent to an electric field of 21 $\pm$ 4 kV/cm. The degenerate microwave field projection onto the NV axis makes the magnitude of the four outer peaks roughly equal. However, since the transitions near D_{gs} are from spin mixed states ($|\pm\rangle = \alpha\,|m_s = 1\rangle \pm \beta\,|m_s = -1\rangle$), there is a trade-off in contrast between these two resonances. The inner Stark-shifted resonances also deviate from a Lorentzian lineshape and become asymmetric. This can be explained in light of the magnetic field induced inhomogeneous broadening. The observed line shape is comprised of contributions from many NV centers in the ensemble. The NV centers that experience a smaller net magnetic field are closer to the ZFS, are more strongly mixed and thus experience a larger Stark-shift. The NV centers that experience a larger net magnetic field are farther away from the avoided crossing and do not tune as much with strain. This inhomogeneity is the result of the difference in proximal impurities for individual NV centers within the ensemble. A Stark shift induced crowding effect away from the avoided crossing results in asymmetric resonance lines. This effect is also seen in simulations where the magnetic field noise is modeled as a random dipolar field.

Fitting these inner peaks to Lorentzians leads to large residuals and uncertainties associated with the fit parameters. Hence we instead fit to the Doniach-Sunjic function which is used to fit X-ray induced fast photoelectron distributions[77]. This function has an asymmetric lineshape

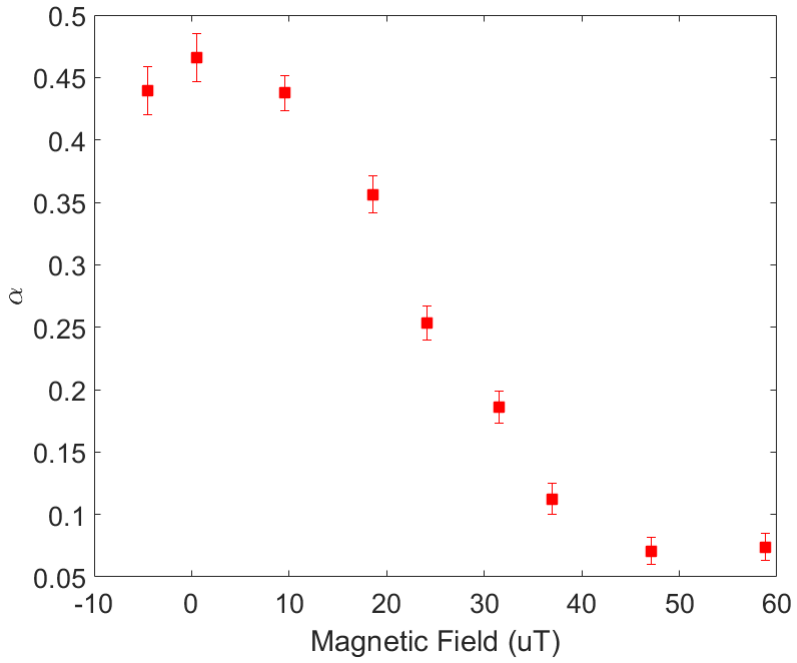


Figure 2.7: The asymmetry parameter, α, as a function of the magnetic field. The lineshape becomes more asymmetric as the resonances approach the avoided crossing and the strain mixes the $m_s = \pm 1$ sublevels.

$$I(\alpha, \nu, \nu_0, \Delta\nu) = \frac{\cos[\pi\alpha/2 + (1-\alpha)\tan^{-1}(\nu - \nu_0)]}{[\Delta\nu^2 + (\nu - \nu_0)^2]^{(1-\alpha)/2}}, \tag{2.5}$$

where ν is the frequency of the microwaves, ν_0 is the center of the lineshape, $\Delta\nu$ is the inhomogeneously broadened linewidth and α is the asymmetry parameter. At $\alpha = 0$, this equation represents a regular Lorentzian. The parameter α increases as the resonances approach the zero-field crossing, reaching a maximum $\alpha \approx 0.5$ in most CVD samples when the $m_s = \pm 1$ states are maximally mixed. The relationship between α and the axial magnetic field is shown in Fig. 2.7.

2.3.2 Strain magnitude

Once we have good fit parameters for our ODMR spectrum, we can use the ground state Hamiltonian to extract values for strain. As shown in Ref. [27], by solving the ground state electronic Hamiltonian in Eq. (1.4), we can calculate the magnetic transition frequencies, $\omega_\pm$, between the states $m_s = 0$ and $m_s = \pm 1$

$$\hbar\omega_\pm = D_{gs} + d_{gs}^{\parallel}\Pi_z \pm [(\mu_B g_e B_z)^2 + (d_{gs}^{\perp}\Pi_\perp)^2 - \frac{(\mu_B g_e B_\perp)^2}{D_{gs}} d_{gs}^{\perp}\Pi_\perp cos(2\theta_B + \theta_\Pi) + \frac{(\mu_B g_e B_\perp)^4}{4D_{gs}^2}]^{1/2}. \tag{2.6}$$

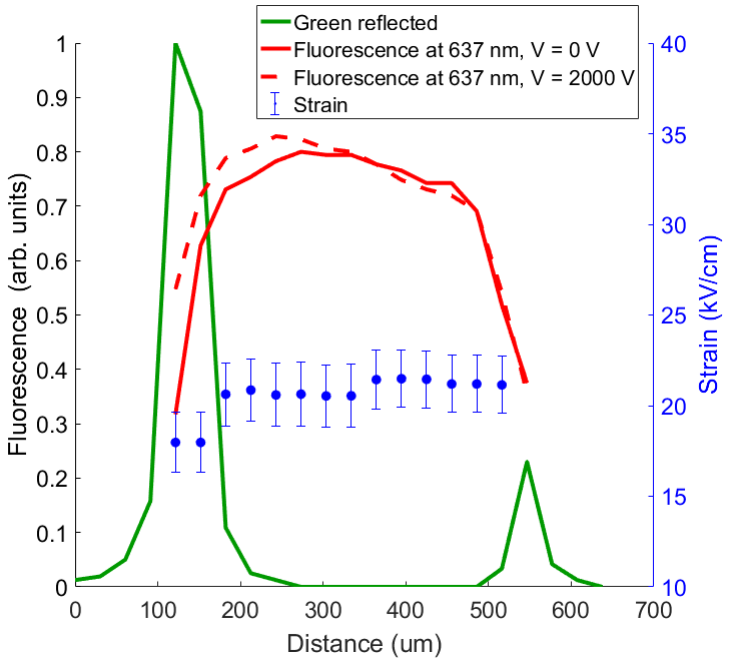


Figure 2.8: The green curve shows the magnitude of the laser light that is reflected from the top and bottom faces of the diamond. The red curves represent the intensity of the 637-nm ZPL. Applying an electric field increases the observed fluorescence at the NV center ZPL. Curves are rescaled for clarity. The blue data points show the strain measured as a function of depth in the diamond. This figure has been adapted from [65].

Here, θ_Π and θ_B are the polar angles for the transverse electric and magnetic fields, respectively. Note that this excludes the hyperfine interaction with the nitrogen nucleus.

We begin our experiments with a value of $B_\perp < 200$ μT. In this case, we can use $\frac{(\mu_B g_e B_\perp)^2}{D_{gs}} << d_{gs}^\perp \Pi_\perp$, this allows us to ignore the last two terms in the square root. We can also ignore the effect of the longitudinal strain since $d_{gs}^\perp >> d_{gs}^\parallel$. This simplifies our expression to

$$\hbar\omega_\pm = D_{gs} \pm [(\mu_B g_e B_z)^2 + (d_{gs}^\perp \Pi_\perp)^2]^{1/2}. \tag{2.7}$$

Now the Stark shift is independent of the polar angle of the perpendicular electric and magnetic fields and in the absence of an externally applied electric field, we only get a measure of the magnitude of the transverse component of the strain field, $\Pi_\perp = \sigma_\perp$.

As shown in Fig. 2.8, the axial variation in the strain magnitude was measured by scanning the confocal microscope in the (100) crystallographic direction. The collected fluorescence from the NV centers was also mapped during these measurements; this served as a rough measure for changes in NV concentration in the sample. No significant change in fluorescence or strain was

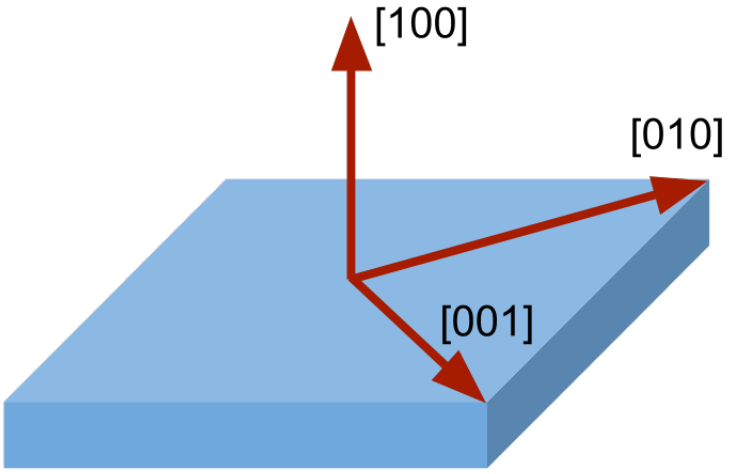


Figure 2.9: Three degenerate [100] directions with respect to the four equivalent [111] NV center axis. The diamond is grown in the [100] direction.

observed. The green fluorescence lets us track the front and back faces of the diamond as it is being scanned. A similar transverse map was also produced by moving the diamond laterally. No significant changes in strain or NV concentration were observed.

The perpendicular strain component, $\sigma_\perp$ of all four NV axes was calculated by applying small orthogonal magnetic fields and sequentially isolating resonances near D_{gs} from the four different [111] crystal directions. It was discovered that all four projections of strain were equal(within uncertainty parameters), $\sigma_\perp^1 = \sigma_\perp^2 = \sigma_\perp^3 = \sigma_\perp^4$. This leaves us with two possibilities for the direction of the strain field:

1. The strain field is isotropic, hence it maps equally onto all four NV axes.
2. The strain field points along one of the three degenerate crystal directions - (100), (010) or (001). These directions are drawn in Fig. 2.9.

To figure out which of the above two cases holds, we need to revert to Eq. (2.7) and use a larger transverse magnetic field. This allows us to use the Stark shift dependence on the polar angle of the transverse magnetic field and determine a strain field direction in the plane transverse to the NV axis.

2.3.3 Strain Direction

A suitably large orthogonal magnetic field (B >1 mT) is generated by a pair of Helmholtz coils and ceramic magnets. The diamond was rotated inside the Helmholtz coils with the NV center axis under investigation aligned perpendicular to the magnetic field.

As the diamond was rotated, changes in the strain-induced Stark shift were recorded. The magnetic field vector was calculated by fitting all twenty four

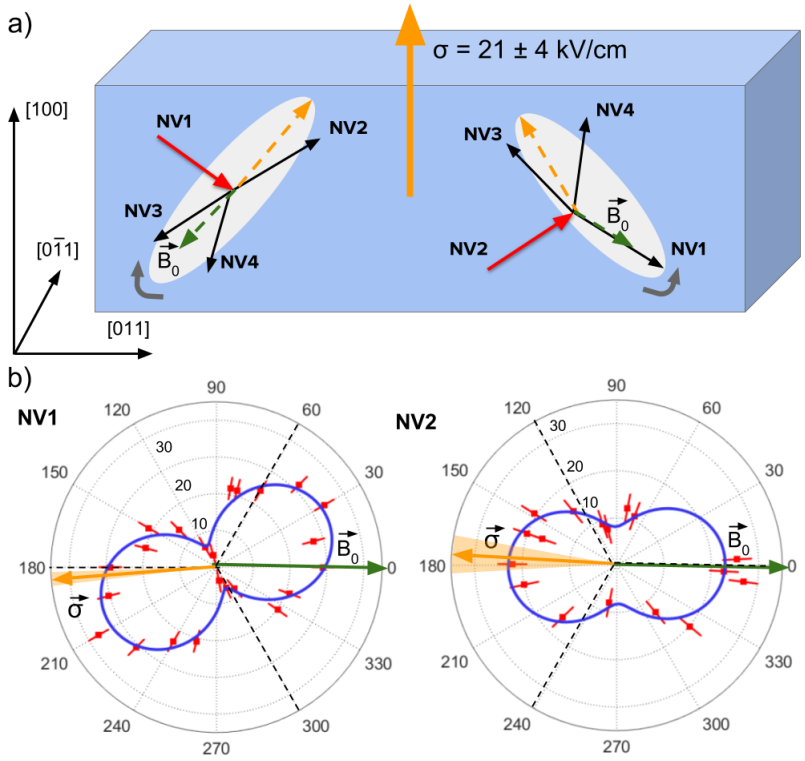


Figure 2.10: a) Schematic illustrating the two NV orientations used to measure the strain direction. The white ellipses represent the plane in which the transverse magnetic field ($B_\perp \approx 1$ mT) is rotated. Strain direction as determined by the polar plots of the Stark shift is drawn in orange. The green arrows represent the initial direction of the magnetic field ($\theta = 0°$ in the graphs below). b) Change in strain-induced Stark shift as a function of the polar angle of the transverse magnetic field for the two NV orientations. Dashed black lines show the lines connecting the vacancy to the three adjacent carbon atoms. Here the strain-induced Stark shifts are measured in kV/cm. The orange vector represents the strain as it projects on the transverse plane and the shaded region represents the uncertainty associated with the strain measurements. Simulated data is shown as a the blue curve. This figure has been adapted from [65].

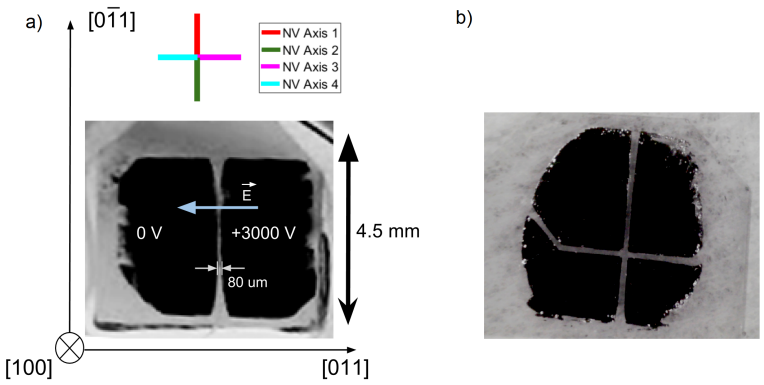


Figure 2.11: Chromium electrodes printed on a CVD diamond. a) In this geometry, the applied electric field is degenerate on pairs of NV axis. b) A second electrode geometry allowed arbitrary electric field direction to be established in the center by applying different voltages on the four pads. Fig.a) has been adapted from [62].

resonances from the four NV axes. A triple axis magneto resistive sensor connected to an Arduino board was also used for rough alignment of the ceramic magnets.

The polar plot from this experiment is shown in Fig. 2.10. Fitting the graph to the energy shifts predicted by the Hamiltonian shows that the strain points in the [100] direction, out of the large face of the diamond. This direction is also parallel to the crystal growth direction. The total strain was determined to be $\sigma = 21 \pm 4$ kV/cm. The degenerate direction of the strain field explains why NV centers aligned along all four crystallographic directions experience the same transverse component of strain.

All diamonds are known to carry some strain and as we have already discussed in the previous chapter, strain induces a mixing of the magnetic sublevels which in turn prohibits linear Zeeman shifts near the avoided crossing. This method allows us to observe a near linear Zeeman shift for small axial magnetic fields despite a large strain component, as long as we are permitted to apply a large transverse magnetic field in the correct direction. As an example, in Fig. 2.10(b), we can see that the strain-induced Stark shift is nulled in NV1 when the transverse magnetic field is oriented at 120° in the non-axial plane. In this configuration of magnetic field and internal strain, our sensitivity to small axial magnetic fields will increase.

2.3.4 Electrometry

In order to apply large electric fields, two chromium electrodes, a few hundred nanometers in thickness, were photolithographically deposited on the top surface of the diamond, E6-CVD-3 (from Table 1.2). A thin layer of titanium was first sputtered on the diamond to promote adhesion to the diamond surface. The

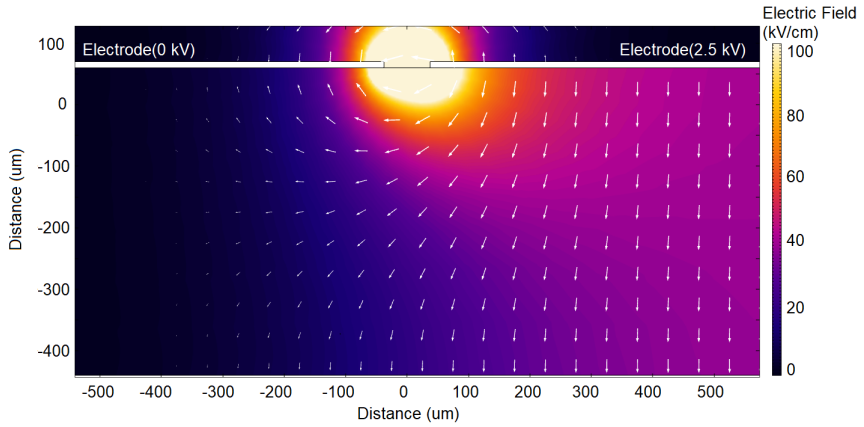


Figure 2.12: COMSOL simulation of electric fields within diamond. The electrodes (white) are separated by the distance of 80 microns. An electric potential of 2500 V is applied on the right electrode. The bottom face of the diamond and the left electrode are grounded. A high region of electric fields is observed near the electrodes and it drops off quickly with depth in the diamond. The white arrows represent the electric field vector.

electrodes were patterned, starting out narrow at a separation of 80 microns in the middle and growing apart to 350 microns near the edges of the diamond. This work was done at Texas A&M University by Dr. Phil Hemmer and his graduate student, Fahad Alghannam. Two different electrode geometries are shown in Fig. 2.11. [1]

The shorting between the electrodes was avoided by careful cleaning the diamond in an ultrasonic bath sequentially with acetone, ethanol and isopronanol. Plasma cleaning was also occasionally performed. Before mounting the diamond in the cryostat, the gap between the electrodes was examined under a microscope for dirt.

If the experiment were to be carried out at ambient pressure, the maximum electric field we could apply would be limited because of electrical breakdown in air. For this purpose, the diamond was mounted in a cryostat which allowed the sample to be held in vacuum at about 10^{-8} Torr. This greatly increased the magnitude of electric field that can be applied between electrodes.

To estimate expected electric field shifts, a simulation of the first pair of electrodes was done in COMSOL[78]. In the simulation(see Fig. 2.12), one of the electrodes is held at 2500 V while the other is grounded. The diamond is typically placed on a copper mount which grounds the rear face of the diamond. The simulation shows a high electric field gradient within the sample; therefore to perform electrometry with some spatial resolution, it becomes necessary to

[1] A second electrode configuration consisting of four chromium pads was also experimented with (Fig 2.11(b)). This configuration let us generate electric fields in the middle by applying different voltages on the four pads. Unfortunately the electrodes were accidently shorted with a large voltage. This led to them being splintered before useful electrometry data could be recorded.

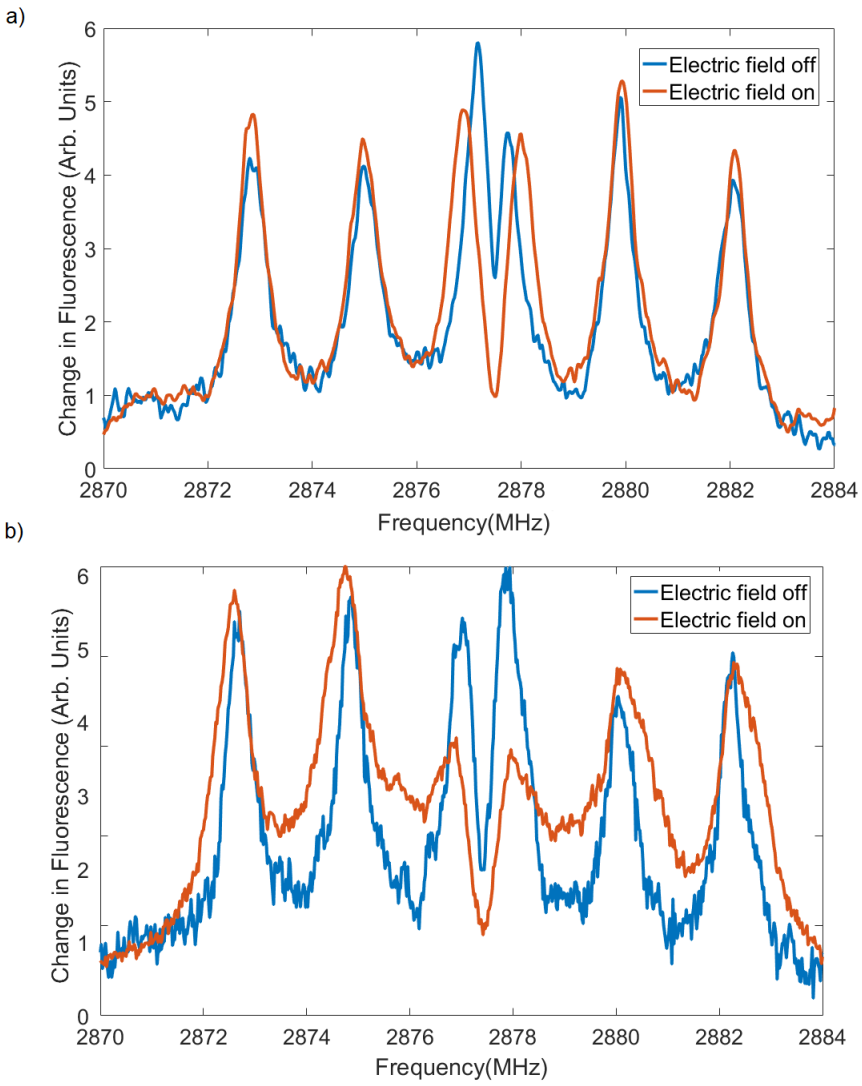


Figure 2.13: Electric field-induced Stark shift observed near a magnetic field of about $-77\,\mu T$. a) This data is recorded with a pinhole; the Stark-shifted resonance lines do not broaden appreciably b) The pinhole is removed for this data. The Stark-shifted lines broaden when the electric field is applied because of the large electric field inhomogeneity in the probed region of the diamond.

spatially filter the collected fluorescence with our confocal microscope.

In the experiment one electrode is grounded at the same potential as the cryostat, and the voltage on the other electrode is varied from 0 to ±3000 V DC with a regulated high voltage supply, connected via a high voltage electrical feedthrough on one side of the cryostat.

The ODMR transitions are shifted by the component of the electric field in the plane perpendicular to the NV axis. An axial Stark shift is also predicted by the Hamiltonian but the small axial component of the ground state's electric dipole moment, $d_{gs}^{\parallel} = 0.35 \pm 0.02$ Hz cm V^{-1} makes it is too small to be measured in our experiment. The Stark shift from orthogonal electric fields is also typically small but the shift is enhanced when the magnetic field is adjusted so that levels of the appropriate symmetry are nearly degenerate. Fig. 2.13 shows levels $|m_s = -1, m_I = -1\rangle$ and $|m_s = +1, m_I - 1\rangle$ near an avoided crossing. When the electric field is applied across the electrodes, it induces a Stark shift of about 200 kHz.

Fig. 2.13 also illustrates the importance of using a pinhole in our experiment. Without a pinhole, the resonances tend to smear out because there is a large electric field- induced inhomogeneity in the interrogated ensemble. A pinhole permits optical sectioning which narrows our probed region and subsequently reduces the electric field gradient within our sampled ensemble.

The ODMR peak positions of one of the four NV centers at a range of electric fields and a constant magnetic field are plotted in Fig. 2.14. The peak positions have been determined with a global fit of six Lorentzians. The data have been fit to the differences in eigenvalues between hyperfine sublevels of the $m_s = \pm 1$ and $m_s = 0$ states by solving the full ground state Hamiltonian. The parameters used in the Hamiltonian are listed in Table 1.1.

As can be seen in the figure, the pairs of lines that experience the largest Stark shift are the ones closest to the D_{gs} and hence maximally mixed. Small detuning of the outer resonances can also be observed.

Stark shifts described for single NV centers in other work[27], are enhanced when the $|m_S = +1, m_I = 0\rangle$ and $|m_S = -1, m_I = 0\rangle$ states are near an avoided crossing, this occurs at an axial magnetic field that is close to zero. From the Hamiltonian given by Doherty[41], we can expect similar enhancements near $B_z = 77$ μT where the $|-1, -1\rangle$ and $|+1, -1\rangle$ levels cross. Likewise, the $|-1, +1\rangle$ and $|+1, +1\rangle$ levels cross at $B_z = -77$ μT. The data are compared to theory in Fig. 2.15 by solving the complete 9x9 ground state Hamiltonian which includes the hyperfine interaction.

Electrometry in this work was usually performed at an axial magnetic field $B_z = \pm 77$ μT because this allowed us to measure the axial magnetic field with the least uncertainty using the outer resonances. At $B = 0$ μT, the outer resonances overlap and only the inner resonances are split because of strain or electric fields.

The sensitivity of the innermost splitting can be found by evaluating the

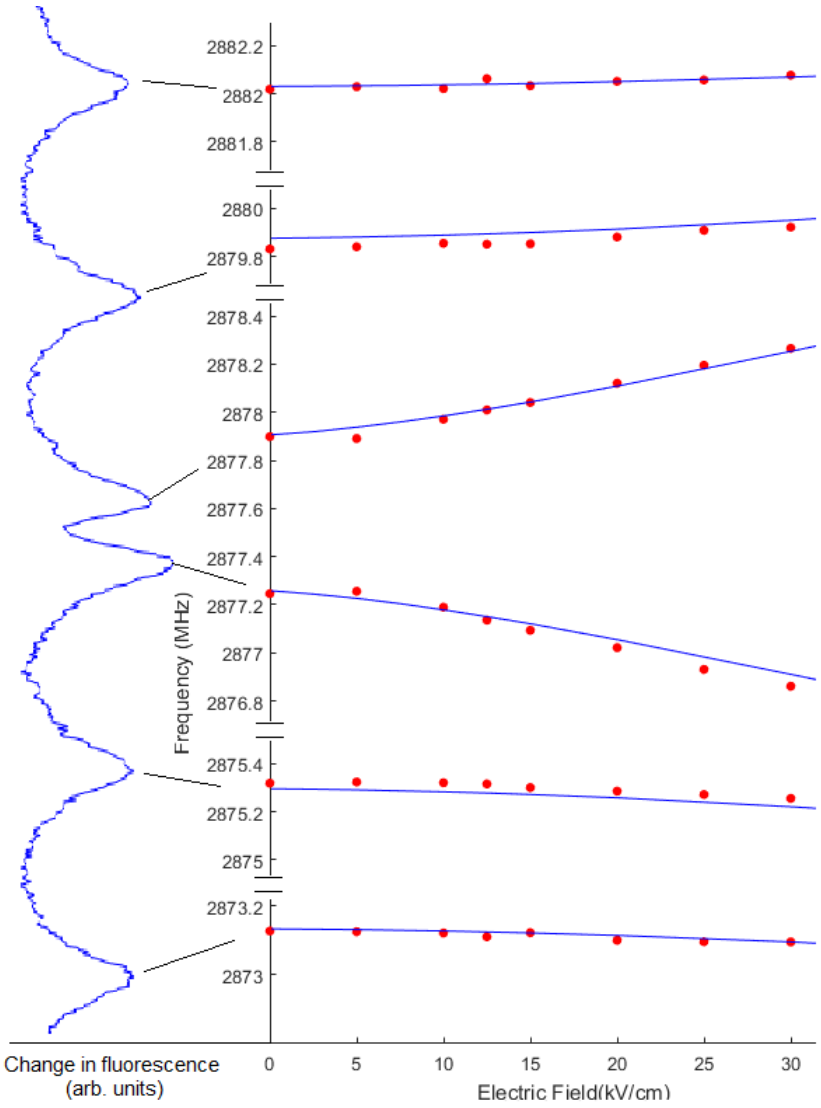


Figure 2.14: Stark shifts for six hyperfine transitions for different electric fields. The blue lines represent the values derived from the ground state Hamiltonian. The inner resonances tune the most as a function of an applied electric field. This figure has been adapted from [62].

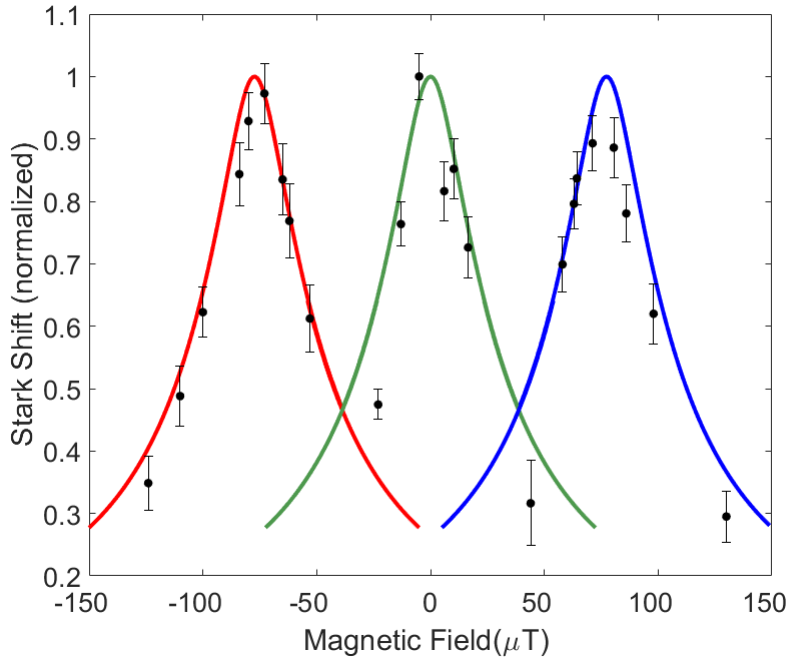


Figure 2.15: Stark shift as a function of axial magnetic field. Solid lines are the three predicted Stark shifts derived from the ground state Hamiltonian. An increase in electric field sensitivity is observed at magnetic fields of B=0 μT and B = $\pm$77 μT. This figure has been adapted from [62].

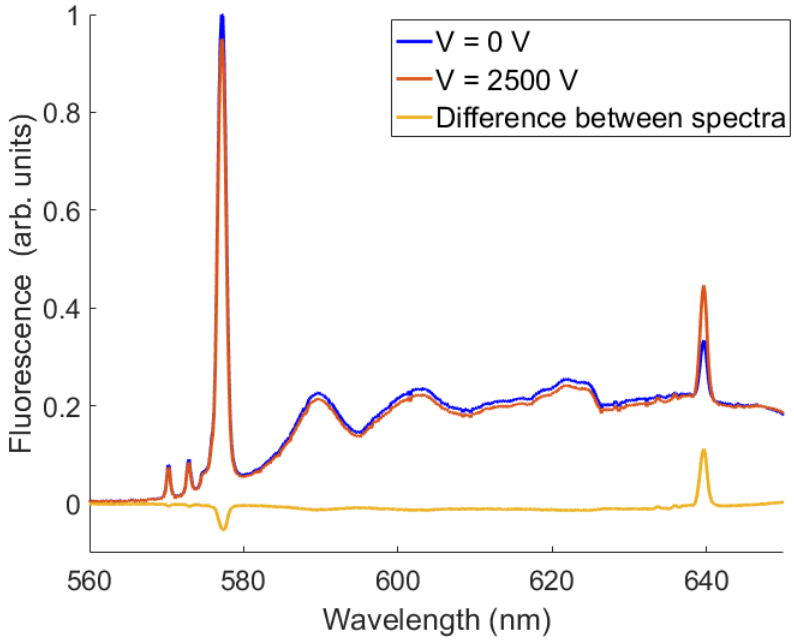


Figure 2.16: Difference in fluorescence at 0 V (blue), 2500 V (red) and their difference (yellow). There is an almost 100% increase in fluorescence from the NV^- ZPL when an electric field is applied. This figure has been adapted from [65].

Hamiltonian at a number of electric fields, or, far from the avoided crossing, by taking the derivative of Eq. 2.7 with respect to the electric field. At each avoided crossing, the splitting has a maximum value of 34 Hz/(V/cm). For an uncertainty in the splitting of about 5 kHz and perfect knowledge of the magnetic field, the corresponding uncertainty in the electric field is 147 V/cm . Far from the crossings, the sensitivity scales as $E^{\perp}/B_z$, with a numeric value of $0.68\,Hz/(V/cm)$ at $E^{\perp} = 30\,kV/cm$ and $B_z = 1\,mT$ (and $B_x = B_y = 0$).

By measuring the fluorescence intensity at the NV^- (637 nm) and NV^0 (575 nm) ZPL, we can measure changes in their relative concentrations(see Fig. 2.16). Closer to the surface, in regions of large electric field (E > 40 kV/cm), there was marked decrease in the concentration of NV^0 centers with a simultaneous increase in NV^- centers (up to 100%). This effect was attenuated as we moved towards the grounded face of the diamond (with lower electric fields). We believe this effect is related to the charge state conversion observed in single NV centers because of field induced band-bending[79]. This effect explains the observed increase in contrast of the ODMR spectra as an electric field is applied.

2.3.5 Electric field imaging

The electrodes were patterned to produce variations in the electric field. A map of the electric field was produced by moving the focal spot across the diamond and measuring the Stark shift for the same voltage difference across the electrodes, as shown in Fig. 2.17 . The resolution of the image produced can be improved by using a tighter pinhole or using a microscope objective with a higher numerical aperture.

Another map of the electric field was produced by moving the focal spot of the microscope objective axially into the diamond and measuring the Stark shift for the same voltage difference across the electrodes, as shown in Fig. 2.18. The results were found to be in good agreement with the simulations performed in COMSOL.

The largest contributor to the systematic uncertainty in this figure comes from the transverse electric dipole moment, d_{gs} = 17 Hz cm/V which has a large associated uncertainty of ±3 Hz cm/V. With just statistical errors, the typical uncertainty in the electric field measurement was $\sigma = \pm 2$ kV/cm. After including systematic uncertainties, the cumulative error was ± 5 kV/cm.

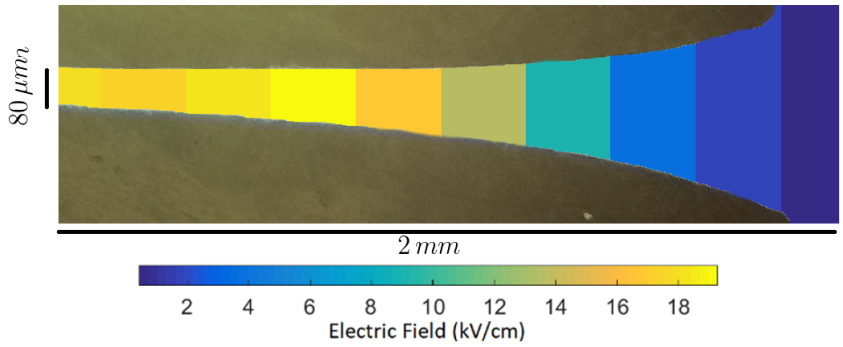


Figure 2.17: Electric field measured between electrodes, about 200 μm inside the diamond. The gap at its minimum is about 80 μm. The electric field magnitude has been color coded. This figure has been adapted from [62].

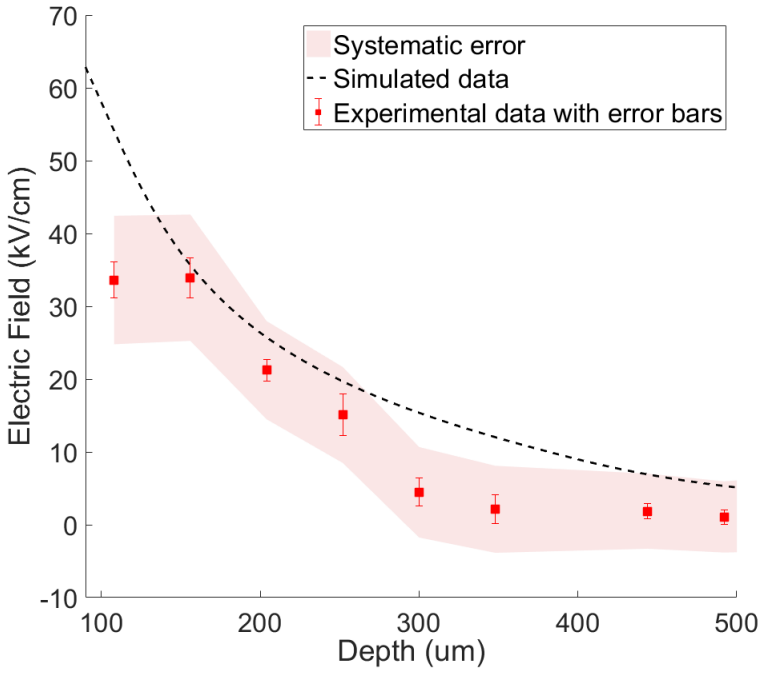


Figure 2.18: Electric field measured as a function of depth the diamond. The simulated data is obtained from finite element analysis done in COMSOL[78]. This figure has been adapted from [65].

Chapter 3

Spin Dynamics

3.1 Introduction

The NV center in diamond has long been considered to be an interesting candidate for quantum information processing (QIP)[80], coherent spintronics, and quantum communication[81]. The long lived spin coherence times, easy state initialization and addressability, photostability and well resolved room temperature transitions make it an attractive candidate for the exploration of quantum phenomenon.

Significant work has been done on the topic of driven and free evolution dynamics of single NV centers in diamond under different surrounding bath configurations and decoupling schemes [82, 83, 84, 85, 86, 87]. However, the progress made on ensembles of NV centers has been limited [88, 89, 90].

Spin dynamics and the resulting decoherence curves can reveal the NV center's bath environment. The decoherence lifetimes calculated from these methods also set the fundamental limits on the achievable AC and DC sensitivities for electric and magnetic field sensing[16].

Metrological applications like magnetometry, electrometry and temperature sensing benefit greatly from using ensembles of spins because the sensitivity, η scales as $\eta \propto \sqrt{N}$ where N is the number of spins. However, in especially dense samples, this gain in sensitivity generally comes with an increase in spin-spin coupling which in turn can lead to a loss in coherence lifetimes. With typical nitrogen($\approx$ 1 ppm) and ^{13}C concentrations($\approx$ 1.1%), the dipolar coupling between NV centers becomes significant above a level of few ppb. Most of our diamonds are near this limit(see table 1.2).

Simulations of NV systems have shown differences in the spin dynamics of single spins versus spin ensembles[91]. We compare our experimental results with this work and other simulations[39, 92, 93] which describe NV spin evolution under different regimes.

To investigate spin dynamics, we use resonant, timed microwave pulses and drive transitions within the ground state manifold of the NV center. This chapter will discuss the different microwave pulse sequences we used to study the evolution and decoherence of prepared spin states.

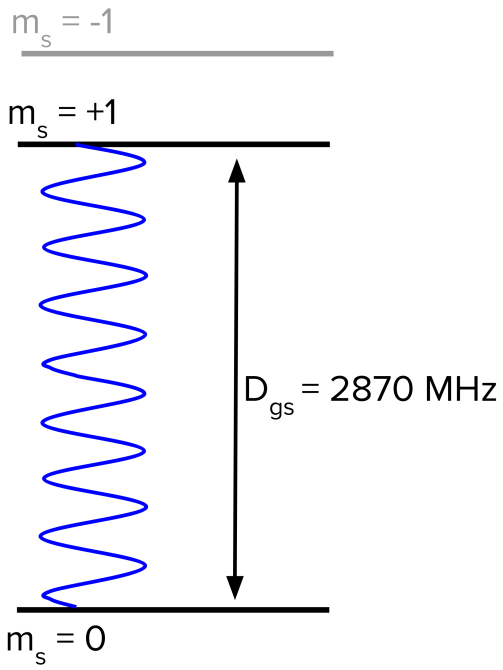


Figure 3.1: Energy level scheme for the two ground states used in the NV center. Coherent microwave radiation is applied to prepare the state in a particular superposition of the two states.

3.1.1 Two-level excitation

For most of this discussion, we ignore the hyperfine coupling with the nitrogen nucleus and also the excited state sublevels. Within the ground state triplet sublevels, $|m_s = 0\rangle$ and $|m_s = \pm 1\rangle$, we arbitrarily choose the $|m_s = 0\rangle$, $|m_s = 1\rangle$ sublevels. Their coupling with the driving microwave field and a decohering magnetic noise will be sufficient to explain the phenomena described here.

However, the splitting of the resonance condition between the hyperfine sublevels does cause a beating effect in the free induction decay(FID) curve(see Section 3.4). The third magnetic sublevel in the ground state triplet, $|m_s = -1\rangle$ is typically Zeeman shifted by tens of MHz and does not participate in the spin dynamics of the other two sublevels. The level diagram is illustrated in Fig. 3.1.

3.1.2 The Bloch Sphere

It can be difficult to understand the evolution of even a simple two-level quantum system. We can use a helpful visualization tool called the Bloch sphere which maps the state vector onto points on a sphere. The pseudo-spin vector drawn in the Bloch sphere points to a set of co-ordinates that represent a quantum state. In our two-level case, we can write any state in the following form

$$|\psi\rangle = c_0 |0\rangle + c_1 |1\rangle \tag{3.1}$$

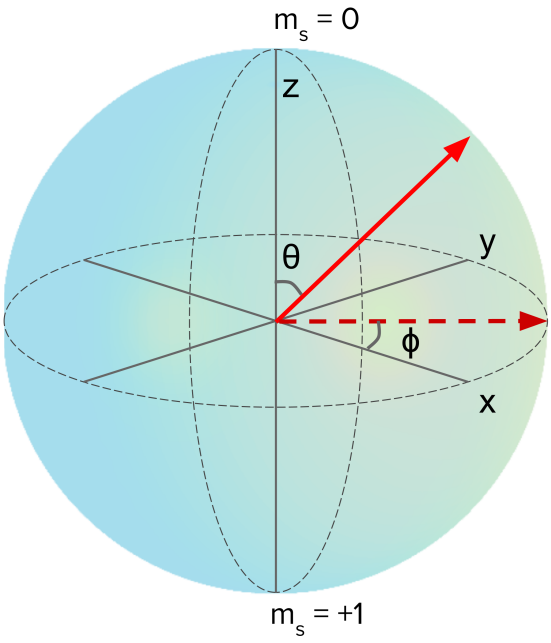


Figure 3.2: An arbitrary state on the Bloch sphere with the polar, ϕ and azimuthal angle, θ. Purely coherent states lie in the x-y plane. Statistical distributions with no coherence are restricted to the z-axis and have no x or y components.

The states correspond to the magnetic sublevels of the ground state, $|m_s = 0\rangle$ and $|m_s = +1\rangle$ separated by the zero-field splitting of 2.9 GHz, plus a small Zeeman contribution (< 10 MHz). This arbitrary state can be mapped on to the Bloch sphere by converting the wave function amplitude coefficients, c_0 and c_1 to angles θ and ϕ using the following relations

$$c_0 = sin(\theta/2) \tag{3.2}$$

$$c_1 = e^{i\phi} cos(\theta/2) \tag{3.3}$$

The Bloch sphere helps us visualize operations on the two-state system for both, pure and mixed states. All pure states lie on the surface of the sphere, while states representing statistical mixtures are interior to the sphere. The state representing a completely unpolarized distribution is represented by the point at the center of the sphere.

3.1.3 Density Matrix

The density matrix formalism presented in this chapter has been borrowed from textbooks[94, 95] and the results are compared with some recent numerical simulations on NV spin dynamics [96, 97, 98].

The density matrix lets us describe pure coherent states, statistical mixtures and also statistical mixtures of coherent states in an ensemble. We use the density matrix to describe the phenomena discussed in this chapter. The above generic state, $|\psi\rangle$ can be expressed in the form of a density matrix as

$$\rho = \begin{bmatrix} \langle |c_0|^2 \rangle & \langle c_0 c_1^* \rangle \\ \langle c_0^* c_1 \rangle & \langle |c_1|^2 \rangle \end{bmatrix} \tag{3.4}$$

The diagonal components of the density matrix represent the populations of the two energy levels, c_0 and c_1. The brackets $\langle ... \rangle$ indicate that the values are averaged over an ensemble. The off-diagonal components represent the coherence between the two states, as the coherence decays because of relaxation, we end up with a classical, product state. The off-diagonal matrix elements of the density matrix vanish for such a state.

3.1.4 Decoherence

Quantum coherences are transient; there are a number of processes that destroy coherence. These processes can be broadly divided by their respective characteristic times, T_1 and T_2.

T_1 decay, also called spin-lattice decay is easier to understand - it is simply the spontaneous transfer of populations from the excited state to the lower state and is thus the excited state lifetime. After an amount of time $t > T_1$ has passed, the density matrix will start to describe a population distribution dictated by the Boltzmann factor associated with the energy level. This type of damping is also called longitudinal relaxation because it causes the z component of the pseudo-spin in the Bloch sphere to relax towards the state representing thermal equilibrium.

For NV centers at temperatures above 1 K, thermal equilibrium populates the ground state energy levels equally (unless a considerably high magnetic field, $B > 1\ T$ is applied). In our case, this state is represented by the center of the Bloch sphere. Typical T_1 time at room temperature for NV center is a couple of milliseconds and it scales strongly with temperature [21, 99, 100].

T_2 decay is the relaxation of the transverse component of the Bloch vector; hence it is also called transverse relaxation. T_2 decay is a population-conserving decoherence effect which only operates on the coherences (off-diagonal components of the density matrix).

This type of decoherence works via two mechanisms and hence has two distinct characteristic time scales - T_2^* and T_2. The former is a classical process wherein the spin bath creates a random magnetic field at the central NV spin. This leads to the phenomena of inhomogeneous broadening[101] and a fast decay time of around 1 μs in our CVD samples. Fortunately, these thermal fluctuations are reversible and can be removed by decoupling sequences like Hahn-Echo. T_2^* sets the limits on DC magnetic and electric field sensitivity.

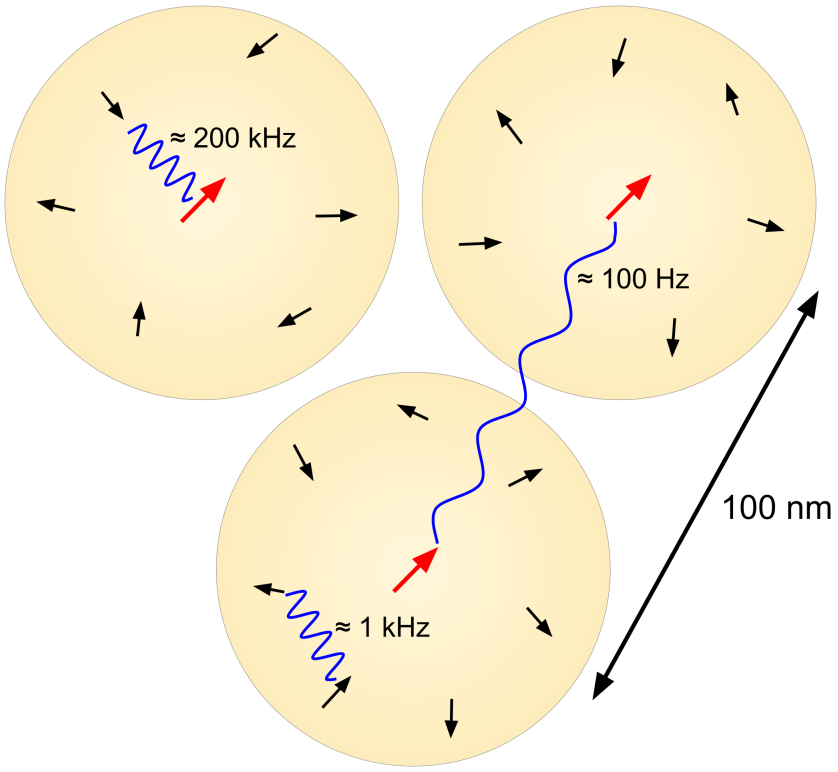


Figure 3.3: Approximate coupling strengths between different impurities. The NV centers(red) are drawn along the same [111] direction. ^{13}C nuclei(black) are oriented randomly and form the spin-bath for the NV center. Given the low intra-bath coupling between the NV centers, the ensemble can be modelled as an aggregate of non-interacting NV-^{13}C bath spin systems.

The second noise source of transverse relaxation is quantum in nature. It arises because of the evolution of the nuclear spins into superpositions of themselves. These superpositions do not commute with the bath Hamiltonian and hence are not reversible with decoupling sequences. This time constant, T_2 is revealed using decoupling sequences and is typically a few hundred microseconds for NV centers at room temperature. T_2 sets the limit on AC magnetic and electric field sensitivity.

In type Ib diamonds(E6-HPHT-1 and E6-HPHT-2), the high nitrogen content is the largest source of NV decoherence. These are called P1 centers and are paramagnetic impurities that have a concentration greater than 100 ppm. These form an electronic spin-bath that induces decoherence in the NV center at a characteristic time scale, $T_2^* \approx 0.2\,\mu s$.

The data presented in this chapter have been recorded with type IIa CVD diamonds that carry a much lower nitrogen content ($[N] < 1$ ppm). Consequently, the main source of transverse spin relaxation is from the ^{13}C nuclei which are dispersed in the carbon lattice at a natural concentration of about 1.1 %. To get a rough picture of the interaction strengths between the central NV spin and the surrounding spin-bath we can use our knowledge of the concentration of impurities and the dipole-dipole coupling Hamiltonian

$$H_{dip} = \frac{\mu_0 \gamma_x \gamma_y \hbar^2}{4\pi r^3}(\vec{S}_x.\vec{S}_y - 3(\vec{S}_x.\vec{r})(\vec{S}_y.\vec{r})), \tag{3.5}$$

where γ_x and γ_y are the gyromagnetic ratios for the two impurities, x and y, $\vec{r}$ is the vector between them and S_x and S_y are their respective spin operators.

Using the pre-factor in the above equation we can get an approximate scale of the interactions. Fig. 3.3 shows the expected interaction strengths between the different impurities in type IIa CVD diamonds calculated using this method.

If the spin-bath were just comprised of nitrogen impurities, we could expect a T_2 time as long as a few milliseconds in high purity, type IIa diamonds. However, the decoherence in these samples is dominated by the ^{13}C isotropic impurities which limits our decoherence time to a few microseconds.

On average, a ^{13}C nucleus will be found 0.5 nm from an NV center and thus will have an interaction strength of about 200 kHz. Despite the small gryomagnetic ratio associated with the ^{13}C nucleus, $\gamma_{^{13}C} = 6.7\text{x}10^7$ T^{-1}s^{-1}, it is the strongest source of decoherence because of its abundance and restricts our characteristic time constant, $T_2^* \approx 5\ \mu s$

Next, the interaction between $\gamma_{^{13}C}$ nuclei is expected to be about 1 kHz. The spin dynamics between pairs of these nuclei causes imperfect revival of spin-echoes which are revealed through dynamic decoupling sequences. This interaction limits our T_2 decoherence time to a few hundred microseconds(discussed in Section 3.5).

Finally, since we are observing ensembles of NV centers, we also have to consider the dipolar interaction between them. The CVD diamonds have a

sparse distribution of NV centers; at a few ppb, the average NV-NV distance is 100 nm. Therefore, the coupling strength is limited to about 100 Hz. Over the timescales observed in this chapter, this interaction can be neglected and we can treat our ensemble as a collection of non-interacting NV centers, in their own individual spin-baths.

This is a very simplified picture since it ignores the presence of other infrequent impurities like unpaired vacancies and boron. However, it gives us a rough scale of the spin-bath dynamics we can expect and as we shall see, it is consistent with the experimental results.

The randomly aligned ^{13}C nuclei(at temperatures greater than 1 K) generate a dipolar magnetic field at the NV center which can be modelled as an Overhauser field[102]. Since these dipoles are scattered irregularly throughout our ensemble, each NV center is in a different configuration with the surrounding ^{13}C nuclei and experiences a distinct dipolar field. The Overhauser field can be modeled as a Gaussian and stationary (zero mean) process [92]

$$C(t) = \langle \delta B_z(0) \delta B_z(t) \rangle = b^2 e^{-|t|/\tau_C}, \tag{3.6}$$

C is the correlation function, τ_C is the correlation time and b is spectral width of the noise. Both of these parameters depend on the specifics of the bath spin. The correlation time is typically hundreds of microseconds for a ^{13}C spin bath[103]. With $b >> 1/\tau_C$, A spin bath of this nature is hence called a 'slow bath'. A bath with shorter correlation times is called a 'fast bath' and, for NV defects, is usually comprised of nitrogen atoms[104].

The parameter b depends on the coupling strength between the bath spins and the central NV spin and can be calculated by evaluating the Gaussian decay curve of the free induction decay[92] as will be shown in Section 3.4. We can use the Hahn-echo technique to derive τ_C which is discussed in Section 3.5.

This magnetic noise is considered to be thermal noise, and the decoherence induced by it is reversible with dynamic decoupling sequences, the simplest of which is the Hahn-Echo sequence (discussed in Section 3.5). Thermal noise can also be attenuated by polarizing the spin bath[105].

Unlike thermal noise, the quantum noise cannot be compensated via decoupling protocols. This noise arises because of the evolution of the ^{13}C nuclei under their internal Hamiltonian[87].

3.2 Experimental Details

3.2.1 Detection Scheme

The experimental setup for measuring spin dynamics is similar to that used for ODMR except now the illuminating green laser is modulated at a frequency 2f while the microwaves are turned on and off at a frequency, f (see Fig. 3.4).

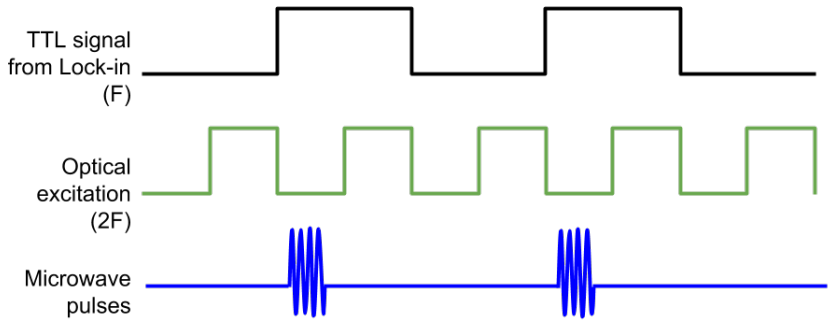


Figure 3.4: Detection scheme used for observing spin dynamics of NV centers. The laser is modulated at twice the detection frequency. The lock-in amplifier effectively measures the emitted fluorescence signal with microwaves and green laser minus the fluorescence induced from the undriven spin system.

In the first cycle of the 2f signal, we polarize the NV center's ground state into the $m_s = 0$ state and then apply microwave pulse sequences, allowing the spin state to rotate in the dark in case of FID or Hahn-echo sequences.

In the second half of the 2f cycle, the microwaves are switched off. The lock-in amplifier thus subtracts the fluorescence from the first part of the cycle where the NV center is modulated with microwaves from the second part where it is only polarized by the green laser. This differential technique allows us to observe the spin evolution as a function of the applied microwaves without the need for a special signal gating mechanism.

A commercial delay generator (Stanford Research Systems DG645)[106] is used to generate pulses of different lengths which drive the microwave switch[73] and also the Pockels cell[107] through a high voltage relay switch. Since the Pockels cell controls the width of the green laser, we can also use this setup to drive optical Rabi oscillations with a resonant red laser[108].

The green pulse serves a dual purpose - first, it polarizes the state into the $m_s = 0$ sublevel, and after the spin evolves as a result of the microwave perturbation, it measures the $m_s = 0$ content of the spin state through the same mechanism discussed in the previous chapter.

3.2.2 The Antenna

Early measurements of the ground state spin dynamics were carried out using an antenna composed of a wire carrying the microwave current. For room temperature experiments, the loop of wire was placed adjacent to the diamond. When used with the cryostat, the wire was wrapped around the microscope objective. This approach worked for ODMR since the magnitude of the Rabi frequency was not important; the contrast was always sufficient to observe the

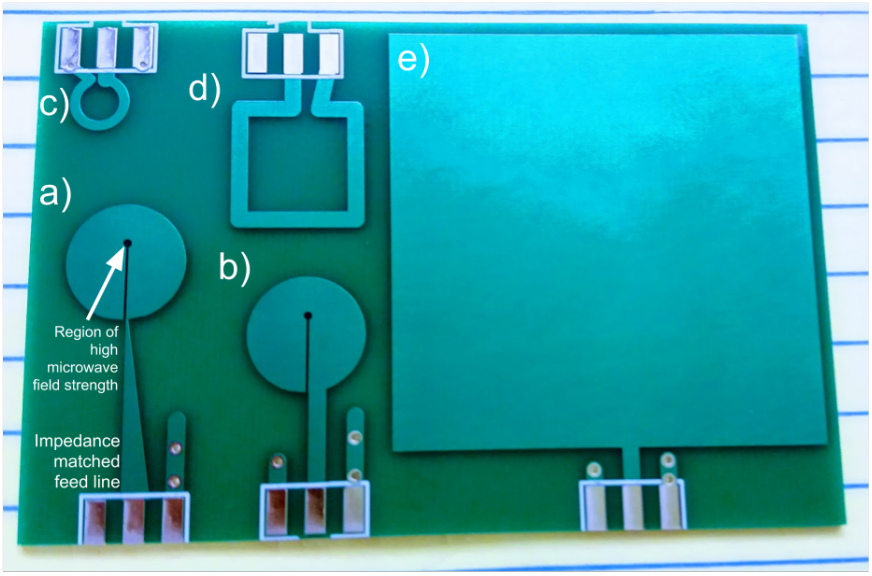


Figure 3.5: a) Antenna design used to observe spin dynamics. A 50 Ohm impedance matched line is used to feed the microwaves. The diamond is placed in the center region which is about 1 mm in diameter. b) Antenna with shorter feed line so it could be placed in the cryostat buffer window. c) and d) Half and full-wavelength loop antennae. e) Patch antenna with half-wavelength sides (10.4 cm)

ground state resonances.

However, for observing spin dynamics, the Rabi frequency was found to be too low even with a +30 dB microwave amplifier. Specifically, the maximum Rabi rate achieved with this method was 0.5 MHz. This was not acceptable for experiments like free induction decay (FID) where our decoherence time, T_2^* was a few microseconds which is comparable to the period of one Rabi cycle. This meant that a significant number of NV centers in our ensemble had decohered before a single $\pi/2$ rotation could be completed.

In order to increase the Rabi frequency, we borrowed an antenna design [109] which has a resonance frequency at 2.87 GHz(see Fig. 3.5a). The antenna bandwidth of 400 MHz allowed us to study Zeeman shifted sublevels upto a large magnetic field of 14 mT. In the small, 1 mm area in the middle of the antenna, the Rabi frequency measured was close to 20 MHz. This antenna, along with some other antennae that we experimented with are shown in Fig. 3.5.

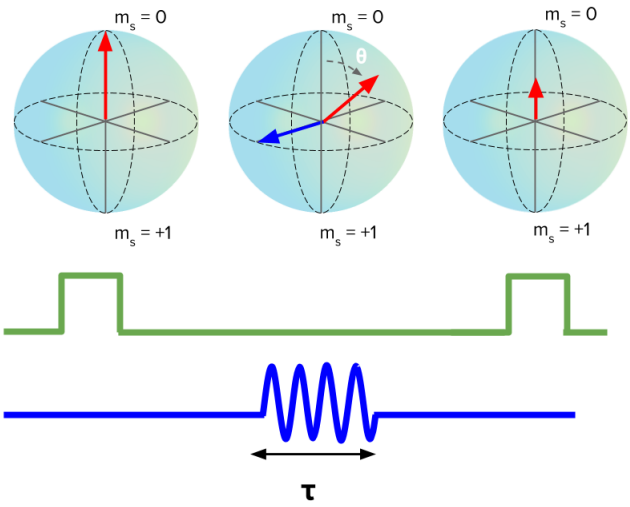


Figure 3.6: Pulse scheme used for Rabi oscillations. The green laser first prepares the state into the $m_s = 0$ state. Resonant microwaves are then applied for a variable time τ. The final green pulse projects the $m_s = 0$ component on the vertical axis.

3.3 Rabi Oscillations

3.3.1 Theory

What can we expect when we apply a resonant driving field to energy levels split as shown in Fig. 3.1? We might intuit that the electrons in the ground state will be driven to the excited state until the ground state is vacant. But instead we observe a cyclical phenomenon - the energy from the photons is first absorbed and the electrons are driven to the excited state, but subsequently, the driving field stimulates the excited level to release the energy and the electrons return to the ground state. This is called stimulated emission and is the operating principle behind lasers.

As we extend the duration of the driving field, the pseudo-spin vector keeps rotating in the Bloch sphere, alternatively pointing along $+\hat{z}$ and $-\hat{z}$ directions at a frequency proportional to the strength of the driving field. This motion describes a cyclical transfer of populations between the $m_s = 0$ and $m_s = +1$ sublevels and is called Rabi flopping or Rabi oscillation. Rabi oscillations are coherently driven rotations between two states. In our case, these are the magnetically coupled, ground state sublevels, $m_s = 0$ and $m_s = 1$, as shown in Fig. 3.1.

Using the semi-classical approach presented in [94], we can approximate the total Hamiltonian of the system as

$$H = H_0 + H_{int}, \tag{3.7}$$

H_0 is the internal Hamiltonian of the spin-system and H_{int} represents the in-

teraction between the atom and an oscillating field with magnitude B_1, this is our microwave field. In the spin basis, these two parts of the Hamiltonian can be written as

$$H_0 = -\omega_0 S_z, \tag{3.8}$$

$$H_{int} = -2\omega_x cos(\omega_L t) S_x, \tag{3.9}$$

where $2\pi\omega_0$ is the splitting of the two energy levels, about 2.9 GHz for the two levels we address in the NV center's ground state. S_z and S_x are the Pauli spin matrices, $\omega_x = \hbar\Omega_R = g_e\mu_B B_1$ is the Rabi frequency, ω_L is the frequency of the microwaves and B_1 is the magnitude of the oscillating magnetic field.

To get rid of the time dependence in our equations, we transform the lab frame into a rotating frame using the following operator

$$U(t) = e^{i\omega_L t S_z}. \tag{3.10}$$

This generates rotations about the $\hat{z}$ axis, matching the oscillation of the microwave field, ω_L.

We use the equation, $H_R = U^{-1}H_{lab}U + i\dot{U}^{-1}U$ to calculate the Hamiltonian in the rotating frame and use the rotating wave approximation to remove the remaining time dependent terms. The rotating wave approximation has been shown to break down in NV centers in the presence of a strong-driving field which exceeds the spin precession frequency($\omega_x > \omega_0$) [110], but with $\omega_0 \approx 2.8$ GHz and $\omega_1 \approx 2$ MHz, we are far from that regime in our experiments.

Now, the Hamiltonian becomes more tractable

$$H_R = \Delta\omega_0 S_z - \omega_x S_x, \tag{3.11}$$

where $\Delta\omega_0 = \omega_0 - \omega_L$ is the detuning of the microwave frequency from resonance.

Ignoring relaxation processes (both T_1 and T_2) and also assuming the driving field to perfectly match the energy level splitting, $\Delta\omega = 0$, we solve the Liousville-Von Neumann equation which describes the evolution of the density matrix, ρ under the rotating frame Hamiltonian, H_R

$$\dot{\rho} = -i[H_R, \rho] = -i[-\omega_x, s_x(t)S_x + s_y(t)S_y + s_z(t)S_z] \tag{3.12}$$

The time-dependent coefficients, s_x, s_y and s_z, describe the motion of the pseudo-spin in the Bloch sphere.

It is now trivial to solve the above differential equation

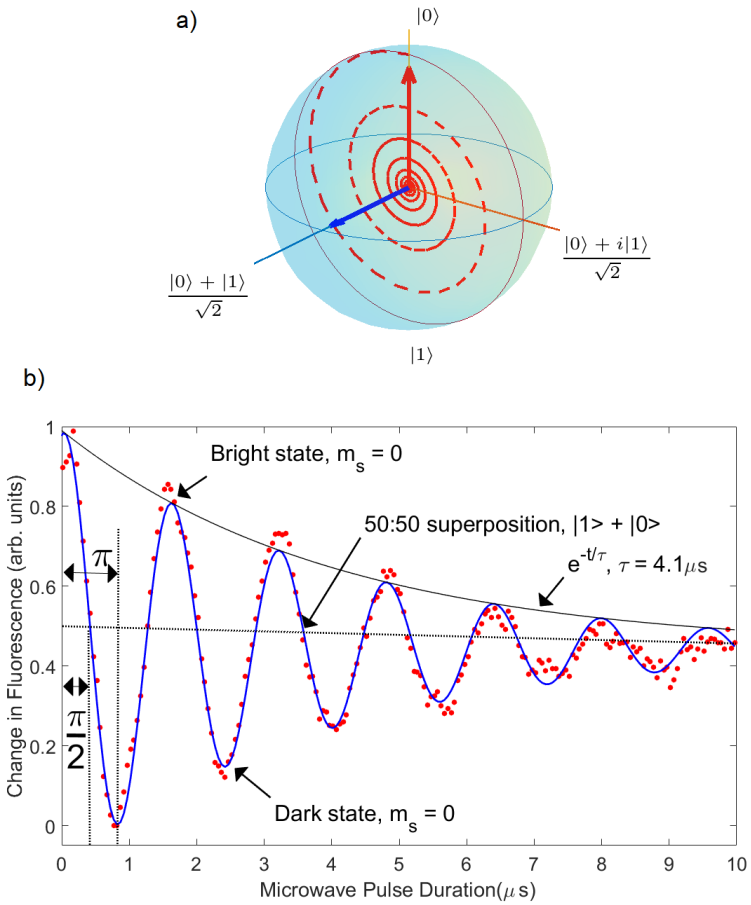


Figure 3.7: a) Simulated evolution of the spin-vector in the Bloch sphere with time constants, $T_1 = 1\ ms$ and $T_2 = 1\ \mu s$. b) Rabi curve obtained from an ensemble of NV centers. The spin oscillates coherently between the $m_s = 0$ and $m_s = 1$ states. The Rabi frequency is 0.62 MHz. The bright and dark states are distinguishable because of the preferential non-radiative intersystem crossing from the $|m_s = 1\rangle$ excited state.

$$
\begin{aligned}
s_x(t) &= 0, \\
s_y(t) &= s_z(0) sin(\omega_x t), \\
s_z(t) &= s_z(0) cos(\omega_x t).
\end{aligned} \tag{3.13}
$$

Since in our case, we are initializing the spins into $m_s = 0$ state, the initial coefficients are $s_z(0) = 1$ and $s_x(0) = 0$, $s_y(0) = 0$. That is, the spin vector points up, along the $\hat{z}$-axis. These equations describe a simple oscillatory behavior of the spin - around the $\hat{x}$-axis, in the $y - z$ plane.

So far we have ignored the interaction of the NV center with the environment. Including the phenomenological decoherence rates, $\Gamma_1 = 1/T_1$ and $\Gamma_2 = 1/T_2$, we get

$$
\begin{aligned}
\dot{s}_x &= 0, \\
\dot{s}_y &= \omega_x s_z - \Gamma_2 s_y, \\
\dot{s}_z &= -\omega_x s_y + \Gamma_1 (1 - s_z),
\end{aligned} \tag{3.14}
$$

For typical characteristic times, $T_1 = 1$ ms and $T_2 = 1$ μs and a Rabi frequency of 0.5 MHz, the evolution of this spin vector is plotted in Fig. 3.7a along with experimental data with similar characteristics.

3.3.2 Results

We now analyze the Rabi oscillations recorded with ensembles of NV centers (Fig. 3.7b). The state is first prepared in the $|m_s = 0\rangle$ ground state sub-level with an off-resonant, green laser pulse. The typical duration of this pulse is 50 μs. This aligns the spin vector in the Bloch sphere along the $\hat{z}$ direction. If we did not apply any microwaves between subsequent green laser pulses, the fluorescence observed with the second green pulse would be maximal since the electrons remain in the $|m_s = 0\rangle$ sub-level. Thus, this is the 'bright' state in our ground state triplet.

Once the laser is turned off, we turn on the microwaves. Given the comparitively long time constant of longitudinal decay ($T_1 \approx ms$)[111], the timing of the delay between the laser turning off and the microwave pulse is not vital(as long as it is less than a millisecond). The microwaves then start to apply a torque on the spin which makes the spin rotate about the $\hat{x}$-axis. The axis around which the spin rotates is determined by the phase of the driving microwave field. At that point, the phase corresponds to an arbitrary rotation around the $\hat{z}$-axis. The relative phase in multiple pulse sequences becomes important and will be discussed in the next section. The state evolves coherently on the Bloch sphere and its final location is determined by the duration of the applied microwaves.

To understand the modulation of the emitted fluorescence as a function of the

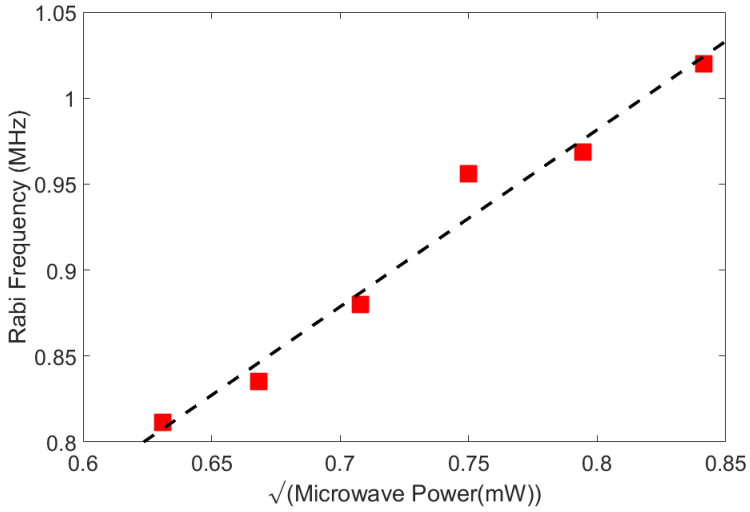


Figure 3.8: Rabi frequency plotted against the input microwave power. We can see that the Rabi frequency scales as the square root of the microwave power or linearly with the magnetic field component of the microwaves.

microwave pulse duration we first imagine a microwave pulse of infinitesimally small width. This pulse does not alter the $m_s = 0$ spin state by a significant amount and we get a large amount of emitted fluorescence since this is our 'bright' state. As the pulse length is increased, the pseudo-spin vector starts to tip away from the $\hat{z}$ axis and after a pulse of duration $\pi/2 = \pi/2\omega_x$, the spin lies in the $\hat{x} - \hat{y}$ plane and is in a coherent superposition of $m_s = 1$ and $m_s = 0$. After a pulse that is twice as long, the population has been transferred completely to the $m_s = 1$ level. When this state is illuminated with the second green laser pulse, the fluorescence is attenuated because the excited state now decays preferentially via the ISC. Therefore, this state is called the 'dark state' and the corresponding microwave pulse is called a π-pulse.

The second green laser pulse acts as a read-out, it measures the $m_s = 0$ spin content of the state after it has evolved under microwaves. It also initializes the spin state onto the $m_s = 0$ axis of the Bloch sphere, ready for the next sequence of microwaves.

We can think of the driving field as a coherent rotation operation which tips the spin vector but preserves its length. We also have other processes, however, that cause decoherence of the spin-state on the time scale of a few microseconds. This causes the exponential decay of the Rabi curve. The decay time constant for the experimental data in Fig. 3.7b is, $\tau = 4.1 \pm 0.1\ \mu s$.

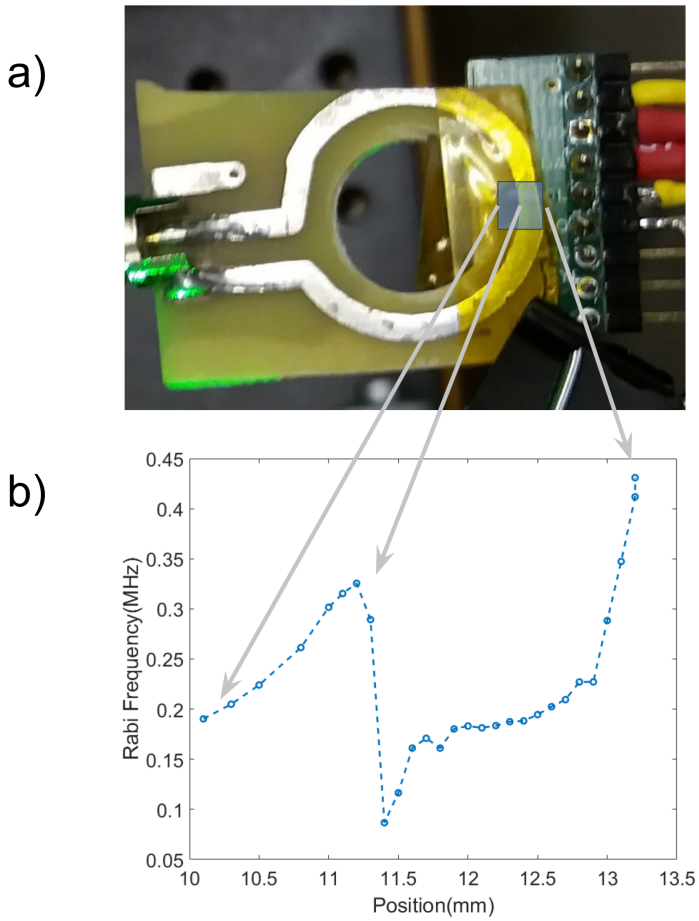


Figure 3.9: a) The diamond is mounted on the right edge of a circular antenna. b) Rabi frequency of the ensembles within the diamond as it is scanned under the confocal microscope. There is a sharp dip in the Rabi frequency at the edge of the printed trace.

3.3.3 Microwave intensity map

We know that the oscillating magnetic field, B_1, has the following relationship with the microwave source power, P_{mw} and the Rabi frequency ω_x

$$B_1 = \frac{\omega_x}{g_e \mu_B} \propto \sqrt{P_{mw}}, \tag{3.15}$$

where g_e is the gyromagnetic ratio of the electron and μ_B is the Bohr magneton. Experimentally, we can see this behavior in Fig. 3.8.

Thus we can use the Rabi frequency to build up a map of the microwave field distribution. To detect microwaves at a specific frequency, we can tune the Zeeman sublevels using a static axial magnetic field, B_z. Fig. 3.9 shows the microwave field distribution of a printed loop as measured by one NV axis in the CVD diamond ensemble. The microwave B-field component that is measured is projected in the plane perpendicular to the NV axis. We can observe a sharp drop in the Rabi frequency, and hence the microwave power at the edge of the trace suggesting that the microwaves must be near parallel to the NV axis. Since there are four NV axes within the ensemble, we can iteratively measure the different microwave field components as they map on to the NV axes, thus building up a complete vector image of the microwave field.

3.4 Free Induction Decay

3.4.1 Theory

Rabi oscillations exhibit the driven dynamics of the ground state. Using information from the Rabi decay curve, we can now observe free, or undriven spin dynamics.

Fig. 3.10 shows the pulse sequence used to observe free induction decay(FID). As in the Rabi procedure, we first prepare the spin in the $m_s = 0$ ground state. From the Rabi curve, we know how to create arbitrary superpositions of the two states, $m_s = 0$ and $m_s = 1$. Specifically, if we apply a $\pi/2$ pulse, the spin is rotated onto the $\hat{x} - \hat{y}$ plane in the Bloch sphere and we create a 50:50 superposition state: $|\psi\rangle = (|0\rangle + |1\rangle)/\sqrt{2}$. After the $\pi/2$ pulse, the system is left to evolve freely under its internal Hamiltonian for a period, τ.

After being tilted into the coherent superposition, the spin state is vulnerable to the noise from the surrounding spin bath. In the idealistic, magnetic noise-free environment, the spin would remain stationary on the Bloch sphere (in the rotating frame). However, because there is thermal noise from the surrounding spin-bath, the spin starts the dephase on account of a randomly fluctuating magnetic field, δB_z (parallel to the NV axis). The transverse noise components, δB_x and δB_y are ignored because of the large zero-field splitting of the NV center which deters any hyperfine interaction induced spin-flips.

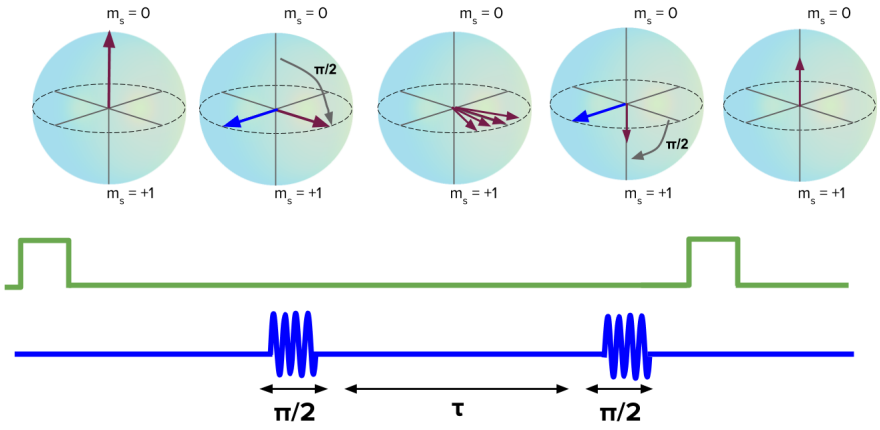


Figure 3.10: Pulse sequence used for free induction decay (FID) measurements. The spin is first prepared in the $m_s = 0$ state. It is then irradiated with a resonant microwave pulse of duration $\pi/2$. The created superposition is allowed to evolve under its internal Hamiltonian. The coherence is lost primarily through the thermal noise of the surrounding bath spins. The spin is then coherently projected on the $m_s = 1$ state with a second $\pi/2$ pulse. The phase accumulated in the FID is converted into a population difference between the $m_s = 0$ and $m_s \pm 1$ levels with the green laser.

The Gaussian width of the Overhauser field is given by[87]

$$b = \sqrt{\langle \delta B_z^2 \rangle - \langle \delta B_z \rangle^2} = \frac{1}{2}(\sum_j A_j^2)^{1/2} \tag{3.16}$$

Each NV center in our ensemble experiences a magnetic noise field that is dictated by its bath environment. Thus, there could be NV centers which are relatively free of ^{13}C in their vicinity and thus experience a long coherence time. An NV center with a large number of impurities nearby could have a significantly shorter coherence time. An NV center close to a $^{13}C -^{13} C$ dimer will also exhibit unique dynamics[112]. Experiments on single NV centers within the same diamond have revealed T_2^* decay times ranging from 0.8 to 7.5 μs[87], suggesting a wide variation in Overhauser fields, δB_z at each NV center.

As discussed earlier, b is the spectral width of the magnetic noise and A_j is the hyperfine coupling with the jth nuclear spin in the spin bath. This interaction results in a gaussian decay of the NV center with a decay constant, T_2^*

$$\langle s_z \rangle \propto -e^{-b^2\tau^2/2} = -e^{-t^2/T^{*2}}, \tag{3.17}$$

thus the dephasing time, $T_2^* = \sqrt{2}/b$. The free induction decay envelope hence allows us to calculate the spectral width of the spin bath. The internal dynamics of the spin bath occur on a much longer scale (> 100 μs) and do not manifest in FID.

On the Bloch sphere, this decoherence can be seen as the fanning out of the individual spin vectors, reducing the length of the net spin vector. After

a period, τ, a second π-pulse is applied which flips the spin onto the -$\hat{z}$ axis, representing the $|m_s = 1\rangle$ state.

The phase of the oscillating driving field determines the vector in the $\hat{x} - \hat{y}$ plane in the Bloch sphere around which the spin-vector is rotated. Since FID requires the two rotation operations to occur around the same axis, the two $\pi/2$ pulses must be phase coherent. With our apparatus, we are simply gating the microwaves applied to the antenna using a TTL signal. This method ensures that the two pulses always remain phase coherent [113]. The same applies for the three pulses used for the Hahn echo sequence in the following section.

Finally, a green laser pulse assess the population difference between the $|m_s = 0\rangle$ and $|m_s = 1\rangle$ sublevels.

3.4.2 Results

The measured free induction decay curves are shown in Fig. 3.11. The shapes of these curves depend on which hyperfine transition we are driving with resonant $\pi/2$ pulses. If we drive the middle resonance with $m_I = 0$ we observe a beating at about 2 MHz. This is because we are detuned from the $m_I = \pm 1$ resonances by this amount. See Section 2.1 for more details on the hyperfine structure of the NV center ground state.

If we park the microwave frequency at either of the side resonances with $m_I = \pm 1$, we see that the FID curve is comprised of two beat frequencies. These correspond to the distinct detunings from the other two peaks (2 MHz and 4 MHz).

We can now use the expression, $T_2^* = \sqrt{2}/b$ to calculate the spectral width of our bath. Since our time constant is 1.2 ± 0.02 μs, we get $b = 1.18 \pm 0.02$ MHz. This is the spectral width of the distribution of dipolar magnetic fields that the NV centers experience in our ensembles.

In fast baths, the decoherence time is generally longer because the spins experience from a large sample of Markovian(memory-less) Overhauser fields, δB_z. The time integral of this rapid process then quickly approaches zero. This phenomenon is called motional narrowing[113]. Conversely, for slow baths, the memory time (τ_C) is longer and thus the magnetic noise at the central spin does not average out to zero. This quasi-static environment leads to a shorter decay constant, T_2^*. However, the slow bath has its own advantage - it allows us to perform spin-echo sequences which can dramatically extend the coherence time. Spin echoes are less effective for faster spin baths.

Using the time constant, T_2^*, we can now estimate the minimum detectable magnetic field, δB using a typical CVD diamond[114]

$$\delta B = \frac{\hbar}{g_s \mu_B} \frac{1}{R\sqrt{\eta}} \frac{1}{\sqrt{N t T_2^*}}, \tag{3.18}$$

where $g_s \approx 2$ is the Lande g-factor, μ_B is the Bohr magneton, $R = 0.3$ is the op-

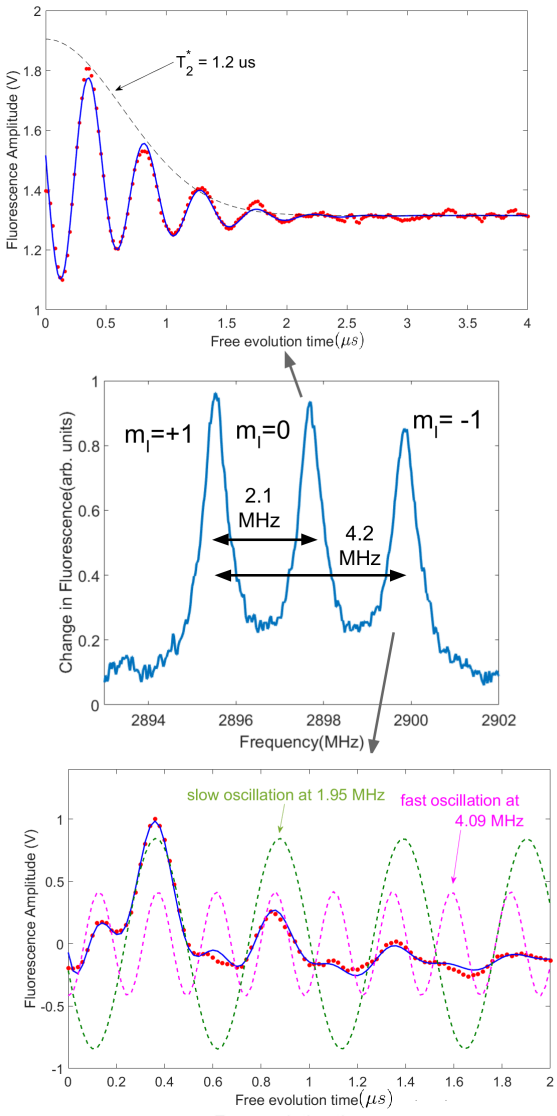


Figure 3.11: Free induction decay curves observed in the ground state. The top curve represents the free induction decay between the magnetic sublevels $|m_s = 0, m_I = 0\rangle$ and $|m_s = -1, m_I = 0\rangle$. The adjacent resonances are also being driven and since they are detuned by a frequency of about 2.1 MHz, a beating at the same frequency is observed. The bottom curve shows FID when the microwave frequency is parked at the other resonance ($m_I = -1$). Here two frequencies can be observed, 4.09 MHz and 1.95 MHz. These frequencies match the hyperfine splittings shown in Fig. 2.2.

tical contrast between the $m_s = 1$ and $m_s = 0$ states, η is the photon collection efficiency and t is the measurement time. We use the supplemental information in [115] to estimate our collection efficiency to be 2%. The poor collection efficiency can be remedied with a microscope objective with a higher numerical aperture (NA) and also using diamond geometries that limit the numbers of photons lost to total internal reflection[116].

Using these parameters the sensitivity in our 80 μm^3 ensemble containing $\approx 10,000$ NV centers is $\delta B = 1\ nT/\sqrt{Hz}$. Experiments outside the cryostat can be performed with an oil-immersion objective with a high NA, this would increase our sensitivity to $\delta B = 400\ pT/\sqrt{Hz}$.

These sensitivities apply to the ODMR detection scheme already discussed in Chapter 2. The sensitivity for electromagnetically induced transparency (EIT) is discussed in Chapter 4.

3.5 Hahn Echo

3.5.1 Theory

The phenomenon of spin echo was first discovered by Erwin Hahn in 1950 at the University of Illinois[117]. Since then it has been a staple in the NMR physicist's toolbox. It has also been adapted to laser spectroscopy and ESR (electron spin resonance) experiments.

The Hahn echo sequence is illustrated in Fig. 3.12. The microwave pulse sequence used here is: $\pi/2 \rightarrow \tau \rightarrow \pi \rightarrow \tau \rightarrow \pi/2$. Just as in FID, the first pulse sequence tips the pseudo-spin vector into the $\hat{x} - \hat{y}$ plane creating a coherent state which then evolves for a time, τ. Here the coherence decays quickly over the span a few microseconds but then a π pulse rotates all the spins that have fanned out (because of magnetic field inhomogeneities) by 180 degrees. This reverses the directions in which the slow and fast spins were moving. We again wait for a time, τ, over which the spins start to come together and form an 'echo'. At the precise moment of the echo, the second $\pi/2$ pulse rotates the state back on to the $m_s = 0$ axis.

Large spin echoes are possible for the slowly evolving ^{13}C bath. Let us examine this by taking an extreme case - the noise is not only quasi-static but constant over the period of the echo sequence. The correlation time τ_C of the bath noise is effectively infinite. Here all the spins experience a distinct non-zero magnetic field noise, δB_z that varies spatially over individual spins but not temporally. Now when we tip the spin and create a coherence with a $\pi/2$ pulse, the net spin vector will decohere on account of the different Larmor precession rates. But now if we apply the π pulse after time τ, the 180 degree reversal will rearrange the spins such that they now experience a noise field of -$\delta B_z(t)$. The spins will thus recohere perfectly after a time, τ.

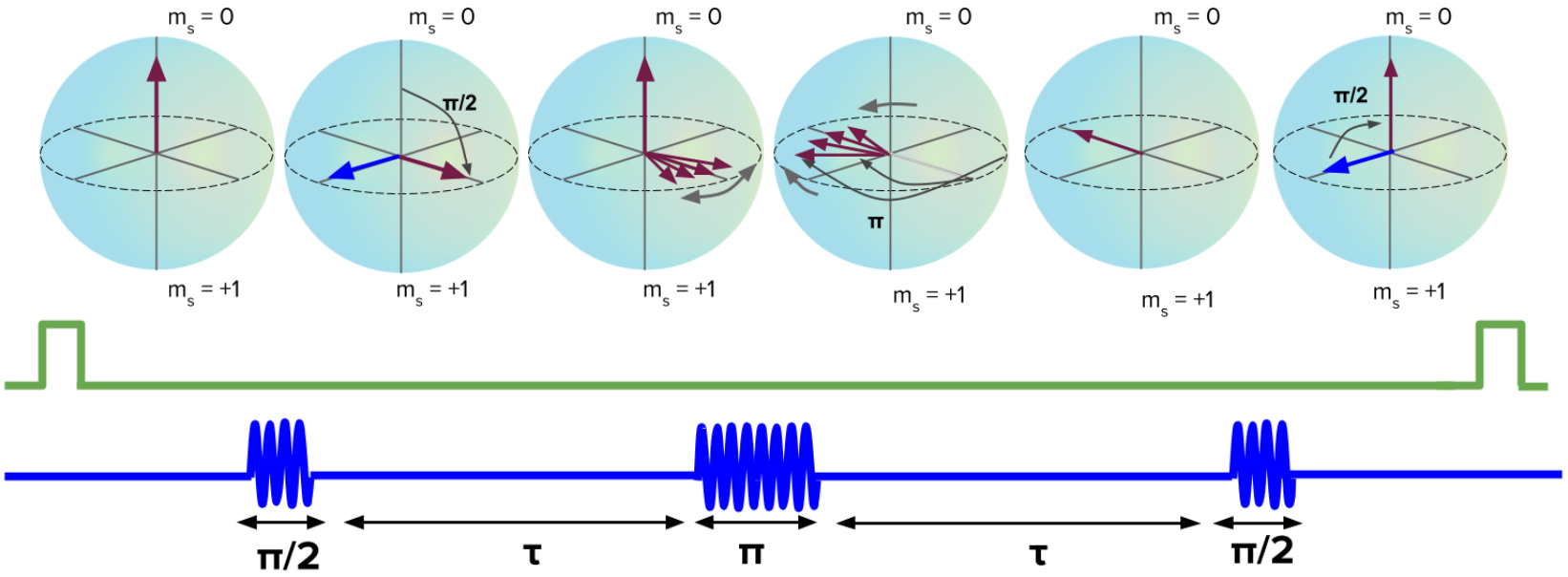


Figure 3.12: Pulse sequence used for Hahn-echo spin decoupling. First the spin is pumped into the $m_s = 0$ state with non resonant green excitation. A resonant $\pi/2$ pulse tips the spin into the x-y plane of the Rabi sphere thus creating spin coherence which then evolves with a characteristic time, T_2^*. The second microwave pulse has a duration of π, this flips the spin by 180 degrees. The effective reflection of the spins reverses their dephasing. Therefore, an echo is formed a time τ, after the π pulse.

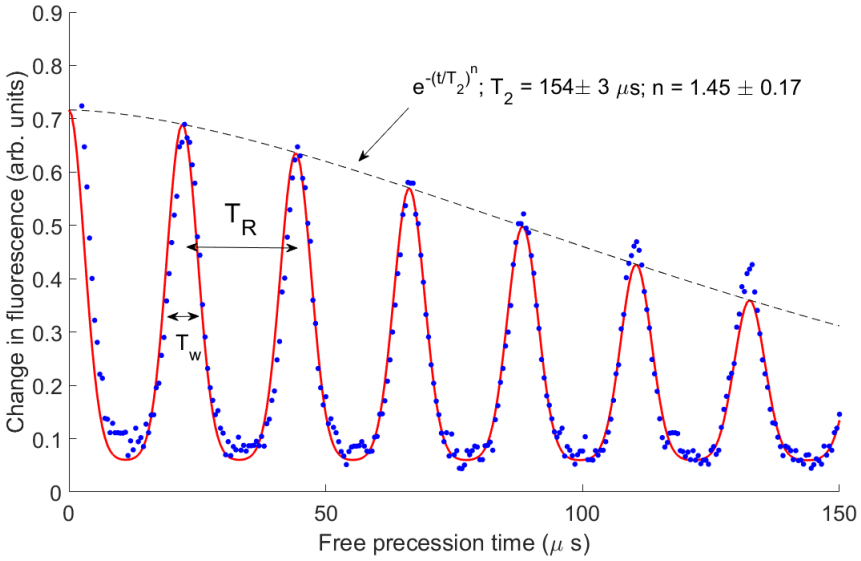


Figure 3.13: Hahn-echo decay curve. The recurrence rate for the echoes matches the Larmor frequency of the ^{13}C spin bath. After $t > T_2$, the echoes cannot be revived because of nuclear pair spin dynamics in the spin bath.

3.5.2 Results

The result from a Hahn echo sequence performed on a CVD diamond is shown in Fig. 3.13. The ^{13}C spin bath is not static as in the scenario discussed above but it is slow enough to extend T_2 over T_2^* by two orders of magnitude. The Hahn echo curve has a decay time of, $T_2 = 154\pm3\ \mu s$. This means that the variance in $\delta B_z(t)$ between the first τ period and the second must be small over this time scale. In fast baths containing ppm densities of nitrogen, the increase in T_2 is not as pronounced[118]. This is because of a short correlation time, τ_C of the magnetic noise; the magnetic field noise at the NV center has changed significantly enough to render the π pulse ineffective.

After a time $t >> T_2$, the dipole-dipole coupling between the ^{13}C nuclei, spin flip interactions and other nuclear spin-pair dynamics become significant. Since these processes are not reversible by the π-pulse, the coherence begins to be lost.

Our classical bath noise model predicts a spin echo for every delay interval, τ. As shown in Fig. 3.13, we instead observe spin echo revivals and collapses at regular intervals. The recurrence rate of these echoes closely matches the Larmor precession frequency of ^{13}C, $\gamma_C = 1.071$ kHz/G. This discrepancy arises because our bath noise model does not account for the back-action of the central NV spin on the ^{13}C nuclei.

The ^{13}C nuclei are precessing at their Larmor frequencies which are dictated by the spin state of the of central NV spin. Once the $\pi/2$ pulse creates the coherent state $|m_s = 1\rangle + |m_s = 0\rangle$, the motion of the ^{13}C spin on its own Bloch

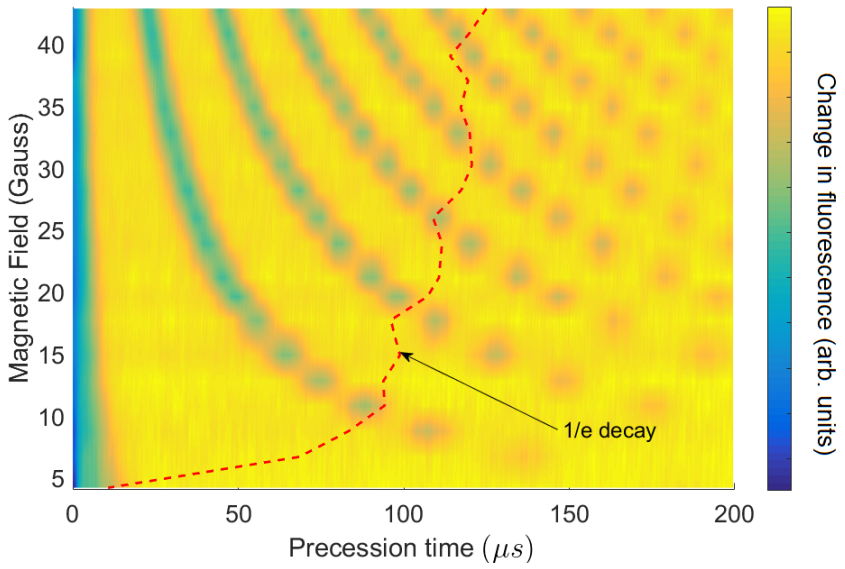


Figure 3.14: Multiple Hahn-echo curves plotted vs magnetic field. The darker blue colorings indicates a spin revival. As the magnetic field increases, the spacing between the echo revivals is reduced. This interval is equal to the Larmor period of the ^{13}C nuclei. The red line represents the T^2 time, it was obtained by fitting individual Hahn echo curves to Eq. (3.21). It can be seen that the T_2 time increases with an increasing magnetic field, as suggested by numerical simulations[39]
.

sphere is conditional on the spin state of the NV center. When the NV center is in the $m_s = 1$ state, total magnetic field at the ^{13}C nucleus is sum of the external magnetic field and the magnetic field produced via hyperfine interaction with the NV center. The effective magnetic field at the ^{13}C nucleus is the external magnetic field alone when the NV spin is in the $m_s = 0$ state. Thus, there is a universal revival of spin echoes when the pulse sequence matches the time required for the nuclear spins to complete a multiple of a Larmor cycle[39, 119].

The data in Fig. 3.13 has been fit to the following form:

$$\langle s_z \rangle = A + Be^{-(t/T)^n} \sum_j^n e^{(t-jT_r)/T_w^2}, \tag{3.19}$$

where N revival peaks occur at regularly spaced intervals of T_r. The width of each peak is T_w and the decay profile is given by e^{-t/T_2}.

For these experiments, the magnetic field was carefully aligned parallel to the NV axis using the ODMR spectrum from all four axes. A perpendicular magnetic field component causes faster decoherence of the spin echoes because the Larmor precession rate of the individual ^{13}C nuclei is modulated by its relative position with the NV center. The decay exponent n varies between

0.5 and 3, changing with the angle that the magnetic field makes with the NV axis[88].

We can use the following expression to estimate the correlation time for our spin bath noise[92]:

$$\tau_C = \frac{T_2^3 b^2}{12} \tag{3.20}$$

where b is the spectral width of the noise, determined from the FID decay rate and T_2 is our Hahn echo decay time. This gives us, $\tau_C = 400 \pm 30ms$. We can compare this to the 100 Hz homogeneous linewidth of ^{13}C nuclei in type IIa diamonds[120], suggesting an average correlation time of 10 ms. In contrast, the correlation time for a nitrogen-rich spin bath with a comparable spectral width($b = 1$ MHz) is $\tau = 10 \pm 5$ μs[121].

Fig. 3.15 shows multiple Hahn echo curves for a range of magnetic fields. We see that the decoherence time T_2 increases with the magnetic field. This result matches the simulations presented in [39]. At weak magnetic fields, the conservation of Zeeman energies between spins is not a strong requirement. As the magnetic field is increased, the Zeeman energy becomes larger than the spin-flip dipolar interaction energy and this mechanism for decoherence is suppressed.

The revival period T_R of the coherence peaks matches the Larmor precession frequency of the ^{13}C atoms. This shows that the NV center can be used a probe for its spin environment. In high nitrogen content samples, however, the dipolar field from NV centers is comparable to the intrabath dipolar field from the paramagnetic nitrogen. Thus, the NV center cannot significantly modulate the behavior of a nitrogen-rich bath.

The width of the peaks, T_w represents the decay time for the individual coherences. This has the magnetic field dependence

$$T_w \propto B^{-k}, \tag{3.21}$$

From analytical solutions, the proportionality constant, k, is 0.5. But numerical solutions with a natural frequency of ^{13}C in the spin bath indicate $k = 0.63$[39]. This difference is because of single ^{13}C nuclear spins lying close to the NV spin which create a large dipolar field, thus not satisfying the short time condition, $T \ll B^{-1}$[122]. The experimental results presented in Fig. 3.15 correspond to $k = 0.61 \pm 0.04$.

We can apply alternating electric or magnetic fields over Hahn echo or other decoupling sequences to achieve higher sensitivities. Using Eq. (3.20) to determine our sensitivity to AC magnetic fields with $T_2 = 154$ μs, we get $\delta B = 50$ $pT/\sqrt{Hz}$.

Another interesting figure-of-merit(FOM) is the product of T_2 and the qubit density, n:

$$FOM = nT_2, \tag{3.22}$$

This serves as a measure of qubit ensembles' utility for quantum applications for

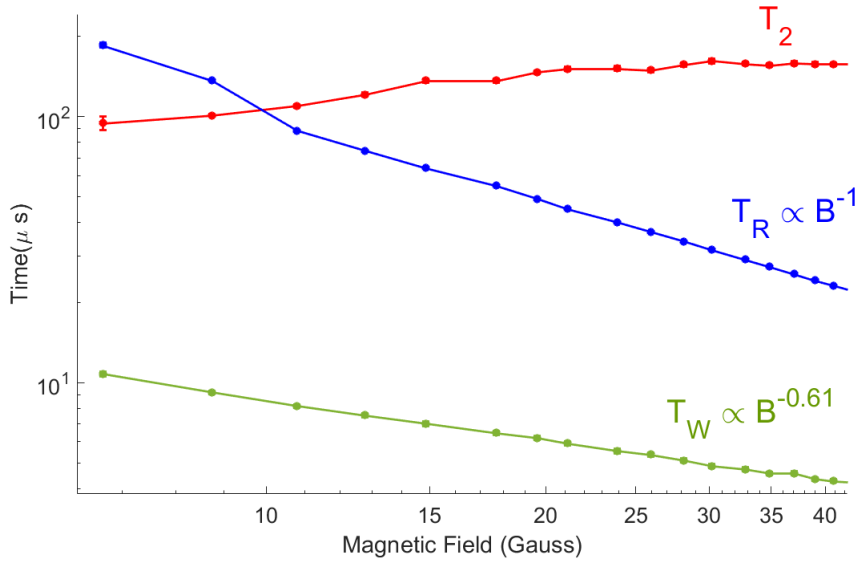


Figure 3.15: The behavior of the different time constants in the Hahn Echo sequence. T_R is the spin echo revival period and is inversely proportional to the Larmor precession rate of the ^{13}C nuclei. T_2 is the decoherence time of the spin echoes and T_w is the half-width of all coherence peaks within a single Hahn echo curve.

our CVD diamond, E6-CVD-3 with $n \approx 10$ *ppb*, under Hahn-echo decoupling, $FOM = 2.5\text{x}10^{14}$ ms cm^{-3}. This is comparable to other works with more complicated decoupling schemes with isotopically pure, ^{12}C-diamonds[121].

We can further extend the coherence times of our diamond by using more π pulses; this technique is called the CPMG decoupling sequence[123]. Operating at cryogenic temperatures has also been shown to decrease decoherence rates[21, 124].

Chapter 4

Electromagnetically Induced Transparency

The experiments discussed hitherto are useful for electric and magnetic field sensing and have given us a clear idea of the ground state's response under such fields. However, given the stringent requirement of magnetic cleanliness in the interaction region of the nEDM, it is not feasible to use an apparatus which has its own magnetic signature. This rules out wires and antennae that deliver microwaves required for ODMR sensing.

Thus, we use an all optical approach called electromagnetically induced transparency (EIT), which allows us to measure the ground state energy shifts by coherently driving optical transitions from the ground state sublevels to the spin-mixed excited state.

4.1 Theory

In order to study the light-atom interactions we can observe the changes in the medium itself or in the transmitted light after it has interacted with the medium through some reciprocal action. But upon excitation through an optically thick medium, most of the light is lost when it is tuned on resonance. A way to remedy this loss of signal is to induce a transparency window using electromagnetically induced transparency (EIT).

The three possible configurations that permit EIT[125] are shown in Fig. 4.1. In each of these, there must be two transitions between pairs of levels that are dipole allowed, and the third transition must be dipole forbidden. These may be either magnetic[126] or optical dipole transitions[127]. One of the transitions is driven weakly by a probe field while the other transition is driven by a stronger, coupling field.

EIT is a quantum phenomena which allows a normally opaque medium to become completely transparent through the destructive interference of excitation pathways within a three-level system. The first experiment to demonstrate EIT was performed with strontium atoms in 1991[128]. Here the absorption of a resonant probe laser was reduced by factor of e^{19} when a coupling laser field was applied to an adjacent transition. The Sr energy levels are arranged in a Λ-configuration(see Fig. 4.1a). EIT was subsequently demonstrated in lead vapor[129] where the three energy levels are arranged in a ladder configu-

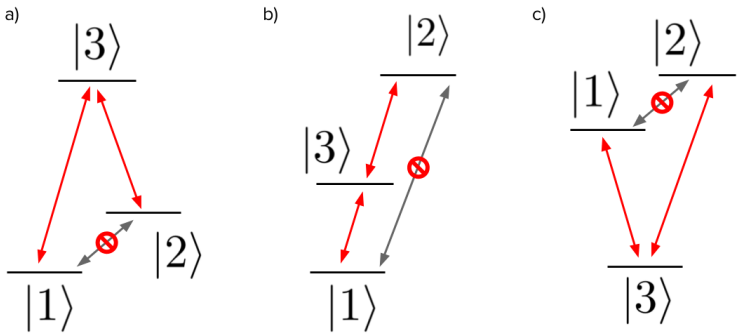


Figure 4.1: Three possible level schemes for EIT - a) Λ-system b) ladder system c) V-system. The allowed dipole transitions are drawn with red arrows. We realize the Λ system in the NV center to demonstrate EIT.

ration(see Fig. 4.1b).

There are a host of associated non-linear optical phenomena that have emerged since the discovery of EIT. One such effect is called 'slow light'. The Kramers-Kronig relations establish the dependence between the absorption coefficient of a medium and its refractive index. Since we observe sharp changes in absorption due to EIT, we must also be inducing a change in the medium's refractive index. This in turn slows the group velocity of light, $v_g << c$ [130]. Slow light was first discovered in simple, resonant systems[131] but these results were limited because of strong absorption on resonance. The phenomenon of EIT solved this problem on account of the induced transparency on resonance. EIT in a Bose-Einstein condensate was shown to slow light down to 60 mph[132]. Novel applications of slow light like optical storage, optical delay lines and light buffers have garnered interest in recent years.

Lasing without inversion (LWI) is another technique made possible with EIT. The necessary condition of population inversion for lasing is removed under LWI via the cancellation of absorption. This allows lasing to occur despite the electrons being in the ground states[133].

4.1.1 Mathematical Model for EIT

The following density matrix formalism has been developed from other work [125, 133, 134]; we subsequently simulated this MATLAB for qualitative comparison with experiments performed on CVD diamonds.

We will use the toy model illustrated in Fig. 4.1a, since the level structure used for EIT in the NV center is also the Λ system. The two lower levels are coupled to the excited state, $|3\rangle$ while $|1\rangle$ and $|2\rangle$ are isolated from each other. The Hamiltonian of this system can be written as

$$H = H_0 + H_1 \tag{4.1}$$

where H_0 is the internal, unperturbed Hamiltonian of the three non-degenerate sub-levels $|1\rangle$, $|2\rangle$ and $|3\rangle$

$$H_0 = \begin{bmatrix} \hbar\omega_1 & 0 & 0 \\ 0 & \hbar\omega_2 & 0 \\ 0 & 0 & \hbar\omega_3 \end{bmatrix}, \tag{4.2}$$

and perturbation from a laser field is written as the interaction Hamiltonian

$$H_1 = -d.\vec{E} = -\vec{E} \begin{bmatrix} 0 & 0 & d_{13} \\ 0 & 0 & d_{23} \\ d_{13} & d_{23} & 0 \end{bmatrix}. \tag{4.3}$$

Here $\vec{E}$ is the electric field and d is the dipole moment tensor (with $d_{12} = d_{21} = 0$ because of the dipole forbidden transition). To move to the appropriate rotating frame, we use the following operator

$$U(t) = e^{iH_0 t/\hbar} = -E \begin{bmatrix} e^{i\omega_1 t} & 0 & 0 \\ 0 & e^{i\omega_2 t} & 0 \\ 0 & 0 & e^{i\omega_3 t} \end{bmatrix}. \tag{4.4}$$

Making the transformation, $H^r_{int} = UH_1U^\dagger$

$$H^r_{int} = \frac{\hbar}{2} \begin{bmatrix} 0 & 0 & -\Omega_1 \\ 0 & 2(\Delta_1 - \Delta_2) & -\Omega_2 \\ \Omega_1 & \Omega_2 & 2\Delta_2 \end{bmatrix}, \tag{4.5}$$

where Ω_1 and Ω_2 are the Rabi frequencies for the two driving fields and Δ_1 and Δ_2 are the detunings from resonance. With two-photon detuning, where $\Delta_1 = \Delta_2 = 0$, we get

$$H^r_{int} = \frac{\hbar}{2} \begin{bmatrix} 0 & 0 & -\Omega_1 \\ 0 & 0 & -\Omega_2 \\ \Omega_1 & \Omega_2 & 0 \end{bmatrix}. \tag{4.6}$$

We observe that this Hamiltonian has a 0-value eigenstate $\mathcal{D}$ (which means it is decoupled from the Hamiltonian)

$$\mathcal{D} = \frac{1}{\sqrt{\Omega_1^2 + \Omega_2^2}}(\Omega_2|1\rangle - \Omega_1|2\rangle). \tag{4.7}$$

This state also has no content from the excited state. This ensures there is no possibility of excitation from it to $|3\rangle$ and hence this is called the 'dark' state. In the absorption spectrum, this leads to transparency window, the width of

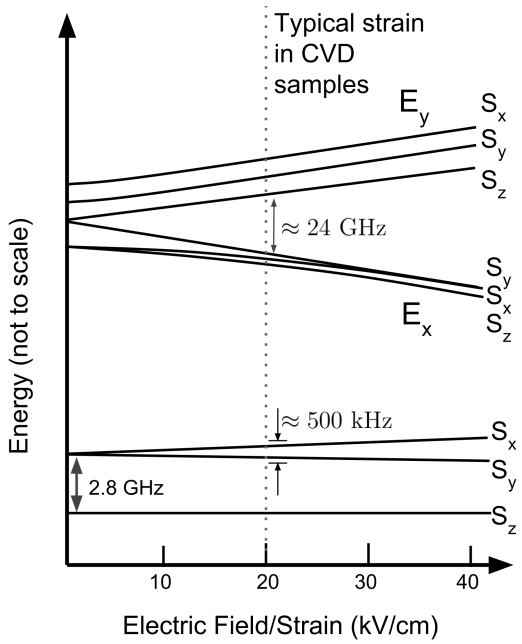


Figure 4.2: Ground and excited state energy levels as a function of strain. The E_x excited states make possible the non-cycling transitions required for a Λ-system while the E_y states displays only spin-conserving transitions on account of the unmixed $(S_x,_y) \leftrightarrow S_z$ spin character.

which is limited by the decoherence rate of this dark state.

4.1.2 EIT in Diamond

We can realize multiple Λ systems in diamond owing to the rich hyperfine structure. The excited state orbital doublet consists of two triplets, E_x and E_y. We can drive optical transitions to both of these levels. We can realize both spin-preserving and spin-flipping optical transitions in the excited state. This is shown in experiments with single NV centers that reveal the structure of their excited states [135].

At the average strain of our CVD diamonds (20 kV/cm), the excited state orbitals are split by 24 GHz. The ground state sublevels S_x and S_y are split by about 500 kHz. The higher energy orbital, E_y is responsible for spin preserving transitions while the lower orbital E_x has a mixed spin state character and thus allows spin-flipping transitions. The energy levels are illustrated in Fig. 4.2. The E_x orbital is maximally mixed at low but non-zero strains. It is possible to tune through these transitions by applying an external electric field or modulating the strain[51].

Driving resonant optical transitions using a 637 nm laser (with sidebands) allows us to establish Λ-type systems between the ground state hyperfine manifold and the excited state, E_x. The hyperfine coupling with the spin-1 nitrogen

nucleus leads to six possible Λ schemes for each of the four different species of NV centers. Hence, the EIT spectrum looks much like the ground state structure revealed in ODMR, except now, instead of using microwaves, we are probing the ground state all-optically using resonant optical transitions.

EIT in NV centers was first demonstrated in a high density sample ([NV] = 30 ppm)[127]. A large magnetic field of 0.1 T was used to bring the ground state sublevels, $m_s = 0$ and $m_s = -1$ near their avoided crossing. A Λ-system was created between these two sublevels and the excited state. An EIT feature was observed as an increase in transparency of 17%. However, since that experiment was performed with an optically thick, inhomogeneously broadened crystal, the ground state splitting could not be resolved.

Experiments at HP Labs[15] demonstrated that EIT in NV centers could be used to resolve the ground state structure. With some modifications, we recreate their experiment and demonstrate how EIT can be used for electrometry.

4.2 Experimental Setup

A necessary condition for EIT is to have a long optical depth [136]. For this purpose, it is important to choose a diamond with a sufficient concentration of NV centers with minimal inhomogeneous broadening. We used a high-purity CVD diamond, E6-CVD-1, with [NV^-]$\approx$ 8 ppb and strain (determined from ODMR spectroscopy), $\sigma \approx 20$ kV/cm. The direction of the strain is in the [100] direction (see Fig. 2.9).

To achieve a high optical depth, a corner of the 4x4x0.4 mm diamond was cleaved[137] as shown in Fig. 4.3. The cleaved edge was AR coated to minimize reflection losses. This configuration works as a waveguide which allows mulitple passes through the diamond through total internal reflection. After traversing the diamond about 17 times, the beam exits through the same cleaved edge.

An optical depth of 4.5 (99% absorption) was reached at a temperature of 77 K. The full-width-half-max of the zero phonon line (ZPL) was measured to be about 130 GHz; out of this, 50 GHz[138] can be attributed to thermal broadening.

The experimental setup for the EIT experiment is illustrated in Fig. 4.4. A tunable diode laser from New Focus[139] is coupled into a fiberized electro-optic modulator (EOM) [140]. The EOM generates side-bands on the input laser if it is supplied with a sinusoidal voltage. The sideband strength varies with the amplitude of the voltage signal. The SynthNV microwave source is used to deliver a 2.87 GHz signal at 18 dBm[71]. This generates sidebands at an intensity ratio of about 0.7:1, this is measured using a scanning Fabry-Perot[141] with a 10- GHz free spectral range. The microwave source is connected to a switch[73] which modulates the microwaves at a few kHz to facilitate lock-in detection.

Continuous excitation with the red laser tends to bleach the NV centers by photoionizing them into neutral, NV^0 centers[20, 142]. To offset this effect, a

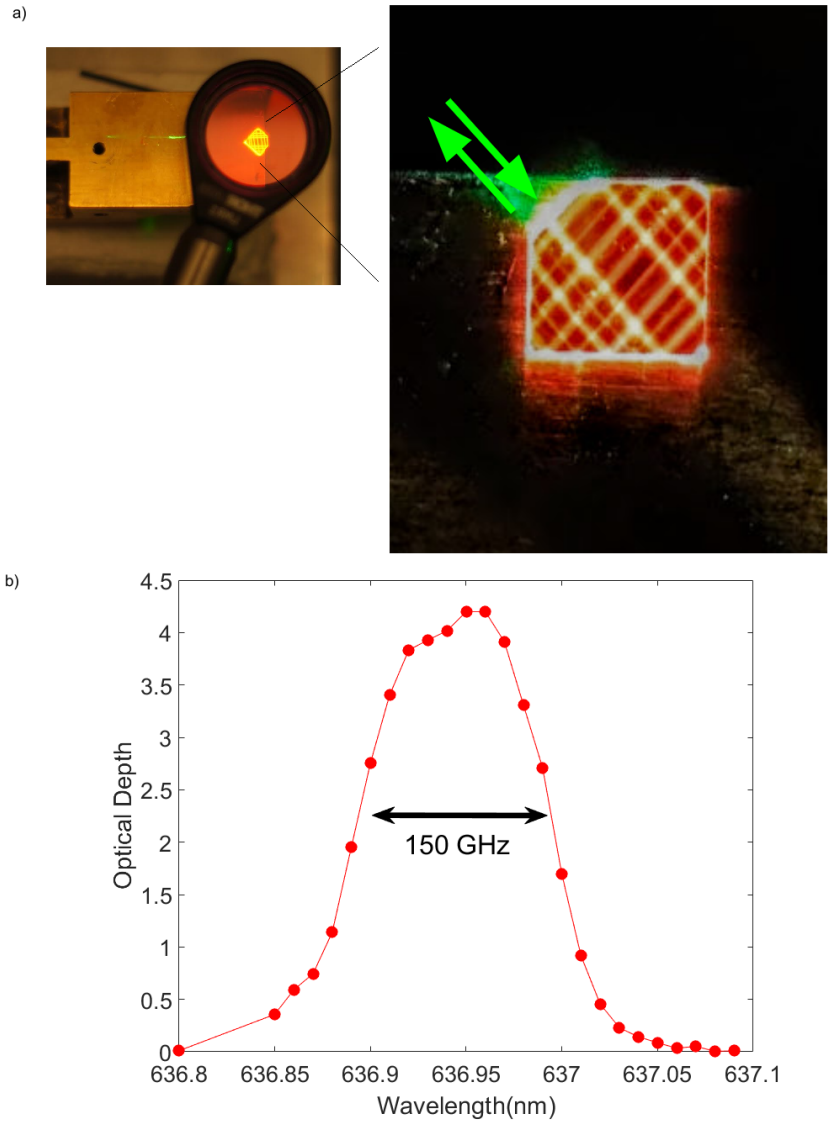


Figure 4.3: a) The diamond is cleaved on one corner to create a waveguide which allows multiple passes of the green and red lasers through total internal reflection. A red filter is used to track the optical path traced inside the diamond. b) Zero phonon line observed at 77 K. An optical depth of 4.5 (99% absorption) is achieved in this configuration.

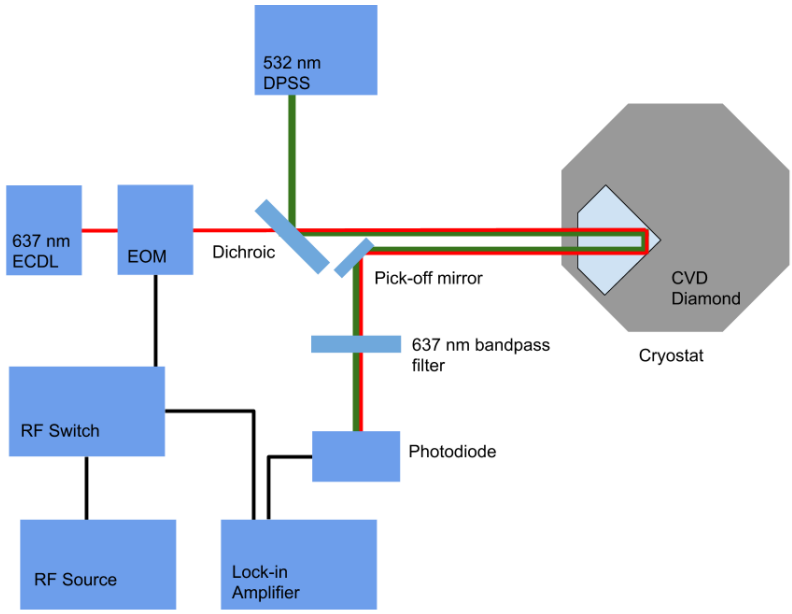


Figure 4.4: Experimental setup for EIT experiments with diamond. The green and red laser beams are combined with a dichroic mirror and alternatively chopped at 500 Hz. The diamond is held in a liquid helium cryostat which has a quartz window for optical access.

co-linear 30-mW green laser was also used in this experiment. The green laser was also useful for alignment purposes, since it allowed us to trace the optical path with the red fluorescence.

The green and red laser beams were alternated at about 500 Hz with an optical chopper in the red lasers' path and a phase-shifted TTL signal routed to the driver of the green laser. The power of the incoming green and red laser beams was 20 mW and 0.5 mW, respectively. After traversing the diamond, about 5 μW of red power returned to the photodetector.

If the experiment was being performed with optical fibers, a fiberized beam combiner was used to combine the red and green laser beams[143]. The input glass fiber had a 2-mm GRIN lens which delivered a collimated beam, 200 μm in diameter. A multimode fiber was used to collect the light after it left the diamond. The fibers were delivered to the diamond through optical feedthroughs on the cryostat.

In free space, a dichroic[144] mirror was used instead and the fiber optic feedthroughs on the cryostat were replaced with an AR coated, 4.5-mm thick quartz glass window.

The diamond was mounted in a cryostat[145] and cooled down to 77 K for measuring the optical depth and subsequently to 8 K for EIT measurements. For the fiberized version, the diamond was mounted on a quartz mount. Quartz was chosen because its coefficient of thermal expansion (0.6 K^{-1}) matched that of diamond (K^{-1}). Silver epoxy was used to glue the diamond to the mount.

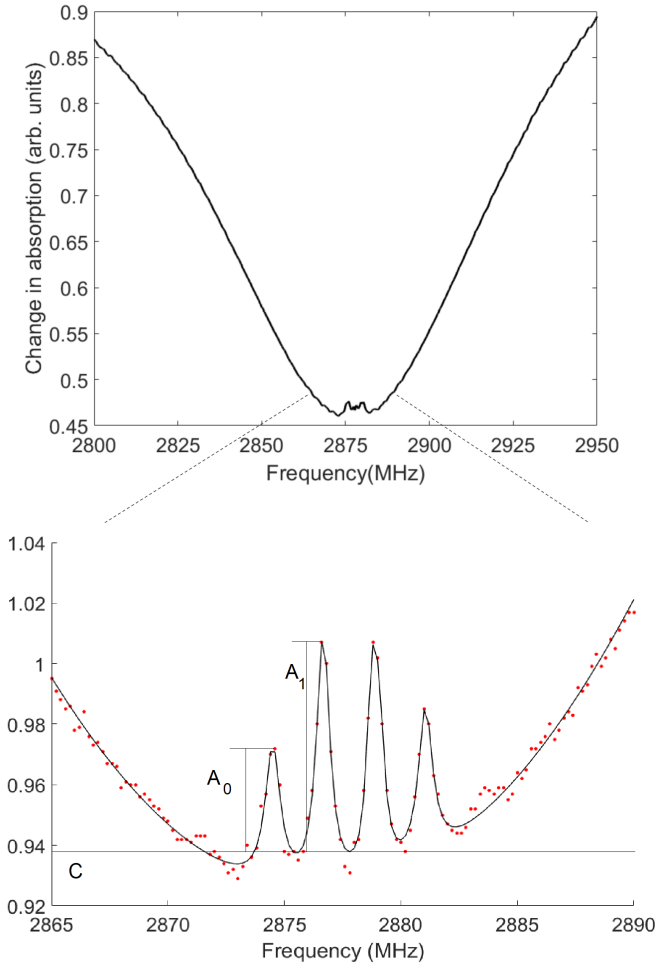


Figure 4.5: EIT features observed in diamond. The top figure shows a broad anti-hole which is a result of optical pumping. The width of this feature is about 80 MHz. The bottom graph shows the narrow EIT resonances at the bottom of the anti-hole. These are increases in transmission and have a narrow spectral width of $\nu_{EIT} = 350\ kHz$.

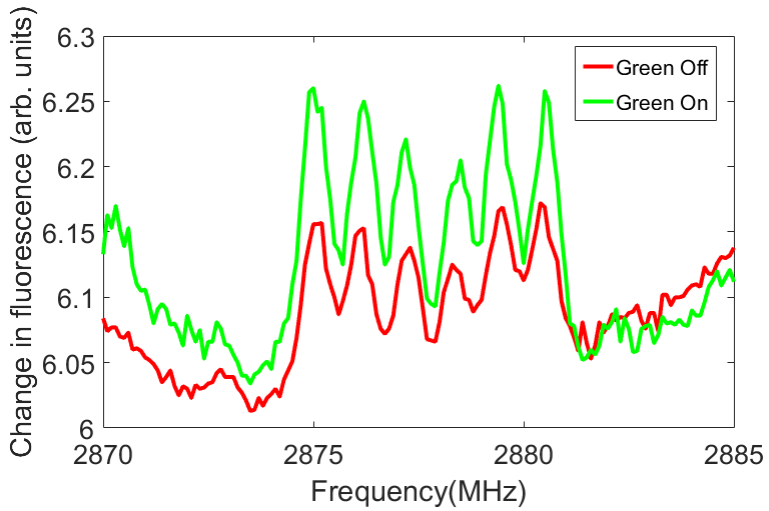


Figure 4.6: Difference in EIT contrast when the green laser is turned off and when it is turned on. The green laser is thought to undo the bleaching effect from the red laser[15]

The mount was laser milled with a CO_2 laser cutting system. Grooves for the GRIN lens as well the outgoing multi-mode fiber were machined into the quartz mount.

To apply magnetic fields, permanent magnets were used in conjunction with magnet wire wrapped around the cryostat in a Helmholtz configuration, driven by a stable current source. The coils generated a magnetic field in the [100] crystallographic direction, this is ideal for maximizing contrast in the EIT spectrum since the EIT resonances from the four crystal axes are degenerate for this magnetic field.

Upon exiting the diamond, the outgoing beam was typically a less than a millimeter from the incoming beam. This separation grew to about 2 millimeters as the beam reached the cryostat window. This deviation was likely because of the imperfect geometry of the crystal (e.g. the adjacent diamond walls not being exactly at 90 degrees to each other). The beams were separated with a D-shaped pickoff mirror and directed to a photodiode[146]. The signal from the photodiode is routed to a lock-in amplifier which was connected to a computer via a USB DAQ[147].

4.3 Results

The frequency of the coupling field was parked to the red side of the zero-phonon-line (637 nm). This ensured coupling to the spin-flipping excited state orbital, E_x. The side bands (probe fields) were scanned around the zero field splitting (ZFS) of the ground state, $D_{gs} = 2.877$ GHz.

As the probe field frequency approaches the ZFS, there is a decrease in

transparency. The coupling field is pumping the electrons out from the $m_s = 0$ state to the $m_s = \pm 1$ state. As the probe field matches the frequency of the $m_s = \pm 1 \leftrightarrow E_x$ transition, the pumping effect is undone and there is an increase in absorption. The width of this anti-hole is about 80 MHz.

When the sideband frequency exactly matches the two photon resonance condition, a sharp window of transparency (EIT) is created. The width of this feature is about 0.5 MHz. Six hyperfine resonances can be seen nestled in the middle of the anti-hole. These represent all four NV axes since the projection of the magnetic field is equal.

Over time the red laser photoionizes the NV centers and a green laser is needed to 'reset' the population of the negatively charged NV centers. For this purpose, the red and green laser pulses are alternated at 500 Hz. The difference in EIT contrast between when the green laser is used and when it is turned off can be seen in Fig. 4.6. The contrast is seen to increase by almost 100% when the green laser is used.

The EIT transparency achieved can be calculated using the method described in [15]. The EIT contrast for the inner peaks shown in Fig. 4.5 can be calculated as:

$$R = \frac{A_1}{A_1/2 + C} = 7\% \tag{4.8}$$

where the magnitudes for A_1 and C are drawn in Fig. 4.5. Similarly, the contrast for the outer peaks is, $R = 3.5\%$. This is comparable to the contrast seen in the experiment performed at HP labs, where $R = 6\%$.

4.3.1 Magnetometry

We can use the Zeeman splitting of the ground state EIT features in Fig. 4.5 to calculate the magnitude of the magnetic field (just like we would in ODMR)

$$B = \Delta\nu/\gamma = 1.10 \text{ MHz}/(28\ GHz/T) = 39\ \pm 1\ \mu T \tag{4.9}$$

where γ is the NV center's gyromagnetic ratio and $\Delta\nu$ is the separation of the inner two peaks. The uncertainty is calculated using the confidence intervals obtained from the fitting procedure.

The EIT spectra for three different magnetic fields is shown in Fig. 4.7. The bottom spectrum in this figure was recorded with just the earth's magnetic field, $B \approx 50\ \mu T$. This unaligned magnetic field causes the EIT features from the different NV axes to be indistinguishable. Once a magnetic field created by the Helmholtz coils is applied to the (100) crystal directions, the EIT features overlap and distinct peaks can be observed.

To measure shot-noise limited sensitivity for magnetic fields in the (100)

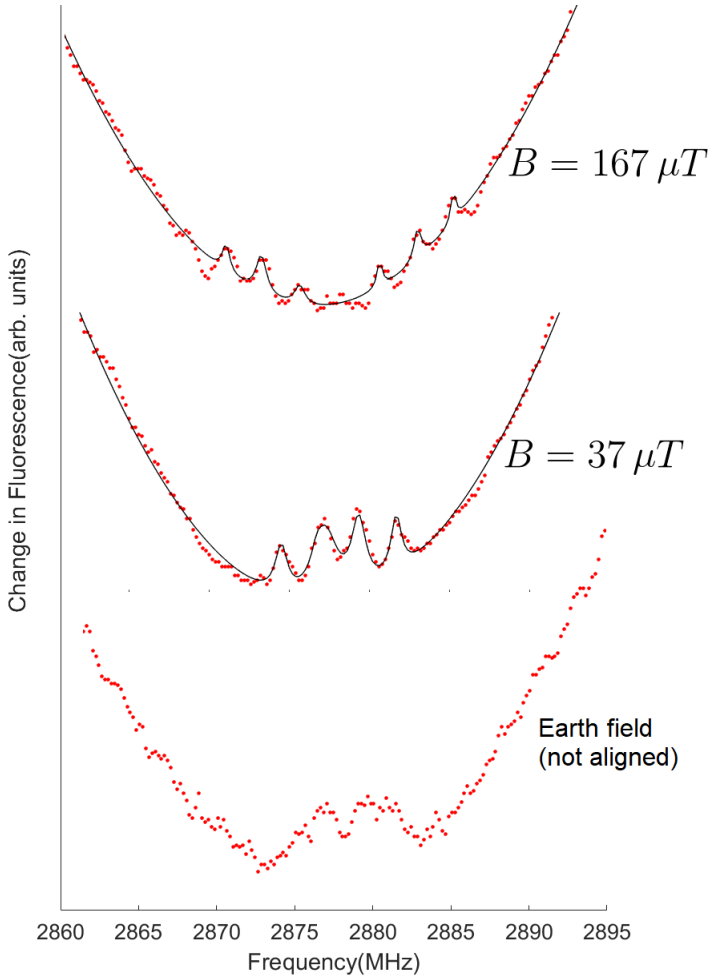


Figure 4.7: EIT spectra for three different magnetic fields. The bottom spectrum was recorded for earth's magnetic field, $B \approx 50\ \mu T$. The other two were taken with magnetic fields aligned in the (100) diamond direction.

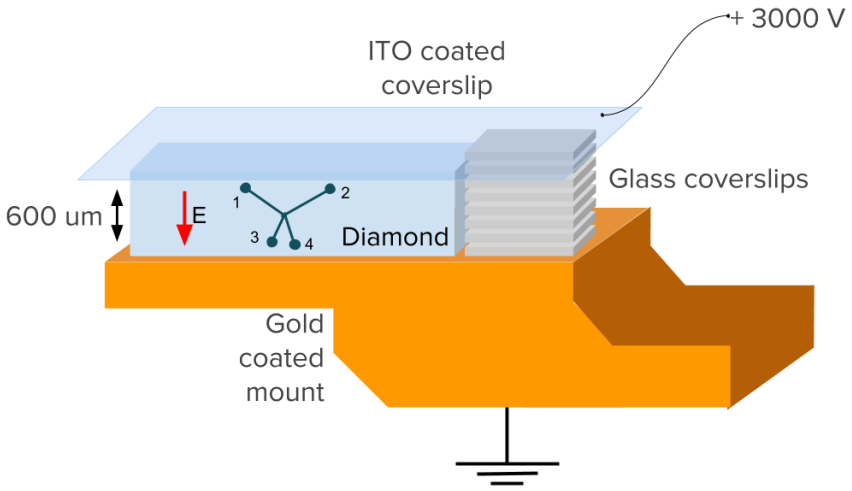


Figure 4.8: Illustration of the diamond mounted in the cryostat. An ITO coated glass slides is used to apply an electric field across the diamond. The electric field is degenerate across all four NV axes.

direction, we can use[15]

$$\delta B_{min} \approx \frac{1}{g\mu_B cos(\theta)} \frac{\Delta\nu_{EIT}}{R} \sqrt{\frac{E_p}{Pt_m}} \tag{4.10}$$

where $\theta = 57°$ is the angle of the magnetic field with respect to all four NV axes, ν_{EIT} is the EIT linewidth, R is the contrast of the EIT features, E_p is the red photon energy, P is the power at the photodetector, and t_m is the measurement time. Using this equation, we calculate our sensitivity to be, $\delta B_{min} \approx 50\ pT/\sqrt{Hz}$.

4.3.2 Electrometry

For electric field measurements, the diamond was sandwiched between the gold-coated mount and an ITO-coated coverslip suspended about 200 μm from the top of the diamond. The transparent coverslip aided the alignment of the multi-pass configuration. The coverslip was connected to a high voltage power supply through electric feedthroughs on the cryostat. As with ODMR experiments, the high vacuum environment allowed us to apply large electric fields without electrical breakdown. The electric field was degenerate for the NV centers oriented along the four crystal directions, pointing in the [100] direction. A drawing of the mount with the diamond and electrode is shown in Fig. 4.8. Simulations of this configuration also showed that the electric field inside the diamond was mostly homogeneous. Results of the COMSOL simulation are shown in Fig. 4.9.

The electric field induced Stark shifts are shown in Fig. 4.10a. At positive voltages, we are applying an electric field anti-parallel to the strain direction

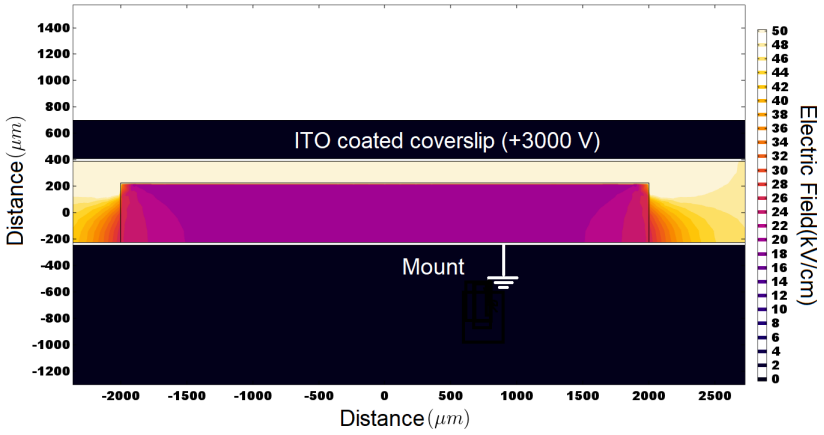


Figure 4.9: COMSOL simulation of the diamond with the electrodes configuration described in the text. The bottom of the diamond is grounded and there is an ITO coated coverslip about 200 μm from the top of the diamond. The coverslip is held at V = 3000 V in this simulation. The electric field within the diamond is largely homogeneous.

which allows us to 'cancel' the strain induced Stark shift. At a negative voltage of 3000 V, the total electric field measured is $\Pi = 36 \pm 5$ kV/cm. Subtracting the strain field($\approx$ 20 kV/cm), we get $E = 16 \pm 5$ kV/cm. The EIT spectra recorded at V = 2750 V and V = -3000 V is shown in Fig. 4.10b. The magnetic field for this data was close zero($B \approx 5\mu T$), we have therefore, extracted the electric field information from the splitting of the states $|m_s = 1, m_I = 0\rangle$ and $|m_s = -1, m_I = 0\rangle$.

As the electric field was changed, there was a corresponding change in contrast of the EIT features. We believe this is because of the tuning of the excited state orbitals with electric fields (see Fig. 4.2). Since the wavelength of the central pump beam is constant over this experiment and the excited state orbital, E_x is being modulated with the electric field, we could apply a sufficiently large electric field and tune away from the EIT system. To compensate, the wavelength of the red laser would need to be readjusted.

The COMSOL simulation (Fig. 4.9) predicts an electric field of $E = 21$ kV/cm. Since we are only sensitive to the orthogonal component of this field($d_{gs}^{\perp} \gg d_{gs}^{\parallel}$), we must multiply this by $cos(33^{\circ})$ which gives us an effective electric field of 17.6 kV/cm. This is within our experimental uncertainties.

Since diamond is a dielectric, the NV centers inside the diamond are 'shielded' from the external electric field by a factor proportional to the dielectric constant, $\kappa = 5.68 \pm 0.15$[148]. The geometry of the diamond and its orientation also influences the dielectric screening as can be seen from COMSOL[78] simulations in Fig. 4.11. The largest electric field in the diamond is achieved by operating with the electric field across the long dimension of the diamond.

In order to estimate our electric field sensitivity we can again use Eq. (4.10)

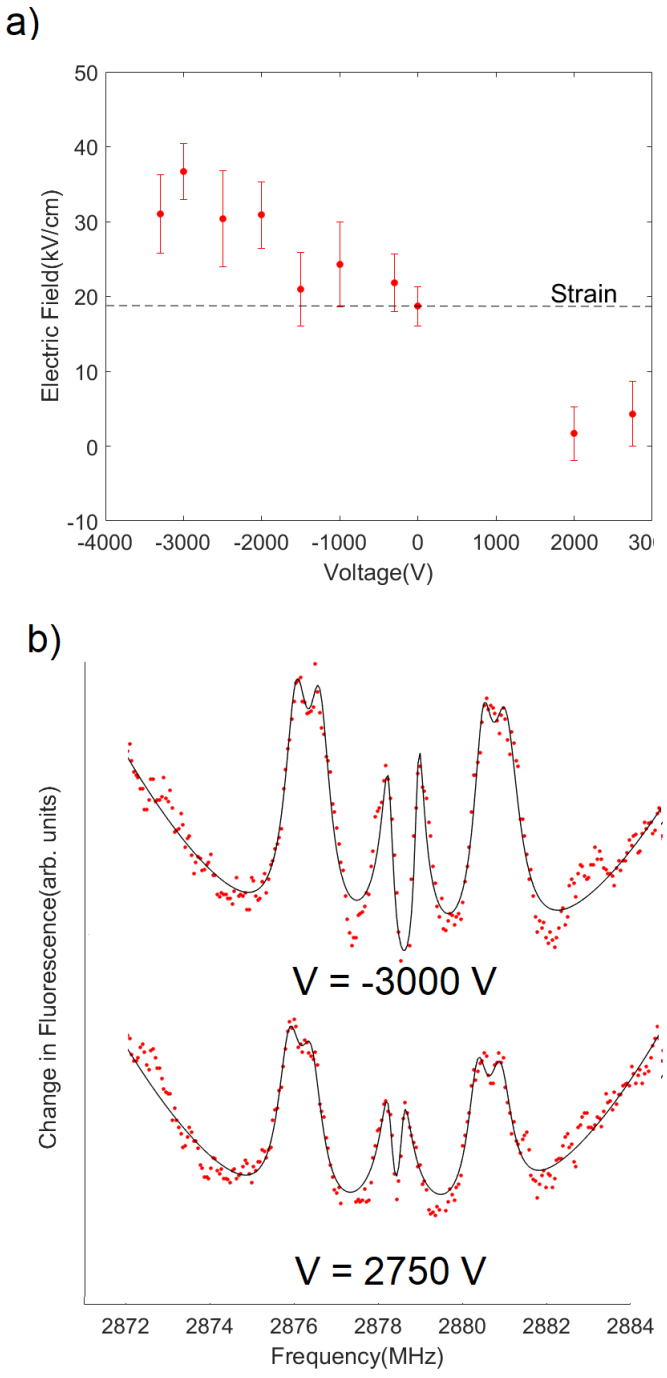


Figure 4.10: a) Electric field induced Stark shifts in the EIT spectrum. The Stark shift of the inner resonances is plotted vs the applied voltage at the ITO electrode. b) EIT data recorded at V = - 3000 V and V = 2750 V.

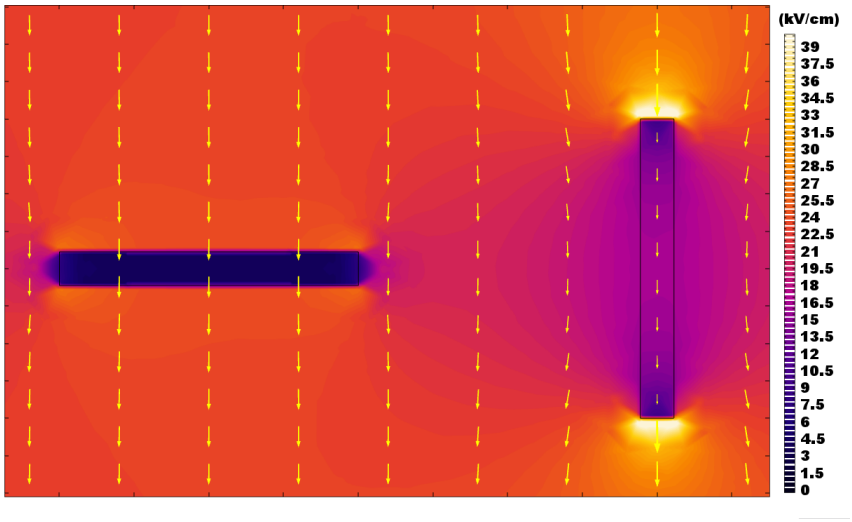


Figure 4.11: COMSOL simulation of two diamonds oriented parallel and perpendicular to an electric field. The dielectric screening effect is enhanced when the diamond is oriented perpendicular to the electric field.

by replacing $g\mu_B$ by $d_{gs}^{\perp}$[15]

$$\delta E_{min} \approx \frac{1}{d_{gs}^{\perp} cos(\theta)} \frac{\Delta\nu_{EIT}}{R} \sqrt{\frac{E_p}{Pt_m}}, \tag{4.11}$$

with typical values for ν_{EIT}, P, R and $\theta = 33°$, we get $\delta E_{min} \approx 1$ V/cm.

Thus we have demonstrated all-optical sensing of electric and mangetic field with NV centers in diamond using EIT. Further improvements in this method could be made by using isotopically pure diamonds, which would reduce the ^{13}C induced inhomogeneous broadening. Other diamond geometries could also be employed to increase the optical depth and thus improve the EIT contrast.

Chapter 5

Conclusion

In this thesis, I have discussed our work with the NV diamond project for nEDM at the University of Illinois. This work has involved different techniques for probing the ground state sublevels of the NV center and studying their response to electric fields.

Microwave induced (ODMR) techniques have helped us characterize the response of the NV ensembles to electromagnetic fields. This has allowed us to realize different regimes where electric and magnetic field sensitivities are maximized. Diamonds containing ensembles of NV centers, with printed electrodes, have also been used as electric and RF field imaging devices. The DC magnetic sensitivity for this method was about 100 nT and the DC electric field sensitivity is about 5 kV/cm.

All-optical (EIT) techniques have been demonstrated as effective ways to measure Zeeman and Stark shifts within the ground state of the NV center. A diamond sensor probed with this technique is magnetically inert and satisfies the requirements of the nEDM experiment. The DC magnetic field sensitivity achieved with this method is about 100 nT and the sensitivity to DC electric fields is about 10 kV/cm.

Free and driven spin dynamics of NV centers have also been studied. These techniques have helped us establish the spin bath environment of the NV ensembles and determine the DC and AC sensitivities to magnetic fields.

References

[1] Harald Atmanspacher. *Recasting reality : Wolfgang Pauli's philosophical ideas and contemporary science*. Springer, Berlin, 2009.

[2] C. S. Wu, E. Ambler, R. W. Hayward, D. D. Hoppes, and R. P. Hudson. Experimental test of parity conservation in beta decay. *Phys. Rev.*, 105:1413–1415, Feb 1957.

[3] J. H. Christenson, J. W. Cronin, V. L. Fitch, and R. Turlay. Evidence for the 2π decay of the k_2^0 meson. *Phys. Rev. Lett.*, 13:138–140, Jul 1964.

[4] Helen Quinn. *The mystery of the missing antimatter*. Princeton University Press, Princeton, N.J, 2008.

[5] Andrei D Sakharov. Violation of cp invariance, c asymmetry, and baryon asymmetry of the universe. *Soviet Physics Uspekhi*, 34(5):392, 1991.

[6] Sinya Aoki and Andreas Gocksch. Neutron electric dipole moment in lattice qcd. *Phys. Rev. Lett.*, 63:1125–1128, Sep 1989.

[7] Ernest Henley. *Subatomic physics*. World Scientific, Singapore Hackensack, NJ, 2007.

[8] J. H. Smith, E. M. Purcell, and N. F. Ramsey. Experimental limit to the electric dipole moment of the neutron. *Phys. Rev.*, 108:120–122, Oct 1957.

[9] J. M. Pendlebury, S. Afach, N. J. Ayres, C. A. Baker, G. Ban, G. Bison, K. Bodek, M. Burghoff, P. Geltenbort, K. Green, W. C. Griffith, M. van der Grinten, Z. D. Grujić, P. G. Harris, V. Hélaine, P. Iaydjiev, S. N. Ivanov, M. Kasprzak, Y. Kermaidic, K. Kirch, H.-C. Koch, S. Komposch, A. Kozela, J. Krempel, B. Lauss, T. Lefort, Y. Lemière, D. J. R. May, M. Musgrave, O. Naviliat-Cuncic, F. M. Piegsa, G. Pignol, P. N. Prashanth, G. Quéméner, M. Rawlik, D. Rebreyend, J. D. Richardson, D. Ries, S. Roccia, D. Rozpedzik, A. Schnabel, P. Schmidt-Wellenburg, N. Severijns, D. Shiers, J. A. Thorne, A. Weis, O. J. Winston, E. Wursten, J. Zejma, and G. Zsigmond. Revised experimental upper limit on the electric dipole moment of the neutron. *Phys. Rev. D*, 92:092003, Nov 2015.

[10] R. Golub and Steve K. Lamoreaux. Neutron electric-dipole moment, ultracold neutrons and polarized 3he. *Physics Reports*, 237(1):1 – 62, 1994.

[11] Takeyasu M Ito and the nEdm Collaboration. Plans for a neutron edm experiment at sns. *Journal of Physics: Conference Series*, 69(1):012037, 2007.

[12] V. A. Dzuba, V. V. Flambaum, and J. S. M. Ginges. Atomic electric dipole moments of he and yb induced by nuclear schiff moments. *Phys. Rev. A*, 76:034501, Sep 2007.

[13] O. P. Sushkov, V. V. Flambaum, and I. B. Khriplovich. Possibility of investigating p- and t-odd nuclear forces in atomic and molecular experiments. 60(5):873–883, 1984.

[14] Yasuhiro Masuda, Kichiji Hatanaka, Sun-Chan Jeong, Shinsuke Kawasaki, Ryohei Matsumiya, Kensaku Matsuta, Mototsugu Mihara, and Yutaka Watanabe. Spallation ucn production for nedm. *Physics Procedia*, 51:89 – 92, 2014. ESS Science Symposium on Neutron Particle Physics at Long Pulse Spallation Sources, NPPatLPS 2013.

[15] V. M. Acosta, K. Jensen, C. Santori, D. Budker, and R. G. Beausoleil. Electromagnetically induced transparency in a diamond spin ensemble enables all-optical electromagnetic field sensing. *Phys. Rev. Lett.*, 110:213605, May 2013.

[16] Dmitry Budker. *Optical Magnetometry*. Cambridge University Press, Cambridge New York, 2013.

[17] A Zaitsev. *Optical Properties of Diamond : a Data Handbook*. Springer Berlin Heidelberg, Berlin, Heidelberg, 2001.

[18] Romana Schirhagl, Kevin Chang, Michael Loretz, and Christian L. Degen. Nitrogen-vacancy centers in diamond: Nanoscale sensors for physics and biology. *Annual Review of Physical Chemistry*, 65(1):83–105, 2014. PMID: 24274702.

[19] M. V. Hauf, B. Grotz, B. Naydenov, M. Dankerl, S. Pezzagna, J. Meijer, F. Jelezko, J. Wrachtrup, M. Stutzmann, F. Reinhard, and J. A. Garrido. Chemical control of the charge state of nitrogen-vacancy centers in diamond. *Phys. Rev. B*, 83:081304, Feb 2011.

[20] K Iakoubovskii, G J Adriaenssens, and M Nesladek. Photochromism of vacancy-related centres in diamond. *Journal of Physics: Condensed Matter*, 12(2):189, 2000.

[21] N. Bar-Gill, L. M. Pham, A. Jarmola, D. Budker, and R. L. Walsworth. Solid-state electronic spin coherence time approaching one second. *Nature Communications*, 4:1743 EP –, Apr 2013. Article.

[22] L Rondin, J-P Tetienne, T Hingant, J-F Roch, P Maletinsky, and V Jacques. Magnetometry with nitrogen-vacancy defects in diamond. *Reports on Progress in Physics*, 77(5):056503, 2014.

[23] Julia Tisler, Thomas Oeckinghaus, Rainer J. Sthr, Roman Kolesov, Rolf Reuter, Friedemann Reinhard, and Jrg Wrachtrup. Single defect center scanning near-field optical microscopy on graphene. *Nano Letters*, 13(7):3152–3156, 2013. PMID: 23795752.

[24] Gopalakrishnan Balasubramanian, I. Y. Chan, Roman Kolesov, Mohannad Al-Hmoud, Julia Tisler, Chang Shin, Changdong Kim, Aleksander Wojcik, Philip R. Hemmer, Anke Krueger, Tobias Hanke, Alfred Leitenstorfer, Rudolf Bratschitsch, Fedor Jelezko, and Jörg Wrachtrup. Nanoscale imaging magnetometry with diamond spins under ambient conditions. *Nature*, 455:648 EP –, Oct 2008.

[25] Arne Wickenbrock, Huijie Zheng, Lykourgos Bougas, Nathan Leefer, Samer Afach, Andrey Jarmola, Victor M. Acosta, and Dmitry Budker. Microwave-free magnetometry with nitrogen-vacancy centers in diamond. *Applied Physics Letters*, 109(5):053505, 2016.

[26] V. M. Acosta, E. Bauch, M. P. Ledbetter, C. Santori, K.-M. C. Fu, P. E. Barclay, R. G. Beausoleil, H. Linget, J. F. Roch, F. Treussart, S. Chemerisov, W. Gawlik, and D. Budker. Diamonds with a high density of nitrogen-vacancy centers for magnetometry applications. *Phys. Rev. B*, 80:115202, Sep 2009.

[27] F. Dolde, H. Fedder, M. W. Doherty, T. Nöbauer, F. Rempp, G. Balasubramanian, T. Wolf, F. Reinhard, L. C. L. Hollenberg, F. Jelezko, and J. Wrachtrup. Electric-field sensing using single diamond spins. *Nature Physics*, 7:459 EP –, Apr 2011.

[28] M. W. Doherty, V. M. Acosta, A. Jarmola, M. S. J. Barson, N. B. Manson, D. Budker, and L. C. L. Hollenberg. Temperature shifts of the resonances of the NV^- center in diamond. *Phys. Rev. B*, 90:041201, Jul 2014.

[29] Junfeng Wang, Fupan Feng, Jian Zhang, Jihong Chen, Zhongcheng Zheng, Liping Guo, Wenlong Zhang, Xuerui Song, Guoping Guo, Lele Fan, Chongwen Zou, Liren Lou, Wei Zhu, and Guanzhong Wang. High-sensitivity temperature sensing using an implanted single nitrogen-vacancy center array in diamond. *Phys. Rev. B*, 91:155404, Apr 2015.

[30] John F. Barry, Matthew J. Turner, Jennifer M. Schloss, David R. Glenn, Yuyu Song, Mikhail D. Lukin, Hongkun Park, and Ronald L. Walsworth. Optical magnetic detection of single-neuron action potentials using quantum defects in diamond. *Proceedings of the National Academy of Sciences*, 113(49):14133–14138, 2016.

[31] F. Dolde, I. Jakobi, B. Naydenov, N. Zhao, S. Pezzagna, C. Trautmann, J. Meijer, P. Neumann, F. Jelezko, and J. Wrachtrup. Room-temperature entanglement between single defect spins in diamond. *Nature Physics*, 9:139 EP –, Feb 2013.

[32] J. H. Li, R. Yu, and X. X. Yang. Achieving slow and fast light with high transmission by nanodiamond nitrogen-vacancy center coupling to photonic crystal cavity. *Journal of Applied Physics*, 114(12):124312, 2013.

[33] Charles Santori, David Fattal, Sean M. Spillane, Marco Fiorentino, Raymond G. Beausoleil, Andrew D. Greentree, Paolo Olivero, Martin Draganski, James R. Rabeau, Patrick Reichart, Brant C. Gibson, Sergey Rubanov, David N. Jamieson, and Steven Prawer. Coherent population trapping in diamond n-v centers at zero magnetic field. *Opt. Express*, 14(17):7986–7994, Aug 2006.

[34] J. R. Weber, W. F. Koehl, J. B. Varley, A. Janotti, B. B. Buckley, C. G. Van de Walle, and D. D. Awschalom. Quantum computing with defects. *Proceedings of the National Academy of Sciences*, 107(19):8513–8518, 2010.

[35] F. J. Heremans, C. G. Yale, and D. D. Awschalom. Control of spin defects in wide-bandgap semiconductors for quantum technologies. *Proceedings of the IEEE*, 104(10):2009–2023, Oct 2016.

[36] N. B. Manson, J. P. Harrison, and M. J. Sellars. Nitrogen-vacancy center in diamond: Model of the electronic structure and associated dynamics. *Phys. Rev. B*, 74:104303, Sep 2006.

[37] Hong-Quan Zhao, Masazumi Fujiwara, and Shigeki Takeuchi. Suppression of fluorescence phonon sideband from nitrogen vacancy centers in diamond nanocrystals by substrate effect. *Opt. Express*, 20(14):15628–15635, Jul 2012.

[38] L. J. Rogers, S. Armstrong, M. J. Sellars, and N. B. Manson. Infrared emission of the NV centre in diamond: Zeeman and uniaxial stress studies. *New Journal of Physics*, 10(10):103024, October 2008.

[39] Nadn Zhao, Sai-Wah Ho, and Ren-Bao Liu. Decoherence and dynamical decoupling control of nitrogen vacancy center electron spins in nuclear spin baths. *Phys. Rev. B*, 85:115303, Mar 2012.

[40] J. R. Rabeau, P. Reichart, G. Tamanyan, D. N. Jamieson, S. Prawer, F. Jelezko, T. Gaebel, I. Popa, M. Domhan, and J. Wrachtrup. Implantation of labelled single nitrogen vacancy centers in diamond using n15. *Applied Physics Letters*, 88(2):023113, 2006.

[41] M. W. Doherty, F. Dolde, H. Fedder, F. Jelezko, J. Wrachtrup, N. B. Manson, and L. C. L. Hollenberg. Theory of the ground-state spin of the nv^- center in diamond. *Phys. Rev. B*, 85:205203, May 2012.

[42] S. Felton, A. M. Edmonds, M. E. Newton, P. M. Martineau, D. Fisher, D. J. Twitchen, and J. M. Baker. Hyperfine interaction in the ground state of the negatively charged nitrogen vacancy center in diamond. *Phys. Rev. B*, 79:075203, Feb 2009.

[43] MATLAB. *version 9.0*. The MathWorks Inc., 2017.

[44] Xing-Fei He, Neil B. Manson, and Peter T. H. Fisk. Paramagnetic resonance of photoexcited n-v defects in diamond. i. level anticrossing in the ^{3}a ground state. *Phys. Rev. B*, 47:8809–8815, Apr 1993.

[45] S. Felton, A. M. Edmonds, M. E. Newton, P. M. Martineau, D. Fisher, D. J. Twitchen, and J. M. Baker. Hyperfine interaction in the ground state of the negatively charged nitrogen vacancy center in diamond. *Phys. Rev. B*, 79:075203, Feb 2009.

[46] M. Steiner, P. Neumann, J. Beck, F. Jelezko, and J. Wrachtrup. Universal enhancement of the optical readout fidelity of single electron spins at nitrogen-vacancy centers in diamond. *Phys. Rev. B*, 81:035205, Jan 2010.

[47] Benjamin Smeltzer, Jean McIntyre, and Lilian Childress. Robust control of individual nuclear spins in diamond. *Phys. Rev. A*, 80:050302, Nov 2009.

[48] Eric Van Oort and Max Glasbeek. Electric-field-induced modulation of spin echoes of n-v centers in diamond. *Chemical Physics Letters*, 168(6):529 – 532, 1990.

[49] T. Nöbauer, K. Buczak, A. Angerer, S. Putz, G. Steinhauser, J. Akbarzadeh, H. Peterlik, J. Majer, J. Schmiedmayer, and M. Trupke. Creation of ensembles of nitrogen-vacancy centers in diamond by neutron and electron irradiation. *ArXiv e-prints*, September 2013.

[50] F. Dolde, M. W. Doherty, J. Michl, I. Jakobi, B. Naydenov, S. Pezzagna, J. Meijer, P. Neumann, F. Jelezko, N. B. Manson, and J. Wrachtrup.

Nanoscale Detection of a Single Fundamental Charge in Ambient Conditions Using the NV- Center in Diamond. *Physical Review Letters*, 112(9):097603, March 2014.

[51] Ph. Tamarat, Torsten Gaebel, J. R. Rabeau, M. Khan, A. D. Greentree, H. Wilson, L. C. L. Hollenberg, Scott P. Prawer, Philip R. Hemmer, Fedor Jelezko, and Jrg Wrachtrup. Stark shift control of single optical centers in diamond. *Physical review letters*, 97 8:083002, 2006.

[52] V. M. Acosta, C. Santori, A. Faraon, Z. Huang, K.-M. C. Fu, A. Stacey, D. A. Simpson, K. Ganesan, S. Tomljenovic-Hanic, A. D. Greentree, S. Prawer, and R. G. Beausoleil. Dynamic stabilization of the optical resonances of single nitrogen-vacancy centers in diamond. *Phys. Rev. Lett.*, 108:206401, May 2012.

[53] G. D. Fuchs, V. V. Dobrovitski, R. Hanson, A. Batra, C. D. Weis, T. Schenkel, and D. D. Awschalom. Excited-state spectroscopy using single spin manipulation in diamond. *Phys. Rev. Lett.*, 101:117601, Sep 2008.

[54] *Element 6*, (accessed February 3rd, 2018). See `http://www.element6.com` for more information on Element-6.

[55] *Nexus 670*, (accessed February 3rd, 2018). See `https://www.nist.gov/laboratories/tools-instruments/nexus-670-thermonicolet-fourier-transform-infrared-spectrometer` for more information on the FTIR instrument.

[56] G S Woods and A T Collins. The 1450 cm -1 infrared absorption in annealed, electron-irradiated type i diamonds. *Journal of Physics C: Solid State Physics*, 15(26):L949, 1982.

[57] *Prism Gem*, (accessed February 3rd, 2018). See `http://www.prismgem.com` for more information on the irradiation facility used.

[58] Simon C Lawson, David Fisher, Damian C Hunt, and Mark E Newton. On the existence of positively charged single-substitutional nitrogen in diamond. *Journal of Physics: Condensed Matter*, 10(27):6171, 1998.

[59] F. C. Waldermann, P. Olivero, J. Nunn, K. Surmacz, Z. Y. Wang, D. Jaksch, R. A. Taylor, I. A. Walmsley, M. Draganski, P. Reichart, A. D. Greentree, D. N. Jamieson, and S. Prawer. Creating diamond color centers for quantum optical applications. *Diamond and Related Materials*, 16:1887–1895, November 2007.

[60] V. M. Acosta, E. Bauch, M. P. Ledbetter, C. Santori, K.-M. C. Fu, P. E. Barclay, R. G. Beausoleil, H. Linget, J. F. Roch, F. Treussart, S. Chemerisov, W. Gawlik, and D. Budker. Diamonds with a high density of nitrogen-vacancy centers for magnetometry applications. *Phys. Rev. B*, 80:115202, Sep 2009.

[61] Peter Gielisse. *Diamond and diamond-like film applications : nucleation and growth, modeling and phase equilibria, properties and characterization, diamond-like carbon, wide bandgap, nitrides and carbides : proceedings Third International Symposium on Diamond Films, St. Petersburg, Russia, June 16-19, 1996.* Technomic Pub. Co, Lancaster, Pa, 1998.

[62] S. Sharma, Hovde C., Alghannam F., and Beck D.H. Electric and magnetic sensing with nv ensembles in diamonds. *Proc.SPIE*, 10111:10111 – 10111 – 9, 2017.

[63] Edward H. Chen, Hannah A. Clevenson, Kerry A. Johnson, Linh M. Pham, Dirk R. Englund, Philip R. Hemmer, and Danielle A. Braje. High-sensitivity spin-based electrometry with an ensemble of nitrogen-vacancy centers in diamond. *Phys. Rev. A*, 95:053417, May 2017.

[64] Marcus W. Doherty, Neil B. Manson, Paul Delaney, Fedor Jelezko, Jrg Wrachtrup, and Lloyd C.L. Hollenberg. The nitrogen-vacancy colour centre in diamond. *Physics Reports*, 528(1):1 – 45, 2013. The nitrogen-vacancy colour centre in diamond.

[65] S. Sharma, C. Hovde, D. H. Beck, and F. Alghannam. Imaging Strain and Electric Fields in NV Ensembles using Stark Shift Measurements. *ArXiv e-prints*, February 2018.

[66] *Laser glow*, (accessed February 3rd, 2018). See `http://www.laserglow.com` for more information on the 532 nm laser.

[67] *Thorlabs dichroic*, (accessed February 3rd, 2018). See `https://www.thorlabs.com/thorproduct.cfm?partnumber=DMLP605` for more information on the Thorlabs dichroic used.

[68] *Mitutoyo Objective lens*, (accessed February 3rd, 2018). See `https://www.edmundoptics.com/microscopy/infinity-corrected-objectives` for more information on the microscope objective used.

[69] *Andover optical filter*, (accessed February 3rd, 2018). See `https://www.andovercorp.com/products/colored-glass/long-wave-pass-type/` for more information on the colored filter glass used.

[70] *Avalanche Photiodiode*, (accessed February 3rd, 2018). See `https://www.thorlabs.com/thorproduct.cfm?partnumber=APD410A` for more information on photodiode used.

[71] *SynthNV microwave source*, (accessed February 3rd, 2018). See `https://windfreaktech.com/product/rf-signal-generator-and-power-detector/` for more information on the microwave source used.

[72] *30dB microwave amplifier*, (accessed February 3rd, 2018). See `https://www.minicircuits.com/pdfs/ZHL-42W+.pdf` for more information on the microwave amplifier used.

[73] *Microwave switch*, (accessed February 3rd, 2018). See `https://www.minicircuits.com/pdfs/ZSDR-230.pdf` for more information on the microwave switch used.

[74] *Confocal Microscopy*, (accessed February 3rd, 2018). See `http://forum.sci.ccny.cuny.edu/cores/microscopy-imaging/confocal-microscopy/documents/ConfocalLaserScanningMicroscopy.pdf` for more information on the formulae used to estimate the confocal microscope resolution.

[75] Thiago P. Mayer Alegre, Charles Santori, Gilberto Medeiros-Ribeiro, and Raymond G. Beausoleil. Polarization-selective excitation of nitrogen vacancy centers in diamond. *Phys. Rev. B*, 76:165205, Oct 2007.

[76] Marcis Auzinsh. *Optically polarized atoms : understanding light-atom interactions*. Oxford University Press, Oxford New York, 2010.

[77] S Doniach and M Sunjic. Many-electron singularity in x-ray photoemission and x-ray line spectra from metals. *Journal of Physics C: Solid State Physics*, 3(2):285, 1970.

[78] *COMSOL*, (accessed February 3rd, 2018). See `https://www.comsol.com` for more information on software used to simulate electric fields.

[79] C. Schreyvogel, V. Polyakov, R. Wunderlich, J. Meijer, and C. E. Nebel. Active charge state control of single nv centres in diamond by in-plane al-schottky junctions. *Scientific Reports*, 5:12160 EP –, Jul 2015. Article.

[80] Lilian Childress and Ronald Hanson. Diamond nv centers for quantum computing and quantum networks. *MRS Bulletin*, 38(2):134138, 2013.

[81] Burkhard Scharfenberger, Hideo Kosaka, William J Munro, and Kae Nemoto. Absorption-based quantum communication with nv centres. *New Journal of Physics*, 17(10):103012, 2015.

[82] Zhi-Hui Wang and Susumu Takahashi. Spin decoherence and electron spin bath noise of a nitrogen-vacancy center in diamond. *Phys. Rev. B*, 87:115122, Mar 2013.

[83] Gijs de Lange, Toeno van der Sar, Machiel Blok, Zhi-Hui Wang, Viatcheslav Dobrovitski, and Ronald Hanson. Controlling the quantum dynamics of a mesoscopic spin bath in diamond. *Scientific Reports*, 2:382 EP –, Apr 2012. Article.

[84] Pu Huang, Xi Kong, Nan Zhao, Fazhan Shi, Pengfei Wang, Xing Rong, Ren-Bao Liu, and Jiangfeng Du. Observation of an anomalous decoherence effect in a quantum bath at room temperature. *Nature Communications*, 2:570 EP –, Dec 2011. Article.

[85] Yuhei Sekiguchi, Yusuke Komura, Shota Mishima, Touta Tanaka, Naeko Niikura, and Hideo Kosaka. Geometric spin echo under zero field. *Nature Communications*, 7:11668 EP –, May 2016. Article.

[86] L. Childress, M. V. Gurudev Dutt, J. M. Taylor, A. S. Zibrov, F. Jelezko, J. Wrachtrup, P. R. Hemmer, and M. D. Lukin. Coherent dynamics of coupled electron and nuclear spin qubits in diamond. *Science*, 314(5797):281–285, 2006.

[87] Gang-Qin Liu, Xin-Yu Pan, Zhan-Feng Jiang, Nan Zhao, and Ren-Bao Liu. Controllable effects of quantum fluctuations on spin free-induction decay at room temperature. *Scientific Reports*, 2:432 EP –, May 2012. Article.

[88] P. L. Stanwix, L. M. Pham, J. R. Maze, D. Le Sage, T. K. Yeung, P. Cappellaro, P. R. Hemmer, A. Yacoby, M. D. Lukin, and R. L. Walsworth. Coherence of nitrogen-vacancy electronic spin ensembles in diamond. *Phys. Rev. B*, 82:201201, Nov 2010.

[89] T. A. Kennedy, J. S. Colton, J. E. Butler, R. C. Linares, and P. J. Doering. Long coherence times at 300 k for nitrogen-vacancy center spins in diamond grown by chemical vapor deposition. *Applied Physics Letters*, 83(20):4190–4192, 2003.

[90] Susumu Takahashi, Ronald Hanson, Johan van Tol, Mark S. Sherwin, and David D. Awschalom. Quenching spin decoherence in diamond through spin bath polarization. *Phys. Rev. Lett.*, 101:047601, Jul 2008.

[91] V. V. Dobrovitski, A. E. Feiguin, D. D. Awschalom, and R. Hanson. Decoherence dynamics of a single spin versus spin ensemble. *Phys. Rev. B*, 77:245212, Jun 2008.

[92] Zhi-Hui Wang, G. de Lange, D. Ristè, R. Hanson, and V. V. Dobrovitski. Comparison of dynamical decoupling protocols for a nitrogen-vacancy center in diamond. *Phys. Rev. B*, 85:155204, Apr 2012.

[93] V. V. Dobrovitski, A. E. Feiguin, R. Hanson, and D. D. Awschalom. Decay of rabi oscillations by dipolar-coupled dynamical spin environments. *Phys. Rev. Lett.*, 102:237601, Jun 2009.

[94] Dieter Suter. *The physics of laser-atom interactions*. Cambridge University Press, Cambridge New York, 1997.

[95] Mark Fox. *Quantum optics : an introduction*. Oxford University Press, Oxford New York, 2006.

[96] Nan Zhao, Zhen-Yu Wang, and Ren-Bao Liu. Anomalous decoherence effect in a quantum bath. *Phys. Rev. Lett.*, 106:217205, May 2011.

[97] Nan Zhao, Sai-Wah Ho, and Ren-Bao Liu. Decoherence and dynamical decoupling control of nitrogen vacancy center electron spins in nuclear spin baths. *Phys. Rev. B*, 85:115303, Mar 2012.

[98] C. A. Ryan, J. S. Hodges, and D. G. Cory. Robust Decoupling Techniques to Extend Quantum Coherence in Diamond. *Physical Review Letters*, 105(20):200402, November 2010.

[99] Mariusz Mrózek, Daniel Rudnicki, Pauli Kehayias, Andrey Jarmola, Dmitry Budker, and Wojciech Gawlik. Longitudinal spin relaxation in nitrogen-vacancy ensembles in diamond. *EPJ Quantum Technology*, 2(1):22, Oct 2015.

[100] A. Jarmola, V. M. Acosta, K. Jensen, S. Chemerisov, and D. Budker. Temperature- and magnetic-field-dependent longitudinal spin relaxation in nitrogen-vacancy ensembles in diamond. *Phys. Rev. Lett.*, 108:197601, May 2012.

[101] Nan Zhao, Zhen-Yu Wang, and Ren-Bao Liu. Anomalous decoherence effect in a quantum bath. *Phys. Rev. Lett.*, 106:217205, May 2011.

[102] Nan Zhao, Sai-Wah Ho, and Ren-Bao Liu. Decoherence and dynamical decoupling control of nitrogen vacancy center electron spins in nuclear spin baths. *Phys. Rev. B*, 85:115303, Mar 2012.

[103] Torsten Gaebel, Michael Domhan, Iulian Popa, Christoffer Wittmann, Philipp Neumann, Fedor Jelezko, James R. Rabeau, Nikolas Stavrias, Andrew D. Greentree, Steven Prawer, Jan Meijer, Jason Twamley, Philip R. Hemmer, and Jörg Wrachtrup. Room-temperature coherent coupling of single spins in diamond. *Nature Physics*, 2:408 EP –, May 2006. Article.

[104] Jing-Wei Zhou, Peng-Fei Wang, Fa-Zhan Shi, Pu Huang, Xi Kong, Xiang-Kun Xu, Qi Zhang, Zi-Xiang Wang, Xing Rong, and Jiang-Feng Du. Quantum information processing and metrology with color centers in diamonds. *Frontiers of Physics*, 9(5):587–597, Oct 2014.

[105] Susumu Takahashi, Ronald Hanson, Johan van Tol, Mark S. Sherwin, and David D. Awschalom. Quenching spin decoherence in diamond through spin bath polarization. *Phys. Rev. Lett.*, 101:047601, Jul 2008.

[106] *DG645 Delay generator*, (accessed February 3rd, 2018). See `http://www.thinksrs.com/products/DG645.htm` for more information on the digital delay generator.

[107] *Pockels Cell*, (accessed February 3rd, 2018). See `https://www.thorlabs.com/newgrouppage9.cfmobjectgroup\_id=6149` for more information on the Pockels cell.

[108] D. Andrew Golter and Hailin Wang. Optically driven rabi oscillations and adiabatic passage of single electron spins in diamond. *Phys. Rev. Lett.*, 112:116403, Mar 2014.

[109] Kento Sasaki, Yasuaki Monnai, Soya Saijo, Ryushiro Fujita, Hideyuki Watanabe, Junko Ishi-Hayase, Kohei M. Itoh, and Eisuke Abe. Broadband, large-area microwave antenna for optically detected magnetic resonance of nitrogen-vacancy centers in diamond. *Review of Scientific Instruments*, 87(5), 5 2016.

[110] K. Rama Koteswara Rao and Dieter Suter. Nonlinear dynamics of a two-level system of a single spin driven beyond the rotating-wave approximation. *Phys. Rev. A*, 95:053804, May 2017.

[111] Mariusz Mrózek, Daniel Rudnicki, Pauli Kehayias, Andrey Jarmola, Dmitry Budker, and Wojciech Gawlik. Longitudinal spin relaxation in nitrogen-vacancy ensembles in diamond. *EPJ Quantum Technology*, 2(1):22, Oct 2015.

[112] Fazhan Shi, Xi Kong, Pengfei Wang, Fei Kong, Nan Zhao, Ren-Bao Liu, and Jiangfeng Du. Sensing and atomic-scale structure analysis of single nuclear-spin clusters in diamond. *Nature Physics*, 10:21 EP –, Nov 2013.

[113] Charles Slichter. *Principles of magnetic resonance.* Springer-Verlag, Berlin New York, 1978.

[114] Dmitry Budker and Michael Romalis. Optical magnetometry. *Nature Physics*, 3:227 EP –, Apr 2007. Review Article.

[115] D. Le Sage, L. M. Pham, N. Bar-Gill, C. Belthangady, M. D. Lukin, A. Yacoby, and R. L. Walsworth. Efficient photon detection from color centers in a diamond optical waveguide. *Phys. Rev. B*, 85:121202, Mar 2012.

[116] Niels Mller Israelsen, Shailesh Kumar, Mahmoud Tawfieq, Jonas Schou Neergaard-Nielsen, Alexander Huck, and Ulrik Lund Andersen. Increasing the photon collection rate from a single nv center with a silver mirror. *Journal of Optics*, 16(11):114017, 2014.

[117] E. L. Hahn. Spin echoes. *Phys. Rev.*, 80:580–594, Nov 1950.

[118] Gijs de Lange, Toeno van der Sar, Machiel Blok, Zhi-Hui Wang, Viatcheslav Dobrovitski, and Ronald Hanson. Controlling the quantum dynamics of a mesoscopic spin bath in diamond. *Scientific Reports*, 2:382 EP –, Apr 2012. Article.

[119] Abdelghani Laraoui, Jonathan S. Hodges, Colm A. Ryan, and Carlos A. Meriles. Diamond nitrogen-vacancy center as a probe of random fluctuations in a nuclear spin ensemble. *Phys. Rev. B*, 84:104301, Sep 2011.

[120] M. J. R. Hoch and E. C. Reynhardt. Nuclear spin-lattice relaxation of dilute spins in semiconducting diamond. *Phys. Rev. B*, 37:9222–9226, Jun 1988.

[121] N. Bar-Gill, L. M. Pham, C. Belthangady, D. Le Sage, P. Cappellaro, J. R. Maze, M. D. Lukin, A. Yacoby, and R. Walsworth. Suppression of spin-bath dynamics for improved coherence of multi-spin-qubit systems. *Nature Communications*, 3:858 EP –, May 2012. Article.

[122] Wen Yang and Ren-Bao Liu. Quantum many-body theory of qubit decoherence in a finite-size spin bath. *Phys. Rev. B*, 78:085315, Aug 2008.

[123] Boris Naydenov, Florian Dolde, Liam T. Hall, Chang Shin, Helmut Fedder, Lloyd C. L. Hollenberg, Fedor Jelezko, and Jörg Wrachtrup. Dynamical decoupling of a single-electron spin at room temperature. *Phys. Rev. B*, 83:081201, Feb 2011.

[124] A. Jarmola, V. M. Acosta, K. Jensen, S. Chemerisov, and D. Budker. Temperature- and magnetic-field-dependent longitudinal spin relaxation in nitrogen-vacancy ensembles in diamond. *Phys. Rev. Lett.*, 108:197601, May 2012.

[125] J. P. Marangos. Electromagnetically induced transparency. *Journal of Modern Optics*, 45(3):471–503, 1998.

[126] Qi-Chun Liu, Tie-Fu Li, Xiao-Qing Luo, Hu Zhao, Wei Xiong, Ying-Shan Zhang, Zhen Chen, J. S. Liu, Wei Chen, Franco Nori, J. S. Tsai, and J. Q. You. Method for identifying electromagnetically induced transparency in a tunable circuit quantum electrodynamics system. *Phys. Rev. A*, 93:053838, May 2016.

[127] P. R. Hemmer, A. V. Turukhin, M. S. Shahriar, and J. A. Musser. Raman-excited spin coherences in nitrogen-vacancy color centers in diamond. *Opt. Lett.*, 26(6):361–363, Mar 2001.

[128] K.-J. Boller, A. Imamoğlu, and S. E. Harris. Observation of electromagnetically induced transparency. *Phys. Rev. Lett.*, 66:2593–2596, May 1991.

[129] K.H. Hahn, J.E. Field, and S.E. Harris. Observation of electromagnetically induced transparency in collisionally broadened lead vapor. In *Quantum Electronics and Laser Science Conference*, page QPDP2. Optical Society of America, 1991.

[130] Mark Fox. *Optical properties of solids*. Oxford University Press, Oxford New York, 2010.

[131] E Wolf. *Progress in optics*. North-Holland Pub. Co, Amsterdam, 2001.

[132] Lene Vestergaard Hau, S. E. Harris, Zachary Dutton, and Cyrus H. Behroozi. Light speed reduction to 17 metres per second in an ultracold atomic gas. *Nature*, 397:594 EP –, Feb 1999.

[133] Marlan Scully. *Quantum optics*. Cambridge University Press, Cambridge New York, 1997.

[134] Michael Fleischhauer, Atac Imamoglu, and Jonathan P. Marangos. Electromagnetically induced transparency: Optics in coherent media. *Rev. Mod. Phys.*, 77:633–673, Jul 2005.

[135] Ph Tamarat, N B Manson, J P Harrison, R L McMurtrie, A Nizovtsev, C Santori, R G Beausoleil, P Neumann, T Gaebel, F Jelezko, P Hemmer, and J Wrachtrup. Spin-flip and spin-conserving optical transitions of the nitrogen-vacancy centre in diamond. *New Journal of Physics*, 10(4):045004, 2008.

[136] Alexander I. Lvovsky, Barry C. Sanders, and Wolfgang Tittel. Optical quantum memory. *Nature Photonics*, 3:706 EP –, Dec 2009. Review Article.

[137] *Delaware Diamond Knives*, (accessed February 3rd, 2018). See `https://www.ddk.com` for more information on vendor for polishing and cleaving diamonds.

[138] Kai-Mei C. Fu, Charles Santori, Paul E. Barclay, Lachlan J. Rogers, Neil B. Manson, and Raymond G. Beausoleil. Observation of the dynamic jahn-teller effect in the excited states of nitrogen-vacancy centers in diamond. *Phys. Rev. Lett.*, 103:256404, Dec 2009.

[139] *New Focus 637 nm Laser*, (accessed February 3rd, 2018). See `https://www.newport.com/f/velocity-633-1790-nm-wide-\&-fine-tuning-lasers` for more information on external cavity diode laser used.

[140] *Jenoptik EOM*, (accessed February 3rd, 2018). See `https://www.jenoptik.us/products/optoelectronic-systems/light-modulation/integrated-optical-modulators-fiber-coupled` for more information on EOM used.

[141] *Scanning Fabry Perot*, (accessed February 3rd, 2018). See `https://www.thorlabs.com/thorproduct.cfm?partnumber=SA210-3B` for more information on the Scanning Fabry-Perot interferometer.

[142] N Aslam, G Waldherr, P Neumann, F Jelezko, and J Wrachtrup. Photo-induced ionization dynamics of the nitrogen vacancy defect in diamond investigated by single-shot charge state detection. *New Journal of Physics*, 15(1):013064, 2013.

[143] *OzOptics Beam Combiner*, (accessed February 3rd, 2018). See `https://www.ozoptics.com/ALLNEW\_PDF/DTS0095.pdf` for more information on fiberized beam combiners.

[144] *636fsx10-025 dichroic*, (accessed February 3rd, 2018). See `https://www.andovercorp.com/static/pdf/catalog.pdf` for more information on the dichroic mirror used for EIT.

[145] *Infrared Labs*, (accessed February 3rd, 2018). See `http://www.infraredlaboratories.com` for more information on the commerical cryostat used.

[146] *Thorlabs photodiode*, (accessed February 3rd, 2018). See `https://www.thorlabs.com/thorproduct.cfm?partnumber=DET10A` for more information on the photodiode used.

[147] *National Instruments DAQ*, (accessed February 3rd, 2018). See `http://www.ni.com/en-us/support/model.usb-6008.html` for more information on DAQ used.

[148] *CVD Diamond Handbook from Element-6*, (accessed February 3rd, 2018). See `https://e6cvd.com/media/wysiwyg/pdf/E6_CVD_Diamond_Handbook_A5_v10X.pdf` for more information on CVD diamonds from Element 6.

Appendix : MATLAB Code

```
% The following code simulates the ground state sublevels
    of all four NV axes in a tetrahedral diamond lattice
function varargout = NVCenter(varargin)
gui_Singleton = 1;
gui_State = struct('gui_Name',       mfilename, ...
    'gui_Singleton',  gui_Singleton, ...
    'gui_OpeningFcn', @NVCenter_OpeningFcn, ...
    'gui_OutputFcn',  @NVCenter_OutputFcn, ...
    'gui_LayoutFcn',  [] , ...
    'gui_Callback',   []);
if nargin && ischar(varargin{1})
    gui_State.gui_Callback = str2func(varargin{1});
end

if nargout
    [varargout{1:nargou5t}] = gui_mainfcn(gui_State,
        varargin{:});
else
    gui_mainfcn(gui_State, varargin{:});
end
function NVCenter_OpeningFcn(hObject, eventdata, handles,
    varargin)
global Bx Bz By mub g  D x piz dpar dperp pix piy aperp
   apar  P gpar gperp planck;

syms Bx Bz By mub g h D x piz dpar dperp pix piy aperp
   apar P gpar gperp planck real;
rotate3d on;
handles.NVAxis = zeros(3,4);

handles.NVAxis(:,1) = [0,0,1];
handles.NVAxis(:,2) = [0.94280904178,0,-0.33333333276];
handles.NVAxis(:,3) =
```

```
    [-0.47140452133,0.81649658085,-0.33333333276];
handles.NVAxis(:,4) =
    [-0.47140452133,-0.81649658085,-0.33333333276];
theta = -29.963*pi/180;
rotationMat1 = [cos(theta),-sin(theta),0;sin(theta),cos(
    theta),0;0,0,1];
rotationMat1 = eye(3);

handles.NVAxis(:,1) = (rotationMat1 * handles.NVAxis(:,1)
    )';
handles.NVAxis(:,2) = (rotationMat1 * handles.NVAxis(:,2)
    )';
handles.NVAxis(:,3) = (rotationMat1 * handles.NVAxis(:,3)
    )';
handles.NVAxis(:,4) = (rotationMat1 * handles.NVAxis(:,4)
    )';

theta = (90-54.735610310247) * pi/180;

rotationMat = [cos(theta), 0, sin(theta); 0,1,0; -sin(
    theta),0,cos(theta)];

ninetyDegRot = [0,0,1;0,1,0;-1,0,0];
rotationMat  =rotationMat;

%comment the following to change to 100 geometry
rotationMat = eye(3);
handles.NVAxis(:,1) = (rotationMat * handles.NVAxis(:,1))
    ';
handles.NVAxis(:,2) = (rotationMat * handles.NVAxis(:,2))
    ';
handles.NVAxis(:,3) = (rotationMat * handles.NVAxis(:,3))
    ';
handles.NVAxis(:,4) = (rotationMat * handles.NVAxis(:,4))
    ';
rotationMat
handles.NVAxis(:,1)
printLatex(handles.NVAxesTag, latex(vpa(handles.NVAxis,2)
    ));

handles.Sx=[0,1/sqrt(2),0;1/sqrt(2),0,1/sqrt(2);0,1/sqrt
    (2),0];
handles.Sy=[0,1/(j* sqrt(2)),0;-(1/(j*sqrt(2))),0,1/(j*
```

```
    sqrt(2));0,-(1/(j*sqrt(2))),0];
handles.Sz=[1,0,0;0,0,0;0,0,-1];
handles.Iz = handles.Sz; handles.Ix = handles.Sx; handles
    .Iy = handles.Sy;
I = eye(3);
handles.Sxgrave =  kron(handles.Sx,I);
handles.Sygrave =  kron(handles.Sy,I);
handles.Szgrave =  kron(handles.Sz,I);
handles.SzSq = handles.Sz*handles.Sz;
handles.SxSq = handles.Sx*handles.Sx;
handles.SySq = handles.Sy*handles.Sy;
handles.SxSy = handles.Sx*handles.Sy;
handles.SySx = handles.Sy*handles.Sx;

handles.SxSyGrave = kron(handles.SxSy,I);
handles.SySxGrave = kron(handles.SySx,I);

handles.SxSqGrave = kron(handles.SxSq,I);
handles.SySqGrave = kron(handles.SySq,I);
handles.SzSqGrave = kron(handles.SzSq,I);
handles.IzSqAcute = kron(I,handles.Iz*handles.Iz);

Bvec = [Bx,By,Bz];

H0 = D*handles.SzSqGrave + P*handles.IzSqAcute+apar*kron(
    handles.Sz,handles.Iz) + aperp *(kron(handles.Sx,
    handles.Ix) + kron(handles.Sy,handles.Iy));
Hmag =  mub * g*(handles.Sxgrave*Bvec(1)+handles.Sygrave*
    Bvec(2)+handles.Szgrave*Bvec(3))/planck;
Helec =      dpar * piz * handles.SzSqGrave - dperp *(pix
    * (handles.SxSyGrave+handles.SySxGrave) + piy * (
    handles.SxSqGrave-handles.SySqGrave));
handles.H = simplify(H0 +Hmag+Helec,'steps',5);
handles.Htemp = subs(handles.H,h,1);

%have to print the Hamiltonian in 3 bits because Latex
    interpreter can not
%handle large matrix dimensions

latex(Helec(1:9,1:9))

latext =latex(Helec(1:9,1:9));
latext = strrep(latext,'\left(\begin{array}','\begin{
```

```
    array}');
93  latext = strrep(latext,'\right','');
94  latext2 =latex( handles.Htemp(1:9,4:5));
95  latext2 = strrep(latext2,'\left(','');
96  latext2 = strrep(latext2,'\right','');
97  latext3 =latex( handles.Htemp(1:9,6:7));
98  latext3 = strrep(latext3,'\left(','');
99  latext3 = strrep(latext3,'\right','');
100 latext4 =latex( handles.Htemp(1:9,8:9));
101 latext4 = strrep(latext4,'\left(','');
102 latext4 = strrep(latext4,'\right','');
103 s = strcat('\mathcal{H} = ',latext);
104 printLatex(handles.hamiltonian1Axes, s);
105 printLatex(handles.hamiltonian2Axes, latext2);
106 printLatex(handles.hamiltonian3Axes, latext3);
107 printLatex(handles.hamiltonian4Axes, latext4);
108
109 handles.output = hObject;
110 guidata(hObject, handles);
111
112 calculateHamiltonian(handles, hObject)
113
114
115 function [eigenvalues eigenvectors] =
    calculateEigenvalues(Hamiltonian, B,PI)
116 global Bx By Bz mub g h D rat dpar dperp pix piy piz
    aperp planck;
117
118 eigenvalues = [0,0,0];
119 eigenvectors = [0,0,0];
120
121 Hamiltonian=subs(Hamiltonian,Bx,B(1));
122 Hamiltonian=subs(Hamiltonian,By,B(2));
123 Hamiltonian=subs(Hamiltonian,Bz,B(3));
124 Hamiltonian=subs(Hamiltonian,pix,PI(1));
125 Hamiltonian=subs(Hamiltonian,piy,PI(2));
126 Hamiltonian=subs(Hamiltonian,piz,PI(3));
127 [eigenvalues,eigenvectors] = eig(Hamiltonian);
128
129
130 function calculateHamiltonian(handles, hObject)
131 set(handles.statusText,'String','Calculating...')
132
```

```
133 digits(7)
134 format long
135 global Bx By Bz mub g h D dpar dperp pix piy piz apar
        aperp P gpar gperp planck;
136 handles.hval = 6.62607004 * 10^-34;
137 handles.mub = 9.27400968*10^-24;
138 handles.pi = [0,0,0];
139 handles.Bx = (10^-7)*str2num(get(handles.Bxedit,'String')
        );
140 handles.By = (10^-7)*str2num(get(handles.Byedit,'String')
        );
141 handles.Bz = (10^-7)*str2num(get(handles.Bzedit,'String')
        );
142 handles.P = (-4.945 * 10^6);
143 handles.apar = (-2.166 * 10^6);
144 handles.aperp = (-2.70 * 10^6);
145 handles.basis = {'|m_S = 1; m_I = 1>','|m_S = 1; m_I = 0>
        ','|m_S = 1; m_I = -1>','|m_S = 0; m_I = 1>','|m_S =
        0; m_I = 0>','|m_S = 0; m_I = -1>','|m_S = -1; m_I =
        1>','|m_S = -1; m_I = 0>','|m_S = -1; m_I = -1>'};
146
147 handles.E(1) = str2num(get(handles.Extext,'String'))
        *10^5;% convert kV/cm to V/m
148 handles.E(2) = str2num(get(handles.Eytext,'String'))
        *10^5;
149 handles.E(3) = str2num(get(handles.Eztext,'String'))
        *10^5;
150 handles.Strain(1) = str2num(get(handles.strainXtext,'
        String')) *10^5;
151 handles.Strain(2) = str2num(get(handles.strainYtext,'
        String')) *10^5;
152 handles.Strain(3) = str2num(get(handles.strainZtext,'
        String')) *10^5;
153
154 txt = ['Total Electric Field(kV/cm) = ' num2str((handles.
        E(1) + handles.Strain(1))/10^5) 'x + ' num2str((
        handles.E(2) + handles.Strain(2))/10^5) 'y +' num2str
        ((handles.E(3) + handles.Strain(3))/10^5) 'z kV/cm' ];
155 set(handles.piText, 'String', txt);
156
157
158 hval = 6.626070040*10^-34;
159
```

```
160 handles.H=subs(handles.H,D,str2num(get(handles.Dgstext,'
        String')) *10^6);
161 handles.H=subs(handles.H,g,-2.00231930436);
162 handles.H=subs(handles.H,mub,9.27400968*10^-24);
163 handles.H=subs(handles.H,planck,hval);
164 handles.H=subs(handles.H,dpar,0.0035 );
165 handles.H=subs(handles.H,dperp,0.17 );
166 handles.H=subs(handles.H,apar,handles.apar );
167 handles.H=subs(handles.H,aperp,handles.aperp );
168 handles.H=subs(handles.H,P,handles.P );
169
170 DrawNV(handles);
171
172 handles.H = vpa(handles.H);
173 handles.allEigenvalues = zeros(9,4);
174 handles.allEigenvectors = zeros(9,9,4);
175
176 for i = 1:4
177 % for i = 1:1
178     [eigenvalues ,eigenvectors] = solveHamiltonian(
            handles, i);
179     handles.allEigenvalues(:,i) = vpa(eigenvalues);
180     handles.allEigenvectors(:,:,i) = vpa(eigenvectors);
181 end
182
183 handles.allEigenvectorsAbs = abs(handles.allEigenvectors)
        ;
184 printLatex(handles.eigenvectors1Axes,latex( vpa(handles.
        allEigenvectorsAbs(:,:,1))));
185 printLatex(handles.eigenvectors2Axes,latex( vpa(handles.
        allEigenvectorsAbs(:,:,2))));
186 printLatex(handles.eigenvectors3Axes,latex( vpa(handles.
        allEigenvectorsAbs(:,:,3))));
187 printLatex(handles.eigenvectors4Axes,latex( vpa(handles.
        allEigenvectorsAbs(:,:,4))));
188 PlotSpectra(handles);
189 loadODMRFile(handles,'fileName.dat','b')
190
191 %Both of the following routines are for NV axis 1
192 if handles.BPolarScanButton.Value
193 %     phiRange = 0;
194     phiRange = [0:10:360];
195
```

```
196     %rotate around NV axis 1 by phi range
197
198     for i=1:length(phiRange)
199         % handles.NVAxis(:,1)
200
201         phi = degtorad(phiRange(i));
202         B = [handles.Bx, handles.By,handles.Bz];
203         NV1Axis = handles.NVAxis(:,1);
204         %Rotate B about NV axis by polar angle phi
205         BRot = B + cross(NV1Axis,B)*sin(phi)+  cross(
                NV1Axis,cross(NV1Axis,B))*(1-cos(phi));
206         handles.Bx = BRot(1);
207         handles.By = BRot(2);
208         handles.Bz = BRot(3);
209
210         PI(1) = (str2num(get(handles.Extext,'String')) +
                str2num(get(handles.strainXtext,'String')))
                *10^5;% convert kV/cm to V/m
211         PI(2) = (str2num(get(handles.Eytext,'String')) +
                str2num(get(handles.strainYtext,'String')))
                *10^5;% convert kV/cm to V/m
212         PI(3) = (str2num(get(handles.Eztext,'String')) +
                str2num(get(handles.strainZtext,'String')))
                *10^5;% convert kV/cm to V/m
213         %[eigenvaluesEOn ,eigenvectorsEOn] =
                solveHamiltonian(handles, 1);
214         EzProj = dot(PI,(handles.NVAxis(:,1)));
215         BzProj = dot(BRot,handles.NVAxis(:,1));
216         orthoVecs = calculateOrtho(handles,handles.NVAxis
                (:,1));
217         ortho1 = orthoVecs(:,1);
218         ortho2 = orthoVecs(:,2);
219         ExProj = dot(PI,ortho1);
220         EyProj = dot(PI,ortho2);
221         EProjection = [ExProj,EyProj,EzProj];
222         BxProj = dot(BRot,ortho1);
223         ByProj = dot(BRot,ortho2);
224         BProjection = [BxProj,ByProj,BzProj];
225
226         [eigenvectorsEOn,eigenvaluesEOn] =
                calculateEigenvalues(handles.H,BProjection,
                EProjection);
227         for k = 1:9
```

```
228                 eigvalEOn(k) = (eigenvaluesEOn(k,k));
229             end
230             energyDiffOn = sort(CalculateEnergyDiffList(
                    handles,eigvalEOn,eigenvectorsEOn));
231
232             EzProj = dot(handles.Strain,handles.NVAxis(:,1));
233             ExProj = dot(handles.Strain,ortho1);
234             EyProj = dot(handles.Strain,ortho2);
235             StrainProjection = [ExProj,EyProj,EzProj];
236
237             [eigenvectorsEOff,eigenvaluesEOff ] =
                    calculateEigenvalues(handles.H,BProjection,
                    StrainProjection);
238
239
240
241             for k = 1:9
242                 eigvalEOff(k) = (eigenvaluesEOff(k,k));
243             end
244
245             energyDiffOff = sort(CalculateEnergyDiffList(
                    handles,eigvalEOff,eigenvectorsEOff));
246
247
248             eigenvaluesShift = energyDiffOn - energyDiffOff;
249             handles.eigenvaluesShiftList(i,:) =
                    eigenvaluesShift;
250 %             eigenvaluesShift
251
252
253             axes(handles.axes1);
254             hold on;
255             BShow = 1.2*BProjection/norm(BProjection);
256
257             plot3([0 BShow(1)],[0 BShow(2)],[0 BShow(3)],'
                    color',[rand(),rand(),rand()],'LineWidth',2)
258             plot3([0 NV1Axis(1)],[0 NV1Axis(2)],[0 NV1Axis(3)
                    ],'color','yellow','LineWidth',2)
259
260         end
261
262
263
```

```
264     simulatedStarkShifts = (handles.eigenvaluesShiftList
            (:,3)) ;
265
266     figure;
267     plot(phiRange, simulatedStarkShifts);
268     figure;
269
270
271     polar(degtorad(phiRange),abs(transpose(
            simulatedStarkShifts)),'--r')
272
273 end
274
275 if handles.BzScanEnable.Value
276     bzRange = [-1000:50:1000]; %Scan range for axial
            magnetic field
277     handles.eigenvaluesShiftList = zeros(length(bzRange)
            ,6);
278         handles.eigenvaluesList = zeros(length(bzRange)
                ,9);
279
280     for i = 1:length(bzRange)
281 %         bzRange(i)
282         PI(1) = (str2num(get(handles.Extext,'String')) +
                str2num(get(handles.strainXtext,'String')))
                *10^5;% convert kV/cm to V/m
283         PI(2) = (str2num(get(handles.Eytext,'String')) +
                str2num(get(handles.strainYtext,'String')))
                *10^5;% convert kV/cm to V/m
284         PI(3) = (str2num(get(handles.Eztext,'String')) +
                str2num(get(handles.strainZtext,'String')))
                *10^5;% convert kV/cm to V/m
285         BProjection = [-0.0*bzRange(i)*10^-7,-0.0*bzRange
                (i)*10^-7,1*bzRange(i)*10^-7];
286         EzProj = dot((PI),(handles.NVAxis(:,1)));
287         orthoVecs = calculateOrtho(handles,handles.NVAxis
                (:,1));
288
289         ortho1 = orthoVecs(:,1);
290         ortho2 = orthoVecs(:,2);
291         ExProj = dot(PI,ortho1);
292         EyProj = dot(PI,ortho2);
293         EProjection = [ExProj,EyProj,EzProj];
```

```
294             [eigenvectorsEOn,eigenvaluesEOn] =
                    calculateEigenvalues(handles.H,BProjection,
                    EProjection);
295             for k = 1:9
296                 eigvalEOn(k) = vpa(eigenvaluesEOn(k,k));
297             end
298
299             energyDiffOn = sort(CalculateEnergyDiffList(
                    handles,eigvalEOn,eigenvectorsEOn));
300
301
302             Strain(1) = ( str2num(get(handles.strainXtext,'
                    String'))) *10^5;% convert kV/cm to V/m
303             Strain(2) = (str2num(get(handles.strainYtext,'
                    String'))) *10^5;% convert kV/cm to V/m
304             Strain(3) = ( str2num(get(handles.strainZtext,'
                    String'))) *10^5;% convert kV/cm to V/m
305             StrainzProj = dot(Strain,(handles.NVAxis(:,1)));
306             StrainxProj = dot(Strain,ortho1);
307             StrainyProj = dot(Strain,ortho2);
308             StrainProjection = [StrainxProj,StrainyProj,
                    StrainzProj];
309
310
311
312
313             [eigenvectorsEOff,eigenvaluesEOff] =
                    calculateEigenvalues(handles.H,BProjection,
                    StrainProjection);
314             for k = 1:9
315                 eigvalEOff(k) = vpa(eigenvaluesEOff(k,k));
316             end
317             energyDiffOff = sort(CalculateEnergyDiffList(
                    handles,eigvalEOff,eigenvectorsEOff));
318             handles.eigenvaluesList(i,:) =          diag(
                    eigenvaluesEOn);
319
320         end
321
322         figure
323         hold on;
324         handles.eigenvaluesList = handles.eigenvaluesList/
                10^6;
```

```
325       bzRange = bzRange / 10^1;
326         handles.eigenvaluesList
327        plot(bzRange, handles.eigenvaluesList(:,1) );
328             plot(bzRange, handles.eigenvaluesList(:,2) );
329
330                 plot(bzRange, handles.eigenvaluesList(:,3)
                        );
331
332       plot(bzRange, handles.eigenvaluesList(:,4) );
333       plot(bzRange, handles.eigenvaluesList(:,5) );
334       plot(bzRange, handles.eigenvaluesList(:,6) );
335       handles.eigenvaluesList
336       FormatFigure(gcf);
337
338       xlabel('Magnetic Field (\mu Tesla)')
339
340       ylabel('Energy(MHz)')
341   end
342
343   set(handles.statusText,'String','Idle');
344
345
346
347   function [eigenvalues eigenvectors] = solveHamiltonian(
          handles, axisId)
348   handles.pi(1) = handles.E(1) + handles.Strain(1);
349   handles.pi(2) = handles.E(2) + handles.Strain(2);
350   handles.pi(3) = handles.E(3) + handles.Strain(3);
351
352   handles.B = [handles.Bx ,handles.By ,handles.Bz];
353   BzProj = dot(handles.B,handles.NVAxis(:,axisId));
354   EzProj = dot(handles.pi,handles.NVAxis(:,axisId));
355   orthoVecs = calculateOrtho(handles,handles.NVAxis(:,
          axisId));
356   ortho1 = orthoVecs(:,1);
357   ortho2 = orthoVecs(:,2);
358   BxProj = dot(handles.B,ortho1);
359   ByProj = dot(handles.B,ortho2);
360   ExProj = dot(handles.pi,ortho1);
361   EyProj = dot(handles.pi,ortho2);
362
363   % ortho1
364   % ortho2
```

```
365
366 BProjection = [BxProj,ByProj,BzProj];
367 PIProjection = [ExProj,EyProj,EzProj];
368 [eigVec,eigVal] = calculateEigenvalues(handles.H,
        BProjection,PIProjection);
369
370 eigVal=vpa(eigVal);
371
372
373
374 for i = 1:9
375     eigenvalues(i) = eigVal(i,i);
376 end
377 eigenvalues = vpa(eigenvalues);
378
379
380 for i = 1:9
381     for k = 1:9
382         if abs(eigVec(i,k)) < 0.0001
383             eigVec(i,k) = 0;
384         end
385     end
386 end
387
388 eigVec = sym(vpa(round(double(eigVec),2))); % change
        number of rounding digits if Latex fails
389 eigenvectors = eigVec;
390
391
392
393 function orthoVectors = calculateOrtho(handles,axis1)
394 randomVector = [0,0.1,0.5];
395 orthoVectors = zeros(3,2);
396
397 orthoVectors(:,1) = cross(randomVector,axis1);
398 orthoVectors(:,2) = cross(orthoVectors(:,1), axis1);
399 orthoVectors(:,1) = 1*orthoVectors(:,1)/norm(orthoVectors
        (:,1));
400 orthoVectors(:,2) = 1*orthoVectors(:,2)/norm(orthoVectors
        (:,2));
401
402 function energyDiffList = CalculateEnergyDiffList(handles
        ,evals,evecs)
```

```
403 energyDiffList = [];
404 for i = 0:2 % loop through ms = 0 energy levels (lowest
    3)
405     energyOfGroundState = evals(9-i)/(10^6);
406     eigvecGS = (evecs(:,9-i));
407     mI = [1,0,-1,1,0,-1,1,0,-1];
408     [M,I] = max(eigvecGS);
409     mIGroundState = mI(I);
410
411     for i = 1:6 % loop through ms = +/- 1 energy levels (
        highest 6 energies)
412         energyOfExcitedState = evals(i)/(10^6);
413         eigvecES = (evecs(:,i));
414         [M,I] = max(eigvecES);
415         mIExcitedState = mI(I);
416         if mIExcitedState == mIGroundState
417             energyDiff = energyOfExcitedState -
                energyOfGroundState;
418             energyDiffList= [energyDiffList, energyDiff];
419         end
420     end
421 end
422 function PlotSpectra(handles)
423
424
425 axes(handles.spectraAxes);
426 %cla;
427 hold on;
428 ylabel('Amplitude','FontSize',7);
429 xlabel('Frequency(MHz)','FontSize',7);
430 box off;
431 set(gca,'FontSize',6.5)
432 totalLor = [];
433 excitedStateEvals = (handles.allEigenvalues(1:6,1:4));
434 topLim = max(excitedStateEvals(:));
435 botLim = min(excitedStateEvals(:));
436 range = [(botLim/10^6)-4:.01:(topLim/10^6)+5];
437   range = [2865:.01:2878];
438
439 totalLor = zeros(1,numel(range));
440 % for axisNum = 1:4
441 for axisNum = 1:4
442     energyDiffList =  CalculateEnergyDiffList(handles,
```

```
        handles.allEigenvalues(:,axisNum),handles.
            allEigenvectors(:,:,axisNum));
443     handles.E(2)/10^5
444     vpa( energyDiffList)
445
446
447     lorentz1 = lorentzian(range,str2num(get(handles.
            linewidthText,'String')), energyDiffList(1),1);
448     lorentz2 = lorentzian(range,str2num(get(handles.
            linewidthText,'String')), energyDiffList(2),1);
449     lorentz3 = lorentzian(range,str2num(get(handles.
            linewidthText,'String')), energyDiffList(3),1);
450     lorentz4 = lorentzian(range,str2num(get(handles.
            linewidthText,'String')), energyDiffList(4),1);
451     lorentz5 = lorentzian(range,str2num(get(handles.
            linewidthText,'String')), energyDiffList(5),1);
452     lorentz6 = lorentzian(range,str2num(get(handles.
            linewidthText,'String')), energyDiffList(6),1);
453     energyDiffList = sort(energyDiffList);
454
455     if axisNum ==1
456         s = strcat('Resonances =  ', latex(vpa(
                energyDiffList(1))),'  , \;  ',latex(vpa(
                energyDiffList(2))),' ,\;  ',latex(vpa(
                energyDiffList(3))),'  , \;  ',latex(vpa(
                energyDiffList(4))),'  , \;  ',latex(vpa(
                energyDiffList(5))),'  , \;  ',latex(vpa(
                energyDiffList(6))),'  , \;  ',latex(vpa(
                energyDiffList(4)-energyDiffList(3))),'  , \;
                 ', latex(vpa(energyDiffList(5)-energyDiffList
                (2))),'  , \;  ', latex(vpa(energyDiffList(6)-
                energyDiffList(1))),'  , \; MHz' );
457         printLatex(handles.eigenvaluesAxes1,s);
458         s = strcat(latex(vpa(energyDiffList(4)-
                energyDiffList(3))),'  ,  ', latex(vpa(
                energyDiffList(5)-energyDiffList(2))),'  ,  '
                , latex(vpa(energyDiffList(6)-energyDiffList
                (1))) );
459         s
460     elseif axisNum==2
461         s = strcat('Resonances =  ', latex(vpa(
                energyDiffList(1))),'  , \;  ',latex(vpa(
                energyDiffList(2))),' ,\;  ',latex(vpa(
```

```
            energyDiffList(3))),'   , \;   ',latex(vpa(
            energyDiffList(4))),'   , \;   ',latex(vpa(
            energyDiffList(5))),'   , \;   ',latex(vpa(
            energyDiffList(4)-energyDiffList(3))),'   , \;
             ',latex(vpa(energyDiffList(5)-energyDiffList
            (2))),'   , \;   ', latex(vpa(energyDiffList(6)-
            energyDiffList(1))),'   , \; MHz' );
462
463         printLatex(handles.eigenvaluesAxes2,s);
464     elseif axisNum==3
465         s = strcat('Resonances =   ', latex(vpa(
            energyDiffList(1))),'   , \;   ',latex(vpa(
            energyDiffList(2))),' ,\;   ',latex(vpa(
            energyDiffList(3))),'   , \;   ',latex(vpa(
            energyDiffList(4))),'   , \;   ',latex(vpa(
            energyDiffList(5))),'   , \;   ',latex(vpa(
            energyDiffList(4)-energyDiffList(3))),'   , \;
             ',latex(vpa(energyDiffList(5)-energyDiffList
            (2))),'   , \;   ', latex(vpa(energyDiffList(6)-
            energyDiffList(1))),'   , \; MHz' );
466
467         printLatex(handles.eigenvaluesAxes3,s);
468     elseif axisNum==4
469         s = strcat('Resonances =   ', latex(vpa(
            energyDiffList(1))),'   , \;   ',latex(vpa(
            energyDiffList(2))),' ,\;   ',latex(vpa(
            energyDiffList(3))),'   , \;   ',latex(vpa(
            energyDiffList(4))),'   , \;   ',latex(vpa(
            energyDiffList(5))),'   , \;   ',latex(vpa(
            energyDiffList(4)-energyDiffList(3))),'   , \;
             ',latex(vpa(energyDiffList(5)-energyDiffList
            (2))),'   , \;   ', latex(vpa(energyDiffList(6)-
            energyDiffList(1))),'   , \; MHz' );
470
471         printLatex(handles.eigenvaluesAxes4,s);
472     end
473
474
475     lor = lorentz1 + lorentz2 + lorentz3 + lorentz4 +
          lorentz5 + lorentz6;
476     totalRange = range;
477
478     if axisNum == 1 && handles.NVAxis1Enable.Value
```

```
479             totalLor = totalLor+ lor;
480         elseif axisNum == 2 && handles.NVAxis2Enable.Value
481             totalLor = totalLor+ lor;
482         elseif axisNum == 3 && handles.NVAxis3Enable.Value
483             totalLor = totalLor+ lor;
484         elseif axisNum == 4 && handles.NVAxis4Enable.Value
485             totalLor = totalLor+ lor;
486
487         end
488
489         axes(handles.spectraAxes)
490
491
492
493         plot(range,axisNum-1+(lor*4));
494         lbl = strcat('NV Axis   ',num2str(axisNum));
495         t= text(range(1),axisNum-1+0.2,lbl);
496         t.FontSize = 6;
497
498     end
499
500     axes(handles.totalSpectraAxes)
501     hold on;
502     ylabel('Amplitude','FontSize',7);
503     xlabel('Frequency(MHz)','FontSize',7);
504     box off;
505     set(gca,'FontSize',6.5);
506     totalLor=totalLor/max(totalLor);
507     plot(range,totalLor,'--');
508     % datacursormode on
509
510     function PlotEnergies(handles,axisId)
511     axes(handles.energyAxes)
512     cla;
513     hold on;
514     for i = 0:2 % loop through ms = 0 energy levels (lowest
        3)
515         energyInMHz = handles.allEigenvalues(9-i,axisId)
            /(10^6);
516         line([5,10],[energyInMHz,energyInMHz]);
517         eigvec = (handles.allEigenvectors(:,9-i,axisId));
518
519         s = '';
```

```
520
521         for k = 1:9
522             if abs(eigvec(k))>0.01
523                 %eigvec(k)
524                 s = strcat(s, '+ ', char(abs(sym(vpa(round(
                        double(eigvec(k)),3))))), ' x ');
525
526                 s = strcat(s,handles.basis(k));
527             end
528         end
529         t = text(4.3,double(energyInMHz+0.25+(mod(i,2)*0.8)),
                s);
530         t.FontSize = 6;
531         ylabel('Energy (MHz)','FontSize',7);
532         set(gca,'FontSize',6.5)
533     end
534     ylimits = get(gca,'ylim');
535     %maxEnergy = double(handles.allEigenvalues(7,axis)/(10^6)
            );
536     %axis([4 11 ylimits(1) 2+maxEnergy]);
537
538     maxEnergy = double(handles.allEigenvalues(7,axisId)
            /(10^6));
539     minEnergy = double(handles.allEigenvalues(9,axisId)
            /(10^6));
540
541     axis([4 11 minEnergy-1 maxEnergy+2]);
542
543     box off;
544     set(gca,'xcolor',get(gcf,'color'));
545     set(gca,'xtick',[]);
546
547     axes(handles.energy2Axes)
548     cla;
549     hold on;
550     for i = 1:6 % loop through ms = +/- 1 energy levels (
            highest 6 energies)
551         energyInMHz = handles.allEigenvalues(i,axisId)/(10^6)
                ;
552
553         line([5,10],[energyInMHz,energyInMHz]);
554         eigvec = (handles.allEigenvectors(:,i,axisId));
555         s = '';
```

```
556
557         for k = 1:9
558             if abs(eigvec(k))>0.01
559                 %eigvec(k)
560
561                 s = strcat(s, '+ ', char(sym(abs(vpa(round(
                        double(eigvec(k)),3))))), ' x ');
562
563                 s = strcat(s,handles.basis(k));
564             end
565         end
566         if i == 1
567             t = text(4.3,double(energyInMHz+0.25),s);
568         else
569             if abs(energyInMHz -  handles.allEigenvalues(i-1,
                    axisId)/(10^6)) < 0.05
570                 t = text(4.3,double(energyInMHz+0.25+(0.5)),s
                        );
571             else
572                 t = text(4.3,double(energyInMHz+0.25),s);
573
574             end
575         end
576
577         t.FontSize = 6;
578         ylabel('Energy (MHz)','FontSize',5);
579         set(gca,'FontSize',6.5)
580     end
581     maxEnergy = double(handles.allEigenvalues(1,axisId)
            /(10^6));
582     minEnergy = double(handles.allEigenvalues(6,axisId)
            /(10^6));
583
584     axis([4  11  minEnergy  maxEnergy+2]);
585     box  off;
586     set(gca,'xcolor',get(gcf,'color'));
587     set(gca,'xtick',[]);
588
589     %}
590     function  loadODMRFile(handles,fileName,color)
591
592     ODMRData = dlmread(fileName);
593     frequencies = ODMRData(:,1);
```

```
594
595 xODMR = ODMRData(:,2);
596 yODMR = ODMRData(:,3);
597 RODMR = xODMR.*xODMR + yODMR.*yODMR;
598 RODMR = sqrt(RODMR);
599 maxR = max(RODMR);
600 RODMR = 8*RODMR/norm(RODMR);
601
602 axes(handles.totalSpectraAxes)
603 hold on;
604 plot(frequencies,RODMR,...
605     'LineStyle','-',...
606     'MarkerSize',0.1,...
607     'MarkerEdgeColor',color,...
608     'MarkerFaceColor',color)
609
610
611 function DrawNV(handles)
612 axes(handles.axes1);
613 %cla;
614 rotate3d on;
615
616 [x,y,z] = sphere(20);
617 hold on
618
619 handles.Bx = (10^-7)*str2num(get(handles.Bxedit,'String'))
    ); %Convert from miligaus to Tesla
620 handles.By = (10^-7)*str2num(get(handles.Byedit,'String'))
    );
621 handles.Bz = (10^-7)*str2num(get(handles.Bzedit,'String'))
    );
622 BVector = [handles.Bx,handles.By,handles.Bz];
623 BVector = 1.2*BVector/norm(BVector);
624
625
626 EVector = [((handles.E(1) + handles.Strain(1))/10^5), ((
    handles.E(2) + handles.Strain(2))/10^5), ((handles.E
    (3) + handles.Strain(3))/10^5)];
627 if max(EVector) ~=0
628     EVector = 1.2*EVector/max(abs(EVector));
629 end
630     EVector = 1.2*EVector/max(abs(EVector));
631 %
```

```
632 plot3([0 BVector(1)],[0 BVector(2)],[0 BVector(3)],'color
        ','green','LineWidth',2) % for magnetic field
633 text(BVector(1),BVector(2),BVector(3),'B');
634
635
636 plot3([0 EVector(1)],[0 EVector(2)],[0 EVector(3)],'color
        ','yellow','LineWidth',2) % for electric field
637 text(EVector(1),EVector(2),EVector(3),'E');
638
639 % plot3([-1,1],[0,0],[0,0],'r','LineWidth',2);
640 % plot3([0,0],[-1,1],[-1,1],'g','LineWidth',2);
641 % plot3([0,0],[1,-1],[-1,1],'b','LineWidth',2);
642
643 plot3([0,0],[2,-2],[2,-2],'k','LineWidth',4);
644
645
646 plot3([0,-12.2/5],[0,0/5],[0,8.66/5]);
647 offset = 1.5;
648 plot3([1+offset 2+offset],[1+offset 1+offset],[1+offset
        1+offset]); % for x-axis
649 plot3([1+offset 1+offset],[1+offset 2+offset],[1+offset
        1+offset]) ;% for y-axis
650 plot3([1+offset 1+offset],[1+offset 1+offset],[1+offset
        2+offset]) ;% for z-axis
651 text(2+offset,1+offset,1+offset,'x');
652 text(1+offset,2+offset,1+offset,'y');
653 text(1+offset,1+offset,2+offset,'z');
654 %
655 text( handles.NVAxis(1,1)+.1,handles.NVAxis(2,1),handles.
        NVAxis(3,1) ,'NV1');
656 text( handles.NVAxis(1,2)+.1,handles.NVAxis(2,2),handles.
        NVAxis(3,2) ,'NV2');
657 text( handles.NVAxis(1,3)+.1,handles.NVAxis(2,3),handles.
        NVAxis(3,3) ,'NV3');
658 text( handles.NVAxis(1,4)+.1,handles.NVAxis(2,4),handles.
        NVAxis(3,4) ,'NV4');
659
660
661 origin = [0,0,0];
662 NAtomPts = handles.NVAxis(:,1);
663 VAtomPts = [0,0,0];
664 C1AtomPts = handles.NVAxis(:,2);
665 C2AtomPts = handles.NVAxis(:,3);
```

```
666 C3AtomPts = handles.NVAxis(:,4);
667
668
669 line([origin(1),NAtomPts(1)]',[origin(1),NAtomPts(2)]', [
        origin(1),NAtomPts(3)]')
670 line([origin(1),C1AtomPts(1)]',[origin(1),C1AtomPts(2)]',
        [origin(1),C1AtomPts(3)]')
671 line([origin(1),C2AtomPts(1)]',[origin(1),C2AtomPts(2)]',
        [origin(1),C2AtomPts(3)]')
672 line([origin(1),C3AtomPts(1)]',[origin(1),C3AtomPts(2)]',
        [origin(1),C3AtomPts(3)]')
673
674 s=1;
675 x=([0 1 1 0 0 0;1 1 0 0 1 1;1 1 0 0 1 1;0 1 1 0 0 0]-0.5)
        *s;
676 y=([0 0 1 1 0 0;0 1 1 0 0 0;0 1 1 0 1 1;0 0 1 1 1 1]-0.5)
        *s*4;
677 z=([0 0 0 0 0 1;0 0 0 0 0 1;1 1 1 1 0 1;1 1 1 1 0 1]-0.5)
        *4*s;
678
679 for i=1:6
680     h=patch(x(:,i),y(:,i),z(:,i),'w');
681     h.FaceAlpha = 0.2;
682     set(h,'edgecolor','k')
683     set(h,'lineStyle',':')
684
685 end
686
687 [x,y,z] = sphere(25);
688 radius = .1;
689 Natom = surf(radius*x+NAtomPts(1),radius*y+NAtomPts(2),
        radius*z+NAtomPts(3),'FaceColor','blue','EdgeColor','
        none');
690 Natom = surf(radius*x+VAtomPts(1),radius*y+VAtomPts(2),
        radius*z+VAtomPts(3),'FaceColor','red','EdgeColor','
        none');
691 Natom = surf(radius*x+C1AtomPts(1),radius*y+C1AtomPts(2),
        radius*z+C1AtomPts(3),'FaceColor','red','EdgeColor','
        none');
692 Natom = surf(radius*x+C2AtomPts(1),radius*y+C2AtomPts(2),
        radius*z+C2AtomPts(3),'FaceColor','red','EdgeColor','
        none');
693 Natom = surf(radius*x+C3AtomPts(1),radius*y+C3AtomPts(2),
```

```
    radius*z+C3AtomPts(3),'FaceColor','red','EdgeColor','
    none');
694
695 camproj('orthographic')
696 az = 10   ;
697 el = (90-54.735610310247);
698 view(az, el);
699 grid on
700 axis equal off     % make the axes equal and invisible
701 set(gcf,'color','w');
702
703
704
705
706 function   val = lorentzian(range, fwhm, center, height)
707 val = zeros(size(range), 'double');
708 for i = 1:length(range)
709     val(i) = (1/pi) * (fwhm/2)/ (   (range(i)-center)^2 +
        (fwhm/2)^2);
710 end
711 val = val/norm(val);
712
713
714
715
716 function printLatex(haxes, Latext)
717
718 axes(haxes);
719 cla
720
721 s = strcat('$ ',Latext,'$');
722
723 s = strrep(s,'mub','\mu_b');
724 s = strrep(s,'Bz','B_z');
725 s = strrep(s,'By','B_y');
726 s = strrep(s,'Bx','B_x');
727
728 s = strrep(s,'piz','\pi_z');
729 s = strrep(s,'piy','\pi_y');
730 s = strrep(s,'pix','\pi_x');
731
732 s = strrep(s,'dpar','d_\parallel');
733 s = strrep(s,'dperp','d_\perp');
```

```
734 s = strrep(s,'aperp','A_\perp');
735 s = strrep(s,'apar','A_\parallel');
736 s = strrep(s,'gpar','g_\parallel');
737 s = strrep(s,'gperp','g_\perp');
738 s = strrep(s,'planck','h');
739
740
741 text('Interpreter','LaTex',...
742     'string',s,...
743     'FontSize',10)
744 axis off
```